3-2013

# Ab-initio and model studies of spin fluctuation effects in transport and thermodynamics of magnetic metals

James K. Glasbrenner
*University of Nebraska-Lincoln*, james.glasbrenner.ctr@nrl.navy.mil

Glasbrenner, James K., "Ab-initio and model studies of spin fluctuation effects in transport and thermodynamics of magnetic metals" (2013). *Theses, Dissertations, and Student Research: Department of Physics and Astronomy*. 23.
http://digitalcommons.unl.edu/physicsdiss/23

# AB-INITIO AND MODEL STUDIES OF SPIN FLUCTUATION EFFECTS IN TRANSPORT AND THERMODYNAMICS OF MAGNETIC METALS

by

James K. Glasbrenner

A DISSERTATION

Presented to the Faculty of
The Graduate College at the University of Nebraska
In Partial Fulfilment of Requirements
For the Degree of Doctor of Philosophy

Major: Physics & Astronomy

Under the Supervision of Professor Kirill D. Belashchenko

Lincoln, Nebraska
March, 2013

# AB-INITIO AND MODEL STUDIES OF SPIN FLUCTUATION EFFECTS IN TRANSPORT AND THERMODYNAMICS OF MAGNETIC METALS

James K. Glasbrenner, Ph. D.
University of Nebraska, 2013

Adviser: Kirill D. Belashchenko

Magnetic materials are vital to many devices and the manipulation of spins is central to the operation of novel devices such as spin transistors. It is important to understand the effect of spin fluctuations on such systems. In this dissertation, first-principles calculations and models further the understanding of spin fluctuation effects in the transport and thermodynamics of magnetic metals.

A simple classical spin-fluctuation Hamiltonian with a single itinerancy parameter is studied using the mean-field approximation, Monte Carlo simulations, and a generalized Onsager cavity field method. The results of these different methods are in agreement. It is found that the thermodynamics are sensitive to the choice of phase space measure and that short-range order is weak for all degrees of itinerancy.

Spin injection from a half-metallic electrode in the presence of thermal spin disorder is analyzed using a combination of random matrix theory, spin-diffusion theory, and explicit simulations for the tight-binding *s*-*d* model. It is shown that spin-flip scattering from the interface destroys spin coherence. Spin injection is possible and is constrained by the mean-free path and spin diffusion length in the semiconductor.

The spin-disorder resistivity (SDR) is calculated for the Gd-Tm series in the paramagnetic state using two complimentary first-principles approaches. The SDR in the series follows an almost universal dependence on the exchange splitting and is underestimated when compared with experiment. Frozen atomic displacements (phonons) are then introduced along with spin disorder and the total resistivity is calculated as a function of the mean-square displacement for Fe and Gd. The resistivity increases non-linearly for small displacements and transitions to a linear dependence at larger displacements that, when fitted, enhances the SDR. The enhancement observed in Gd is substantial. The enhancements are electronic in origin, and the rapid increase observed in Gd is traced to a strong, disorder-induced interaction between the electron and hole Fermi surfaces, while the linear trend at large displacements is a saturation effect brought on by strong disorder.

# ACKNOWLEDGMENTS

This has been a time of great personal discovery for myself while working on this dissertation, reaching several important life milestones along the way. I have been challenged, felt the joy of discovery, and discovered for myself what it means to be a scientist. I have had a lot of assistance along the way, and as such, there are many people that I would like to thank for helping me out while I worked on this dissertation.

First, I would like to thank my supervisor Prof. Kirill Belashchenko for providing me with support, guidance, and being an invaluable teacher and mentor every step of the way. As a teacher his classes challenged me, honing my critical thinking skills and developing my intuition for modeling the physical world. As a mentor he provided me with fascinating research questions and invaluable insight into the physical interpretation of my work, equipping me with the skill-set necessary to carry out my own research. Under his guidance I've learned how to look at a research project from every angle, using the information gathered to build a complete picture of the physics involved. The quality of the work in this dissertation simply would not have been possible without him. Finally I also would like to thank him for his interest in my scientific career by sending me to interesting conferences where I was able to develop my skills as a presenter, and encouraging me to look into many different options for my post-graduate career.

I would like to thank the other members of my supervisory committee, Prof. Evgeny Tsymbal, Prof. Christian Binek, Prof. Timothy Gay, and Prof. Xiao Zeng, for their insight during this critical period of my life and their careful reading of this dissertation. In particular, I thank Prof. Tsymbal for being a wonderful classroom instructor during my early years in graduate school and I am grateful for his interesting ques-

tions about my work during the weekly condensed matter theory seminars. I thank Prof. Binek for his friendship and his effort to attend my seminars whenever I held one. I thank Prof. Gay for his friendly conversations about my progress and future aspirations, and also thank both him and Prof. Zeng for taking an interest in my work despite it lying outside of their own research interests.

Much of the work presented here is the result of collaboration and there are several wonderful people I would like to thank for making that possible. First, I thank Dr. Aleksander Wysocki for giving me guidance and instruction while he was a part of Prof. Belashchenko's research group and collaborating with me on the work in Chapters 3 & 4. I had many interesting conversations with him and I am especially grateful for the Fortran code examples he provided to me as well as his assistance in learning to use the LMTO software package. I thank Prof. Sergii Khmelevskyi, Prof. Ilya Turek, Prof. Vaclav Drchal, and especially Prof. Josef Kudrnovský for their collaboration and work on the DLM calculations presented in Chapter 5. I thank Dr. Bhalchandra Pujari for his help in calculating the spectral function in Chapter 6 and for the interesting conversations we've had. In addition to the aforementioned collaborators, I also would like to thank Dr. Joonhee An for our many insightful conversations during his time as a postdoc and fellow group-mate Mr. Sai Mu for our many discussions about our research, our life experiences while living in the Heartland of America, and trading war stories about the experience of being a graduate student.

Relocating to the middle of the country to attend graduate school after growing up in Pennsylvania was not easy. I would like to thank my friends back home for their active interest throughout these years in what I've been doing with my life. I appreciate the time they've taken to stay in contact with me, which has helped to keep me sane, and I can't wait to be geographically closer to them. I want to thank my parents, Paul and Lori Glasbrenner, for their support and encouragement. They always believed in my abilities, even when I doubted them myself, and sacrificed a lot to allow me to get to this point in my life. And I want to thank my brother Aaron for being the more laid-back of the two of us and cheering me on as I completed this crucial step of my life and career.

Finally, I would like to thank my wife Meghan. I would not have been able to summon the willpower to make it through this long period of study without her. While I was working on this dissertation we went from being friends to husband and wife, and her words of love and encouragement provided me with the motivation to take control of my research and work towards the final product contained in this manuscript. She has been my best friend for close to ten years and has always believed in me. She has made so many sacrifices for me to make sure I could stay on track to finish this work. She has helped to keep me organized and level-headed and I love her with all my heart. It is difficult to see how I would have been able to complete this program of study without her in my life. Meghan, thank you.

# DEDICATION

To Meghan, my best friend and wife, who has given me so much joy and support over the past ten years, I dedicate this work to you.

# Contents

# List of Figures

# List of Tables

## *Chapter 1*

# Introduction

Magnets are a fixture of everyday life. Many people have played with permanent magnets as children, captivated by the mysterious behavior and physics that result from like poles repelling and opposite poles attracting. The fascination with magnets has a long history, from the invention of the compass in China to William Gilbert's experimental determination in 1600 that the Earth itself can be considered a giant magnet. Nowadays magnets are a crucial component in many technological devices, such as hard drives, cars, radios, televisions, refrigerators, and cellphones. Modern life would be very different without permanent magnets.

The development of the classical theory of magnetism began with Oersted's discovery in 1820 that magnetic forces are produced by electric currents. Further studies by Biot and Savart, as well as Ampére furthered the understanding of magnetic forces, and the development of electromagnetic field theory by Faraday and Maxwell placed the field of classical electromagnetism on firm footing. However, the spontaneous magnetism of solids is a phenomenon that can only be understood in the framework of quantum mechanics [13]. The spin degree of freedom of the electron in combination with the exchange interaction is now understood to be the microscopic origin of magnetism.

Beyond current commercial applications, the manipulation of electronic spins in materials holds tremendous promise for future devices and for the continuation of Moore's law. Moore's law is the observation that the number of transistors on integrated circuits doubles roughly every two years. The standard approach to increasing the number of transistors on a chip is to scale down the size of each transistor. However a fundamental limit is approached when the transistor is only a few nanometers long [14]. At these small length scales electrons can tunnel from source to drain without an applied gate voltage and the transistor no longer behaves like a binary switch. Assuming this could be solved, there is the ultimate length-scale limit of approximately 1.5 nanometers, which is thought to be the smallest scale possible where a source and drain may still be defined. Additionally, packing these small transistors together and passing a current through them results in Joule heating, and there are significant challenges to efficiently removing heat at these length scales without sacrificing performance [15]. Using the electron's spin degree of freedom in transistors instead of its charge has been proposed [16]. This is an attractive option to continuing Moore's Law as pure spin currents do not give rise to Joule heating, which overcomes one of the significant obstacles in scaling. There is hope that spin transistors will lead to faster and smaller transistors. However, in order to ultimately develop commercial versions of these devices, a solid understanding of the physics of spin manipulation is required, especially in the context of finite temperature where spin fluctuations become important.

In the rest of this introductory chapter, the classical theory of paramagnetism and the quantum origin of magnetism will be reviewed. This is followed by a discussion of the origin of ferromagnetism. Afterwards, a background overview to prepare the reader for the forthcoming chapters will be discussed, including ferromagnetic ordering in local and itinerant systems, spin-diffusion transport theory, and magnetic scattering in the heavy rare-earth metals. The introductory chapter concludes with an overview of the rest of this dissertation.

## 1.1 Classical theory of magnetism

The classical understanding of the dynamics of electromagnetic fields is contained in the Maxwell equations. Typically, the Maxwell equations are presented in two different versions: the microscopic and macroscopic forms. This division is for convenience and it can be shown that the microscopic electric and magnetic fields due to the classical versions of atoms and/or molecules in a solid lead naturally to the macroscopic fields **D** and **H**, see Refs. [17–19] for formal proofs. This analysis connects the magnetic field **B** to the macroscopic field **H** and the magnetization **M** via the familiar equation,

$$\mathbf{H} = \frac{\mathbf{B}}{\mu_0} - \mathbf{M}. \tag{1.1}$$

In classical theory, the magnetization vector **M** encapsulates the magnetic field due to the induced and permanent magnetic moments in materials. Below follows a brief historical overview of the classical description of paramagnetism and the Weiss theory of ferromagnetism, followed by a discussion of the problems presented by a purely classical treatment.

The response of **M** to an applied field **H** is parameterized by the magnetic susceptibility $\chi_M$,

$$\mathbf{M} = \chi_M \mathbf{H}, \tag{1.2}$$

where

$$\chi_M = \left(\frac{dM}{dH}\right)_{H=0}. \tag{1.3}$$

In general, the magnetic susceptibility is a tensor and can have a complicated dependence on different properties, such as field orientation and magnitude, temperature, and the application of stress and strain. Typical analysis assumes the magnetic response to be isotropic and $\chi_M$ is simply a temperature-dependent scalar. The contributions to the magnetic susceptibility can be broken down into two categories, diamagnetic and paramagnetic. The diamagnetic response, which produces a magnetization that opposes an applied field and is present in all substances, is the result of applied fields inducing molecular currents, in accordance with Lenz's law. The paramagnetic response, which is much stronger than the diamagnetic response, produces a magnetization parallel to an applied field and occurs in materials with intrinsic magnetic moments. Thus all atoms, ions, and molecules with an odd number of electrons exhibit paramagnetism. Elements with partially-filled $d$ or $f$ shells (transition and rare-earth elements) are paramagnetic, as are many metals [13]. In subsequent discussions only the paramagnetic response will be considered. The diamagnetic response can usually be evaluated separately. It is important to remember that for a full description both the diamagnetic and paramagnetic contributions need to be taken into account.

Paramagnets do not exhibit a magnetization in the absence of an applied field despite having permanent microscopic magnetic moments because thermal fluctuations randomize them. When an external field is applied, the field produces a torque on the moments, making it favorable for them to align parallel to the field, competing with thermal fluctuations which destroy this alignment. When the field is strong enough (called the saturation field), all the moments will be parallel and the magnetization will reach its maximum value. Langevin solved the problem of a classical gas of rigid, magnetically polarized molecules with moment $m$ [20], finding the magnetization $M$ to be

$$M = NmL\left(\frac{mH}{k_B T}\right), \tag{1.4}$$

where $N$ is the number of magnetic molecules, $k_B$ is the Boltzmann constant, $T$ is the temperature, and $L(x) = \coth x - (1/x)$ is the classical Langevin function. The magnetic susceptibility can be found via Eq. 1.3, and for low fields $\mu H \ll k_B T$ the paramagnetic susceptibility simplifies to Curie's law [21],

$$\chi_M = \frac{Nm^2}{3k_B T}, \tag{1.5}$$

Performing a measurement of the susceptibility as a function of temperature and fitting to Eq. 1.5 gives an experimental estimation of the local moment for a paramagnetic material.

The paramagnetic theory does not explain ferromagnetic behavior, where a spontaneous magnetization is sustained in the absence of external fields. Weiss postulated the existence of an internal molecular field $H_{\text{mol}}$ to explain ferromagnetic alignment [22], replacing $H \rightarrow H_{\text{ext}} + H_{\text{mol}}$, where $H_{\text{mol}} = \beta M$. This modifies the paramagnetic theory, predicting the magnetization to be

$$M = NmL\left[\frac{m\left(H_{\text{ext}} + \beta M\right)}{k_B T}\right] \tag{1.6}$$

which is finite in the absence of external fields. The magnetization vanishes above the Curie temperature $T_c = \beta N m^2/3k_B$ as the moments are completely randomized and the system becomes paramagnetic. Above $T_c$, the magnetic susceptibility is

$$\begin{aligned}\chi_M &= \frac{Nm^2/3k_B}{T - \beta Nm^2/3k_B} \\ &= \frac{\chi_0}{T - T_c},\end{aligned} \tag{1.7}$$

which is known as the Curie-Weiss law. The Langevin-Weiss theory, which was reasonably successful in describing the physics of a variety of simple ferromagnets, was the state of the classical theory of ferromagnetism at the beginning of the twentieth century.

Despite the successes of the Langevin-Weiss theory, there are a number of fundamental problems with it that cannot be resolved in the classical description. Relaxing the assumption that the magnetic moments are rigid is necessary for a rigorous description. Within the classical picture, the magnetic moments are generated by electrons that circle around atoms in orbits, and there is no *a priori* reason to constrain the radius of these orbits. If the Boltzmann distribution is applied to all electronic degrees of freedom in the atoms, then it is found that the diamagnetic and paramagnetic contributions exactly cancel each other and the magnetic susceptibility is zero [23, 24]. Another problem is that the classical free electron gas is predicted to not have a diamagnetic response. The Langevin-Weiss theory cannot be reproduced if Boltzmann statistics are applied to the intrinsic degrees of electronic freedom. A well formed theory ought to be able to handle the intrinsic degrees of freedom, and no such theory exists in classical mechanics. A proper, rigorous description of magnetism requires quantum mechanics, which is the topic of the next section.

## 1.2 Quantum theory of magnetism

Modern physics has been shown that the electron may be a two-fold source of magnetism. The first type of magnetism is the intrinsic spin moment and the second type of magnetism is due to the translational or orbital motion of the electron [13]. Intrinsic spin angular momentum is quantified by the quantum operator **S**, has no classical analog (early theories postulated that the electron itself rotated [25], hence the name spin), and historically spin was inserted into quantum theory because of empirical observation of the "duplexity" of atomic spectra. The explanation of the spin degree of freedom came from Dirac's equation, where spin is understood to be a consequence of special relativity. Orbital angular momentum is quantified by the quantum operator **L** and has a classical analog: for example the orbital momentum of an electron circling an atom. Both sources of angular momentum give rise to a magnetic moment, and in general the effect of spin is largely responsible for the magnetic properties of solids.

Both the spin and orbital angular momentum are quantized. In a single-electron atom, the magnitudes of the respective operators are

$$|\mathbf{S}| = \hbar\sqrt{S(S+1)}, \tag{1.8}$$

$$|\mathbf{L}| = \hbar\sqrt{L(L+1)}. \tag{1.9}$$

The projections of **S** and **L** along the quantization axis $z$ are

$$S_z = m_s\hbar; \qquad m_s = \pm 1/2, \tag{1.10}$$

$$L_z = m_\ell\hbar; \qquad m_\ell = L, L-1, \ldots, 0, \ldots, -L. \tag{1.11}$$

The projections of the magnetic moment along the quantization axis are related to the $z$ axis projections of the spin and angular momentum

$$\mu_z^{(s)} = g_s m_s \mu_B; \qquad g_s = 2.00231930436153 \pm 5.3 \times 10^{-13} \text{ [26]}, \tag{1.12}$$

$$\mu_z^{(\ell)} = g_\ell m_\ell \mu_B; \qquad g_\ell = 1. \tag{1.13}$$

Because of the electron's negative charge, the spin moment $\mu_z^{(s)}$ is aligned anti-parallel to $S_z$. The absolute spin and angular magnetic moment, found by substituting $S_z \to |\mathbf{S}|$ and $L_z \to |\mathbf{L}|$ is

$$|\boldsymbol{\mu}_s| = 2\mu_B \sqrt{S(S+1)}, \tag{1.14}$$

$$|\boldsymbol{\mu}_\ell| = \mu_B \sqrt{L(L+1)}. \tag{1.15}$$

The above vector model for the single-electron atom also introduces the total angular momentum operator $\mathbf{J} = \mathbf{L} + \mathbf{S}$ with magnitude $|\mathbf{J}| = \hbar\sqrt{J(J+1)}$ [13]. The eigenvalues of the operators $\mathbf{S}$, $\mathbf{L}$, and $\mathbf{J}$ are used to characterize the state of the single-electron atom.

In the many-electron atom, the vector summing rules are as follows. The spin and orbital momentum operators are the sum of the individual electron contributions, $\mathbf{S} = \sum_i \mathbf{S}_i$ and $\mathbf{L} = \sum_i \mathbf{L}_i$. The total angular momentum is, as in the one-electron atom, $\mathbf{J} = \mathbf{L} + \mathbf{S}$. This corresponds to Russell-Saunders coupling, which is valid when the electrostatic interaction between the many electrons is much greater than the spin-orbit interaction, which is the case in the light elements[1] [13]. The eigenvalues

---

[1] The $jj$ coupling scheme is used for very heavy elements ($Z > 75$), in which the individual spin and orbital momentum $\mathbf{S}_i$ and $\mathbf{L}_i$ for an electron are coupled with the other electrons' momenta. The total momentum for an individual electron is $\mathbf{J}_i = \mathbf{L}_i + \mathbf{S}_i$, and after this is worked out for all electrons, then the total momentum of the system is $\mathbf{J} = \sum_i \mathbf{J}_i$.

for the total momentum are

$$|\mathbf{J}| = \hbar\sqrt{J(J+1)}; \qquad |L-S| \leq J \leq |J+S|. \tag{1.16}$$

The different values of $J$ form a degenerate multiplet, which is lifted via the spin-orbit interaction. The projection of $\mathbf{J}$ along the quantization axis $z$ has the eigenvalues

$$J_z = m_J\hbar; \qquad m_J = J, J-1, \ldots, 0, \ldots, -J. \tag{1.17}$$

The $z$ axis projection and absolute value of the total magnetic moment are

$$\mu_z^{(J)} = g_J m_J \mu_B, \tag{1.18}$$

$$|\boldsymbol{\mu}_J| = g_J \mu_B \sqrt{J(J+1)}, \tag{1.19}$$

where $g_J$ is the Landé g-factor for the many-electron atom. When an electron cloud of arbitrary $L$ and $S$ interacts with an external magnetic field, because of the anomalous spin g-factor, the interaction term involves $\mathbf{L}+2\mathbf{S}$ instead of $\mathbf{L}+\mathbf{S}$, so it is necessary to project $\mathbf{L}+2\mathbf{S}$ along $\mathbf{J}$ and find the g-factor that satisfies $(\mathbf{L}+2\mathbf{S})\cdot\mathbf{J} = g\mathbf{J}^2$ [27]. In the approximation that $g_s = 2$, the Landé g-factor is

$$g_J = 1 + \frac{1}{2}\frac{J(J+1)+S(S+1)-L(L+1)}{J(J+1)}. \tag{1.20}$$

Nonzero values for Eqs. 1.18 & 1.19 in atoms are possible in atoms with an odd number of electrons and in partially-filled $d$ and $f$ electronic shells, as discussed previously. In the transition and rare-earth elements, there are multiple orbital occupation configurations possible, and it is not immediately clear which configuration corresponds to the ground state. A simple method to determine the orbital configuration of the ground state in an atom is Hund's rules (quoting Ref. [13]):

1. "The total spin quantum number $S = \sum m_s$ in the ground state is a maximum within the limits prescribed by the Pauli principle.
2. The total orbital quantum number $L = \sum m_\ell$ in the ground state is a maximum within the limits prescribed by rule 1.
3. The quantum number $J$ of the total angular momentum for a shell which is not completely filled is: $J = L - S$, if the shell is less than half full; $J = L + S$, if the shell is more than half full."

For a justification of Hund's rules see, for example, Ref. [28].

When determining the ground state of materials Hund's rules may be applied, although some care must be taken and in general it cannot be expected to give a correct quantitative description. In materials, the constituent ions give rise to a potential throughout the solid called the crystal field. The inhomogeneous crystal field interacts strongly with the outer electron shells and deviations from atomic behavior are expected. One consequence is that $L_z$ may average to zero, as observed in the transition metals, thus "quenching" the orbital angular momentum and causing the magnetic moment to be determined by spin only (i.e. Hund's first rule). On the other hand, highly localized orbitals deeper in the ionic core such as the 4f orbitals in the rare-earth metals are less affected by the crystal field and exhibit stronger spin-orbit coupling. These effects contribute to an unquenching of the orbital moment, and the full set of Hund's rules should be used.

## 1.3 Quantum theory of paramagnetism

In this section two types of paramagnetism will be discussed in the context of quantum mechanics. The first is the paramagnetism of local moments, which in the proper limit reproduces the Curie law and the Langevin theory. The second type of paramagnetism is that of metals, where the electron gas interacts with an external field to develop a net magnetization. This is also called Pauli paramagnetism.

### 1.3.1 Paramagnetism of local moments

Consider a system of $N$ non-interacting atoms in a volume $V$ with a degenerate ground state determined by $\mathbf{L}$, $\mathbf{S}$, and $\mathbf{J}$. The application of a magnetic field lifts the degeneracy, splitting the ground state into a $2J+1$ multiplet. The fields are small enough that excitations to higher energy multiplets can be ignored, such that the energy of an atom in an external field is $E = -\boldsymbol{\mu} \cdot \mathbf{H}$. The magnetic moment per atom is $\boldsymbol{\mu} = -g_J \mu_B \mathbf{J}$ and the external field is $\mathbf{H} = H\widehat{z}$.

To find the magnetization and magnetic susceptibility as a function of temperature, the free energy first must be determined. The free energy $F$ of the system is found by solving the statistical equation

$$\begin{aligned} e^{-\beta F} &= \sum_{m_J=-J}^{J} e^{-\beta g_J \mu_B H m_J} \\ &= \frac{e^{\beta g_J \mu_B H(J+1/2)} - e^{-\beta g_J \mu_B H(J+1/2)}}{e^{\beta g_J \mu_B H/2} - e^{-\beta g_J \mu_B H/2}}, \end{aligned} \tag{1.21}$$

where $\beta = (k_B T)^{-1}$. The magnetization can then be immediately written down as

$$M = -\frac{N}{V}\frac{\partial F}{\partial H} \tag{1.22}$$

$$= \frac{N}{V} g_J \mu_B J B_J(\beta g_J \mu_B J H), \tag{1.23}$$

where the Brillouin function $B_J$ is defined as

$$B_J(x) = \frac{2J+1}{2J}\coth\frac{2J+1}{2J}x - \frac{1}{2J}\coth\frac{1}{2J}x. \tag{1.24}$$

When $k_B T \gg g_J \mu_B H$, $x \ll 1$ and the magnetic susceptibility simplifies to

$$\chi_M \approx \frac{1}{V}\frac{NJ(J+1)g_J^2\mu_B^2}{3k_B T}, \tag{1.25}$$

corresponding to a Curie constant of

$$C = \frac{d\chi_M^{-1}}{dT} = \frac{3k_B}{NJ(J+1)g_J^2\mu_B^2}. \tag{1.26}$$

Defining an effective moment $m_{\text{eff}} = g_J \mu_B \sqrt{J(J+1)}$, the Langevin result of Eq. 1.5 is recovered.

The effective moment is formally identical to Eq. 1.19. Therefore, measurements of the Curie constant allow comparison between the experimental value of $m_{\text{eff}}$ and the quantum mechanical calculation $|\boldsymbol{\mu}_J|$, which reveals the degree of quenching in an element. The effective moment of the heavy rare-earth metals is, rather remarkably, predicted with reasonable accuracy when $J$ is determined using Hund's rules, while for the transition metals the orbital moment is quenched and one should use $J = S$ and $g_J \approx 2$ [18, 29]. It should be noted that for Fe, for example, using just Hund's first rule still does not accurately determine the ground state moment. Instead, an accurate determination is possible using first-principles band theory, such as that described in Chapter 2.

### 1.3.2 Pauli paramagnetism

When a magnetic field is applied to a metal, the electron gas may exhibit a paramagnetic response called Pauli paramagnetism. An expression for the response can be derived in the independent electron approximation and, for simplicity, the conduction electrons are assumed to have fully quenched orbital moments [30]. An electron with spin parallel to **H** contributes a magnetization density $-\mu_B/V$ and with spin antiparallel contributes $\mu_B/V$. Let $n_\uparrow$ be the number of electrons with a positive contribution to the magnetization density (anti-parallel spin to H) and $n_\downarrow$ be the number of electrons with a negative contribution (parallel spin to H). The total magnetization due to the conduction electrons is

$$M = \mu_B(n_\uparrow - n_\downarrow). \tag{1.27}$$

The following derivation of the Pauli susceptibility follows Ref. [27]. The energy density

$$\frac{E}{V} = \frac{\mu_B^2}{2\chi_p}(n_\uparrow - n_\downarrow)^2 - \mu_B(n_\uparrow - n_\downarrow)H \tag{1.28}$$

replicates Eq. 1.27 for the minimization condition $\partial E/\partial(n_\uparrow - n_\downarrow) = 0$. Physically, the first term in Eq. 1.28 corresponds to the increase in kinetic energy due to the transfer of $\downarrow$ electrons to unoccupied $\uparrow$ states, and the second term is the energy decrease due to aligning spins with the external field. Alternatively, the energy density can be

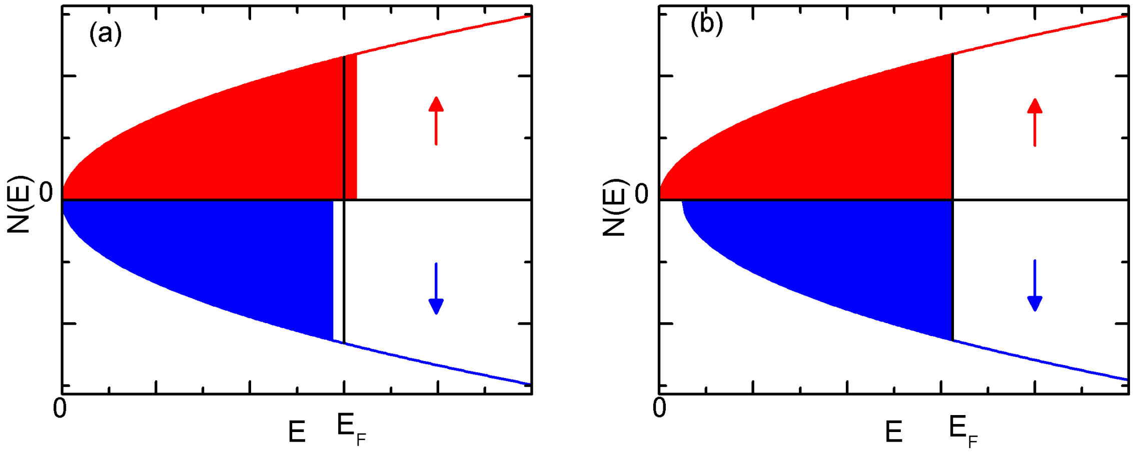

Figure 1.1: The density of states for a Pauli paramagnet in an external field. (a) When the field is applied, electrons from the ↓ channel populate unoccupied states in the ↑ channel. (b) The realignment of the Fermi level.

calculated by taking integrations over the density of states (DOS)

$$E = \int_{-\infty}^{E_\uparrow} EN_\downarrow(E)dE + \int_{-\infty}^{E_\downarrow} EN_\uparrow(E)dE - \mu_B(n_\uparrow - n_\downarrow)H. \tag{1.29}$$

Fig. 1.1 illustrates what happens when the field $H$ is applied. Around the Fermi energy, a small fraction of ↓ electrons populate empty states above the Fermi energy in the ↑ channel. Because of the Pauli exclusion principle, electrons that occupy states far below the Fermi energy cannot be promoted to empty states. Since only the electrons at and near the Fermi energy are effected by the applied field, the DOS in Eq. 1.29 can be approximated by its value at the Fermi energy, $N_{\uparrow,\downarrow}(E) \approx N_s(E_F)$ (note that the total DOS at $E_F$ is $N(E_F) = 2N_s(E_F)$). It follows from Fig. 1.1 that $n_\uparrow - n_\downarrow = N_s(E_F)(E_F + \delta E) - N_s(E_F)(E_F - \delta E) = 2N_s(E)\delta E$, and that the integration limits can be taken from $E_F$ to $E_{\uparrow,\downarrow} = E_F \pm \delta E$. This leads to

$$\begin{aligned} E &= \int_{E_F}^{E_F+\delta E} EN_s(E_F)dE + \int_{E_F}^{E_F-\delta E} EN_s(E_F)dE - \mu_B(n_\uparrow - n_\downarrow)H \\ &= \frac{N_s(E)}{2}\left[(E_F+\delta E)^2 + (E_F-\delta E)^2 - 2E_F^2\right] - \mu_B(n_\uparrow - n_\downarrow)H \\ &= \frac{1}{2N_s(E_F)}(n_\uparrow - n_\downarrow)^2 - \mu_B(n_\uparrow - n_\downarrow)H. \end{aligned} \tag{1.30}$$

Comparing Eqs. 1.28 & 1.30, the Pauli susceptibility $\chi_p$ is found to be

$$\chi_p = 2\mu_B^2 N_s(E_F). \tag{1.31}$$

Unlike the Curie law result for local moments, the Pauli susceptibility is temperature independent and depends on the DOS at the Fermi energy.

## 1.4 Ferromagnetism

A handful of elemental materials and a vast number of compounds exhibit phases with magnetic ordering, the spontaneous alignment of spins[2] in the absence of an external magnetic field. There are three general cases of ordering: ferromagnetism, antiferromagnetism, and ferrimagnetism. In ferromagnetic ordering all spins align parallel to one another, resulting in a macroscopic magnetization. In antiferromagnetism the spins are aligned anti-parallel to one another and the net magnetization is zero. Unlike the ferromagnetic case, antiferromagnetic order can be achieved via different topologies of moment ordering. In some systems, such as materials with a triangular Kagome lattice crystal structure, different antiferromagnetic orderings can

---

[2] In condensed matter, the terms spin and moment are often used interchangeably. When the orbital moment is quenched, which is the case in the many ferromagnetic substances [13], this substitution of terms is reasonably accurate. However in unquenched systems such as the heavy rare-earths, the differentiation between **S** and **J** should be made clear.

be degenerate or energetically similar, giving rise to magnetic frustration. In ferrimagnetism, the spins order in some non-ferromagnetic way, but the magnetization is finite. For example, this can occur in compounds with two different magnetic species with different net moments, so even if the magnetic ordering is reminiscent of an antiferromagnet, the different moment magnitudes lead to a net magnetization.

This section will discuss the origin of magnetic ordering and then present two magnetic models, the Heisenberg model for localized moments and the Stoner model for magnetic, itinerant electrons. For simplicity, only ferromagnetic ordering will be discussed.

### 1.4.1 The exchange interaction

The origin of magnetic ordering is the so-called exchange interaction. To illustrate the concept of exchange as discussed in Ref. [30], consider the hydrogen molecule, a system of two spatially separated protons and two electrons. The Hamiltonian of the system is

$$H = -\frac{\hbar^2}{2m}\left(\nabla_1^2 + \nabla_2^2\right) + V(\mathbf{r}_1, \mathbf{r}_2), \tag{1.32}$$

and because there are two electrons the spin quantum number can be either $S = 0$ (anti-symmetric spin singlet state) or $S = 1$ (symmetric spin triplet state). To keep the overall wave function anti-symmetric, the spatial wave function must be symmetric for the singlet state and anti-symmetric for the triplet state. The independent electron approximation is assumed and $V(\mathbf{r}_1, \mathbf{r}_2)$ is ignored. The singlet and triplet states are built using the tight-binding approach, such that the two-electron wave functions are linear combinations of products of the atomic stationary-state wave functions $\phi_1$ and $\phi_2$ centered at $\mathbf{R}_1$ and $\mathbf{R}_2$

$$\psi_s(\mathbf{r}_1,\mathbf{r}_2) = \phi_1(\mathbf{r}_1)\phi_2(\mathbf{r}_2) + \phi_2(\mathbf{r}_1)\phi_1(\mathbf{r}_2) + \phi_1(\mathbf{r}_1)\phi_1(\mathbf{r}_2) + \phi_2(\mathbf{r}_1)\phi_2(\mathbf{r}_2), \tag{1.33}$$

$$\psi_t(\mathbf{r}_1,\mathbf{r}_2) = 2\left[\phi_2(\mathbf{r}_1)\phi_1(\mathbf{r}_2) - \phi_1(\mathbf{r}_1)\phi_2(\mathbf{r}_2)\right]. \tag{1.34}$$

While correct in the independent electron case, Eq. 1.33 is a very poor description of the singlet state when electron-electron interactions are considered. Terms three and four predict that both electrons have a significant probability of being present near the same atom, which is energetically unfavorable due to Coulomb repulsion. As a remedy, terms three and four can be dropped from Eq. 1.33, leaving

$$\bar{\psi}_s(\mathbf{r}_1,\mathbf{r}_2) = \phi_1(\mathbf{r}_1)\phi_2(\mathbf{r}_2) + \phi_2(\mathbf{r}_1)\phi_1(\mathbf{r}_2). \tag{1.35}$$

This is known as the Heitler-London approximation, and is much more accurate than Eq. 1.33 for the $H_2$ molecule with widely separated protons. Eq. 1.34 for the triplet state is reasonable as it does not have two electrons occupying the same atom.

Taking the difference in energy between the singlet state in Eq. 1.35 and the triplet state in Eq. 1.34 yields

$$\begin{aligned}\frac{1}{2}\left(E_s - E_t\right) = \int d\mathbf{r}_1 d\mathbf{r}_2 \left[\phi_1(\mathbf{r}_1)\phi_2(\mathbf{r}_2)\right] \Bigg( &\frac{e^2}{|\mathbf{r}_1 - \mathbf{r}_2|} + \frac{e^2}{|\mathbf{R}_1 - \mathbf{R}_2|} + \\ &\frac{e^2}{|\mathbf{r}_1 - \mathbf{R}_1|} + \frac{e^2}{|\mathbf{r}_2 - \mathbf{R}_2|}\Bigg) \left[\phi_2(\mathbf{r}_1)\phi_1(\mathbf{r}_2)\right].\end{aligned} \tag{1.36}$$

Eqs. 1.34 & 1.35 differ only through the exchange of spatial electron coordinates $\mathbf{r}_1$ and $\mathbf{r}_2$ and so the energy difference in Eq. 1.36 is called the exchange splitting. In spin space, the difference is between parallel and anti-parallel spin alignments of the electrons, and if $E_s > E_t$, then ferromagnetic ordering is energetically preferred. This is the origin of spontaneous magnetic ordering and is sometimes viewed as a magnetic interaction called the exchange interaction. It is important to note that, despite the terminology, the exchange interaction is nothing more than the effect of electrostatic interactions and the Pauli exclusion principle.

The interaction just described is called direct exchange, owing to the direct Coulomb interaction between the electrons on two separate ions. There are other types of exchange responsible for magnetic ordering. Superexchange is when the exchange interaction between spins on two separate atoms is mediated by the electrons on a third, non-magnetic atom [31–33]. This is commonly found in magnetic insulators, such as the ionic solids CuO and MnO. Indirect exchange is when the exchange between electrons localized on atoms is mediated by conduction electrons, such as in the rare-earth metals, and is explained by the Ruderman-Kittel-Kasuya-Yosida (RKKY) theory [34–36]. Itinerant exchange occurs between the electrons in an electron gas such as in Fe, Ni, and Co; an example of a theory of itinerant exchange is the Stoner model to be discussed in Sec. 1.4.3. In many magnetic crystals the overall exchange interaction responsible for ordering is a combination of the different types discussed here. This is an immense theoretical challenge as a complete description of magnetism should be able to interpolate between the different types of exchange.

### 1.4.2 Heisenberg model

The previous analysis demonstrates how to determine whether the ground state of a two-electron system contains parallel or anti-parallel spin alignment. Extending this kind of treatment to a system of $N$ atoms is not straightforward. However if excitations to states outside the ground state multiplet are ignored, then a spin Hamiltonian called the Heisenberg model can be constructed. This model reproduces the spin structure and is commonly used to investigate the thermodynamics of a wide variety of magnetic materials.

To motivate the Heisenberg model, the hydrogen molecule is once again considered. When the hydrogen atoms are very far apart the ground state is fourfold degenerate, and the spin on each atom can individually orient up or down. When the atoms are brought together to form a $H_2$ molecule, the ground state splits into a multiplet, where the splitting is small compared to the gap between excited states. If higher energy multiplets are ignored, then the molecule has four possible spin orientations. The total spin operator for the $H_2$ molecule is

$$\mathbf{S}^2 = (\mathbf{S}_1 + \mathbf{S}_2)^2 = \frac{3}{2} + 2\mathbf{S}_1 \cdot \mathbf{S}_2. \tag{1.37}$$

Using $|\mathbf{S}^2| = S(S+1)$, the eigenvalue of $\mathbf{S}_1 \cdot \mathbf{S}_2$ is $-\frac{3}{4}$ in the singlet state and $+\frac{1}{4}$ in the triplet state. Therefore the spin Hamiltonian

$$H^{\text{spin}} = \frac{1}{4}\left(E_s + 3E_t\right) - \left(E_s - E_t\right)\mathbf{S}_1 \cdot \mathbf{S}_2 \tag{1.38}$$

has energy $E_s$ in the singlet state and $E_t$ in the triplet state. Redefining the zero energy to remove the constant terms yields

$$H^{\text{spin}} = -J\mathbf{S}_1 \cdot \mathbf{S}_2; \qquad J = E_s - E_t. \tag{1.39}$$

Parallel spins are favored when $J > 0$ and antiparallel spins are favored when $J < 0$.

In general, extending the above procedure to a system of $N$ atoms is complex, as the analogous starting point would be the degenerate ground state splitting into a multiplet of $(2S+1)^N$ levels whose eigenvalues need to be replicated by the constructed spin Hamiltonian. It turns out, however, that the $N$-atom system can also be described by a modification of the two-electron spin Hamiltonian by simply summing over all pairs of atoms:

$$H^{\text{Heis}} = -\frac{1}{2}\sum_{ij} J_{ij}\mathbf{S}_i \cdot \mathbf{S}_j - g\mu_B \sum_i \mathbf{S}_i \cdot \mathbf{H}_i, \tag{1.40}$$

where the factor of 1/2 is introduced to take care of double counting and a Zeeman energy term was introduced to account for an applied field. This is the Heisenberg Hamiltonian. The exchange tensor $J_{ij}$ is necessarily symmetric $J_{ij} = J_{ji}$ and in the absence of symmetry each pair of atoms can, in principle, have a unique exchange constant associated with it. The exchange constant parameterizes the energy it takes to flip a spin in a solid. Because $J_{ij}$ can be positive or negative depending on the pair, the Heisenberg model can be applied to both ferromagnets and antiferromagnets.

The Heisenberg model is a typical starting point for investigating the thermodynamics of magnetic systems by solving the statistics problem using exact Monte Carlo simulations or an approximation. The simplest approximation that yields qualitative results is the mean-field approximation, which is equivalent to the molecular Weiss field where the complex pair interactions are contained in a simple effective field term. To apply the approximation, the spin on site $i$ is rewritten in the form

$$\mathbf{S}_i = \langle \mathbf{S}_i \rangle + (\mathbf{S}_i - \langle \mathbf{S}_i \rangle) = \langle \mathbf{S}_i \rangle + \Delta\mathbf{S}_i, \tag{1.41}$$

where $\langle \mathbf{S}_i \rangle$ and $\Delta\mathbf{S}_i$ are the thermal average and fluctuations of $\mathbf{S}_i$. Substituting Eq. 1.41 into the first term of Eq. 1.40,

$$-\frac{1}{2}\sum_{ij} J_{ij}\left(2\mathbf{S}_i \cdot \langle \mathbf{S}_j \rangle + \langle \mathbf{S}_i \rangle \cdot \langle \mathbf{S}_j \rangle + \Delta\mathbf{S}_i \cdot \Delta\mathbf{S}_j\right). \tag{1.42}$$

The fluctuation terms are assumed to be small and terms of order $(\Delta\mathbf{S})^2$ and higher are dropped. The second term in Eq. 1.42 can be removed by setting the appropriate zero energy. For a system with translational symmetry, all spins are identical[3] ($\langle\mathbf{S}_i\rangle = \langle\mathbf{S}\rangle$) and the thermal spin average can be related to the total magnetization density $\langle\mathbf{S}\rangle = V\mathbf{M}/(Ng\mu_B)$. In the single-site approximation the external field must be uniform, i.e. $\mathbf{H}_i = \mathbf{H}$. The mean-field Hamiltonian is then

$$H_{MFA} = -g\mu_B \sum_i \mathbf{S}_i \cdot \mathbf{H}^{\text{eff}}, \tag{1.43}$$

where the effective field $\mathbf{H}^{\text{eff}}$ is

$$\begin{aligned} \mathbf{H}^{\text{eff}} &= \mathbf{H} + \frac{V}{N(g\mu_B)^2}\mathbf{M}\sum_j J_{ij} \\ &= \mathbf{H} + \lambda\mathbf{M} \end{aligned} \tag{1.44}$$

with

$$\lambda = \frac{V}{N}\frac{J_0}{(g\mu_B)^2}; \qquad\qquad J_0 = \sum_j J_{ij}. \tag{1.45}$$

Eq. 1.43 is formally the same as the Hamiltonian treated in Sec. 1.3.1, so the statistics problem is solved in the same way and the magnetization is Eq. 1.23 with the appropriate substitution of variables:

$$\mathbf{M}(T) = \frac{N}{V} g\mu_B S B_S(\beta g\mu_B S H^{\text{eff}}). \tag{1.46}$$

If the spins are treated as classical vectors ($S \to \infty$), then the Brillouin function in

---

[3] This assumption is for ferromagnetic systems only. This symmetry needs to be broken for anti-ferromagnetic systems.

Eq. 1.24 simplifies to the Langevin function. Setting $m_0 = g\mu_B S$ as the magnetization due to a single spin at zero temperature, the magnetization is equivalent to Eq. 1.6 from the classical Langevin-Weiss theory:

$$\mathbf{M}(T) = \frac{N}{V} m_0 \left[\coth(\beta m_0 H^{\text{eff}}) - \frac{1}{\beta m_0 H^{\text{eff}}}\right]. \tag{1.47}$$

Eq. 1.3 can be used to calculate the susceptibility of the mean-field Heisenberg model in the paramagnetic state, where $k_B T \gg \mu_B H^{\text{eff}}$. Starting with Eq. 1.46, this recovers the Curie-Weiss law

$$\chi_M = \frac{\chi_0}{T - T_c} \tag{1.48}$$

with bare susceptibility $\chi_0$ and Curie temperature $T_c$:

$$\chi_0 = N(g\mu_B)^2 \frac{S(S+1)}{3k_B}, \tag{1.49}$$

$$T_c = \frac{S(S+1)}{3k_B} J_0. \tag{1.50}$$

The Curie temperature in Eq. 1.50 is generally overestimated when compared with exact solutions of the Heisenberg model (using, for example, Monte Carlo simulations). This is a well-known deficiency of the mean-field approach.

### 1.4.3 Stoner model

The previous discussion of the exchange interaction and the Heisenberg model assumed that the electrons responsible for magnetism were localized on individual atomic sites. This is a reasonable assumption for magnetic insulators and the heavy rare-earth elements, but it is inadequate in explaining how delocalized electrons can support a ferromagnetic ground state, such as in the $3d$ transition metals Fe, Co, and Ni. It turns out that the energetic competition between Coulomb repulsion, the Pauli principle, and the electronic kinetic energy can give rise to a ferromagnetic state. A band theory of electrons is necessary to explain such ferromagnetic ordering.

The previous discussion of Pauli paramagnetism was based on the band theory of electrons, and the energy density in Eq. 1.28 contained only terms for the kinetic energy and the Zeeman energy, ignoring Coulomb repulsion between electrons. If the Coulomb interaction is introduced, then because of the Pauli principle, electrons that are close together will have anti-parallel spins at the expense of a greater Coulomb repulsion energy. Parallel spins will tend to avoid each other, lowering the Coulomb energy.

Keeping these qualitative points in mind, a good starting point is to take the energy density in Eq. 1.28 and add in the Coulomb repulsion term $Un_\uparrow n_\downarrow$ similar to what is used in the simple Hubbard model [27]. Making use of the definitions $m \equiv n_\uparrow - n_\downarrow$ and $n \equiv n_\uparrow + n_\downarrow$, the Coulomb term can be rewritten as $U/4(n^2 - m^2)$. The first term is a constant and can be eliminated by an appropriate energy shift, while the second term is dependent on the magnetization of the material. The modified energy density can be written as

$$\frac{E}{V} = \frac{\mu_B^2}{2\chi_p}\left(n_\uparrow - n_\downarrow\right)^2 - \frac{I}{4}\left(n_\uparrow - n_\downarrow\right)^2 - \mu_B\left(n_\uparrow - n_\downarrow\right)H, \tag{1.51}$$

where $I \equiv U$, by convention. Recalling the expression for $\chi_p$ in Eq. 1.31, Eq. 1.51 can be rewritten as

$$\frac{E}{V} = \frac{\mu_B^2}{2\chi}\left(n_\uparrow - n_\downarrow\right)^2 - \mu_B\left(n_\uparrow - n_\downarrow\right)H, \tag{1.52}$$

where

$$\chi = \frac{\chi_p}{1 - IN_s(E_F)} \tag{1.53}$$

is the exchange-enhanced Pauli susceptibility.

Looking at Eq. 1.53, $\chi$ diverges when $IN_s(E_F) = 1$ indicating that for $IN_s(E_F) > 1$ the paramagnetic state is unstable, and a spontaneous magnetization will develop. This is the famous Stoner criterion. The intra-atomic Coulomb parameter $I$, also called the Stoner parameter, is relatively constant for most metals, with $I \approx 1$ eV [37]. The DOS at the Fermi level, on the other hand, varies significantly from metal to metal. Fe, Co, and Ni, for example, have a DOS at the Fermi energy large enough to fulfill the Stoner criterion and support ferromagnetism. Other metals, like Pd, are close to the transition point, making them easy to polarize.

## 1.5 Diffusive theory of spin transport

Up to this point the discussion has centered on the origin and thermodynamics of magnetism and magnetic ordering. Another area of interest in magnetism is the theory of spin transport, a sub-branch of spin electronics or spintronics. Spin transport theory is relevant to the material to be discussed in Chapter 4. Spintronics is the field of research concerned with the manipulation of the electron's spin in electronic devices, in addition to its charge. One aim of the field is to build a commercially viable spin transistor [16] that can operate at room temperature. Achieving this goal means understanding how to generate, manipulate, and detect spin currents in spin injection geometries.

The problem of spin injection was first worked out by Johnson and Silsbee [38, 39],

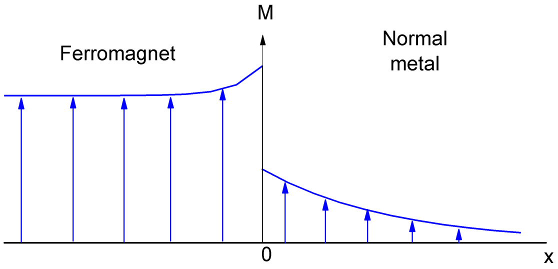

Figure 1.2: A schematic of the magnetization of a ferromagnet/normal metal junction while current flows from left to right. The interface is at $x = 0$, the ferromagnet is at $x < 0$ and the normal metal is at $x > 0$. The non-equilibrium magnetization, called the spin accumulation, exponentially decays away from the interface on both the ferromagnetic and normal metal sides.

and further investigations were done by van Son [40], Valet and Fert [41], Hershfield and Zhao [42], and Rashba [43, 44]. When a voltage is applied to a ferromagnet/normal metal junction and a steady-state current passes through the interface into the normal metal, a non-equilibrium magnetization develops in the normal metal near the interface, as shown in the schematic in Fig. 1.2. This is due to spin polarized electrons entering the normal metal through the interface, which then relax via spin-flip processes over the length scale of the spin-diffusion length[4] [46, 47]. This non-equilibrium magnetization is called the spin accumulation and it is the result of successful spin injection. It is an important concept in spintronics and is relevant to other interesting spin-dependent phenomena such as giant magnetoresistance [48, 49].

The diffusive spin-dependent transport theory, also called the two spin channel model, is used to model spin injection. The two channel model is a modification first postulated by N. F. Mott [50] of the semi-classical diffusive model of transport relevant to ferromagnets. The general observation is that the conduction electrons often can be separated into two independent classes based on their spin. Therefore

---

[4] The spin-diffusion length, and hence the spin accumulation, in normal metals and semiconductors can be large. Spin-diffusion lengths can be on the order of micrometers in very pure samples of Ag, and lengths of over 100 micrometers have been observed in n-doped semiconductors [45].

the conductivity $\sigma$, and hence any currents $j$ traveling through a system, are split into spin-dependent components

$$\sigma = \sigma_\uparrow + \sigma_\downarrow, \tag{1.54}$$

$$j = j_\uparrow + j_\downarrow. \tag{1.55}$$

A weak coupling between the spin channels may be introduced, allowing for spin relaxation. Following the formalism of Rashba [43, 44], the relevant equations for diffusion in the two-channel model are

$$\nabla^2 \mu_s = \frac{\mu_s}{L_s^2}, \tag{1.56}$$

$$L_s^2 = \frac{(\sigma_\downarrow D_\uparrow + \sigma_\uparrow D_\downarrow)\,\tau_s}{\sigma}, \tag{1.57}$$

$$P_j = \frac{2\sigma_\uparrow \sigma_\downarrow}{j\sigma}\nabla\mu_s + P_\sigma, \tag{1.58}$$

$$\nabla\mu = -\frac{P_\sigma}{2}\nabla\mu_s + \frac{j}{\sigma}. \tag{1.59}$$

where

$$\mu = \frac{\mu_\uparrow + \mu_\downarrow}{2}, \tag{1.60}$$

$$\mu_s = \mu_\uparrow - \mu_\downarrow, \tag{1.61}$$

$$P_X \equiv \frac{X_\uparrow - X_\downarrow}{X}, \tag{1.62}$$

and $\mu$ is the average electrochemical potential. The spin accumulation $\mu_s$ is formally the difference of the electrochemical potential for the ↑ and ↓ channels. Eq. 1.62 gives the polarization $P_X$ of variable $X$, for example the conductivity polarization $P_\sigma$ and the current polarization $P_j$. The spin-diffusion length $L_s$ is related to the spin-dependent diffusion constants $D_\lambda$ ($\lambda =\uparrow,\downarrow$), spin-dependent conductivities, and the spin relaxation time $\tau_s$.

The junction between a ferromagnet and a normal metal ($F/N$ junction) represents the simplest possible system for spin injection. Assume that the interface is at $x = 0$, the ferromagnet at $x < 0$, and a normal metal at $x > 0$, just as in Fig. 1.2. Eqs. 1.56-1.59 need to be applied to each region separately, then joined via the boundary condition

$$j_\lambda(0) = \Sigma_\lambda \left[\mu_{\lambda N}(0) - \mu_{\lambda F}(0)\right] \tag{1.63}$$

where $\Sigma_\lambda$ is the spin-resolved contact conductivity. Spin-dependent conductivities are defined for the ferromagnet $\sigma_F = \sigma_{F\uparrow} + \sigma_{F\downarrow}$ and the conductivity for the normal metal is $\sigma_N = \sigma_\lambda/2$. Finally, boundary conditions also require that the spin accumulation decays to zero far away from the interface.

Solving Eq. 1.56 for the $F$ region and $N$ regions,

$$\mu_{sF} = \mu_{sF}(0)e^{x/L_{sF}}, \tag{1.64}$$

$$\mu_{sN} = \mu_{sN}(0)e^{-x/L_{sN}}. \tag{1.65}$$

The difference between the spin-up and -down currents at the interface are, according to Eq. 1.63,

$$[\mu_{\uparrow N}(0) - \mu_{\uparrow F}(0)] - [\mu_{\downarrow N}(0) - \mu_{\downarrow F}(0)] = \frac{j_\uparrow(0)}{\Sigma_\uparrow} - \frac{j_\downarrow(0)}{\Sigma_\downarrow}. \tag{1.66}$$

After multiplying both sides by $2\Sigma_\uparrow\Sigma_\downarrow$ and some algebra, we see that

$$\begin{aligned}
2\Sigma_\uparrow\Sigma_\downarrow\left[\mu_{sN}(0)-\mu_{sF}(0)\right] &= 2\Sigma_\downarrow j_\uparrow(0) - 2\Sigma_\uparrow j_\downarrow(0) \\
&= \left[\Sigma_\uparrow j_\uparrow(0) + \Sigma_\downarrow j_\uparrow(0) - \Sigma_\uparrow j_\downarrow(0) - \Sigma_\downarrow j_\downarrow(0)\right] \\
&- \left[\Sigma_\uparrow j_\uparrow(0) - \Sigma_\downarrow j_\uparrow(0) + \Sigma_\uparrow j_\downarrow(0) + \Sigma_\downarrow j_\downarrow(0)\right] \\
&= \left[\Sigma_\uparrow + \Sigma_\downarrow\right]\left[j_\uparrow(0) - j_\downarrow(0)\right] - \left[\Sigma_\uparrow - \Sigma_\downarrow\right]\left[j_\uparrow(0) + j_\downarrow(0)\right] \\
&= \Sigma\left[P_j - P_\Sigma\right] j. \qquad (1.67)
\end{aligned}$$

An effective contact resistance can be defined as

$$r_c = \frac{\Sigma}{4\Sigma_\uparrow\Sigma_\downarrow} \qquad (1.68)$$

and Eq. 1.67 rewritten as

$$\mu_{sN}(0) - \mu_{sF}(0) = 2r_c\left(P_j - P_\Sigma\right) j. \qquad (1.69)$$

To evaluate Eq. 1.58 at the interface, the polarization relation is applied to the $F$ and $N$ regions, Eqs. 1.64 & 1.65 are plugged in for $\mu_s$, the expressions are evaluated at $x = 0$, and the following effective ferromagnet and normal metal resistances $r_F$ and $r_N$ are defined:

$$r_F = \frac{L_{sF}\sigma_F}{4\sigma_{\uparrow F}\sigma_{\downarrow F}}, \qquad (1.70)$$

$$r_N = \frac{L_{sN}}{\sigma_N}. \qquad (1.71)$$

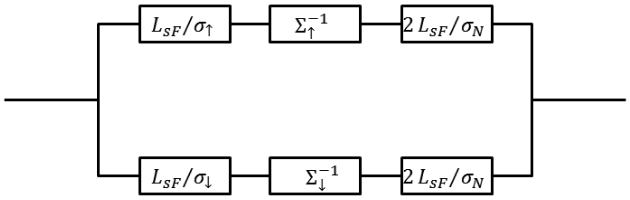

Figure 1.3: The phemonological parallel resistor model is equivalent to the two channel model. The $F$ and $N$ regions contribute bulk spin-dependent resistances and the interface can have a spin-selective contact resistance.

The resulting expressions are

$$\mu_{sF}(0) = 2r_F\left[P_j - P_{\sigma F}\right]j, \tag{1.72}$$

$$\mu_{sN}(0) = -2r_N P_j j. \tag{1.73}$$

The final step is to apply Eqs. 1.72 & 1.73 to Eq. 1.69, and after some algebra the result is

$$P_j = \frac{r_c P_\Sigma + r_F P_{\sigma F}}{r_F + r_c + r_N}. \tag{1.74}$$

This is the current polarization for the $F/N$ junction.

According to Eq. 1.74, when the contact is ohmic ($r_c \approx 0$) and the ferromagnet and normal metal have similar effective resistances $r_F \sim r_N$, then $P_j \sim P_{\sigma F}$ and the current polarization is determined by the polarization of the ferromagnet and efficient spin injection is possible. However, if the normal metal is replaced with a semiconductor (which is necessary for a spin transistor device) such that $r_N \gg r_F$ and the contact remains ohmic, it follows that $P_j \ll 1$ and spin injection is suppressed. The suppression of spin injection for ohmic $F/N$ contacts is the well-known conductivity mismatch problem [51, 52].

The $F/N$ junction is also equivalent to the parallel resistor model depicted in Fig. 1.3 with the specified spin-dependent resistances which replicates the current polarization expression in Eq. 1.74 [53]. The resistor model gives insight into why the conductivity mismatch happens. With an ohmic contact and a semiconductor for region $N$, the bulk resistance of $N$ is spin independent and much larger than the spin-dependent resistances of $F$. As a result, the effective resistance of both the up and down channels is $\approx 2L_{sf}/\sigma_N$, drawing the same current and suppressing spin injection. Looking at either Eq. 1.74 or Fig. 1.3 suggests that inserting a spin-selective contact with a large resistance, such as a tunnel barrier or a spin-selective Schottky barrier, should remove the conductivity mismatch problem and restore spin injection with $P_j \sim P_\Sigma$. This is observed experimentally [54, 55]. Another solution is to use a magnetic semiconductor instead of a metallic ferromagnet such that $r_F \sim r_N$, which has also been confirmed by experiment [56].

## 1.6 High-temperature resistivity of the heavy rare-earth metals

In Chapters 5 & 6, the magnetic contribution to the total resistivity of the heavy rare-earth metals (Gd-Tm series) is investigated using first-principles methods. These elements all have a hexagonal close-packed (hcp) crystal structure and the $4f$ electrons responsible for magnetism in the heavy rare-earth metals, unlike the $3d$ transition metals, are highly localized and do not participate in transport. Measurements of the Curie constant in the paramagnetic phase also suggest that the orbital moments are unquenched. Magnetic ordering is due to the indirect exchange described in the Ruderman-Kittel-Kasuya-Yosida (RKKY) theory [34–36, 57, 58]. The coupling of the

$5d$ conduction electrons and the localized $4f$ electrons necessary for RKKY exchange also is responsible for spin-disorder scattering at finite temperatures. In this section some background on the problem is presented.

Matthiessen's rule is typically assumed when evaluating the resistivity of metals. The key assumptions are that the scattering mechanisms that contribute to the resistivity are independent and that the inverse scattering rates may be summed together. In this case, the total resistivity is written as

$$\rho = \rho_{\text{res}} + \rho_{\text{ph}} + \rho_m, \tag{1.75}$$

where $\rho_{\text{res}}$ is the residual resistivity due to impurities, $\rho_{\text{ph}}$ is the phonon contribution to the resistivity, and $\rho_m$ is the magnetic contribution to the resistivity. The residual resistivity $\rho_{\text{res}}$ is a temperature-independent constant and is typically subtracted out. The phonon resistivity in metals is well known and is described by the Bloch-Grüneisen formula, which at high temperatures $T \gg \Theta_D$ ($\Theta_D$ is the Debye temperature) is $\rho_{\text{ph}} \propto T$.

The magnetic contribution to the resistivity is due to scattering from spin fluctuations, which adds an "anomalous" contribution $\rho_m(T)$ to the electrical resistivity [13, 59, 60]. At $T = 0$ K, the spins are aligned and periodic and do not contribute to scattering, so $\rho_m = 0$. As $T$ is increased, the spins fluctuate about $\langle \mathbf{S} \rangle$ and $\rho_m$ is finite. Above the ordering temperature (Curie temperature $T_c$ for ferromagnets), the spins are fully disordered and uncorrelated, leading to a saturation of the magnetic scattering and therefore $\rho_m$. The simplest model of spin-disorder scattering is based on the $s$-$d$ ($d$-$f$) Hamiltonian, which was worked out by Kasuya [61] and de Gennes and Friedel [62].

The *d*-*f* Hamiltonian may be written as

$$H = -\Gamma \mathbf{s} \cdot \mathbf{S}, \tag{1.76}$$

where $\Gamma$ is the interaction parameter, $\mathbf{s}$ is the spin of the conduction electron, and $\mathbf{S}$ is the localized spin on an atom. Eq. 1.76 is meaningful if spin-orbit coupling is weak and the orbital momentum is quenched. If, on the other hand, the orbital moment is unquenched and spin-orbit coupling is strong enough to enforce collinearity of $\mathbf{L}$ and $\mathbf{S}$, which may be anticipated in the heavy rare-earth elements, then $\mathbf{S}$ should be replaced by the projection of $\mathbf{J}$ on $\mathbf{S}$, $(g_J - 1)\mathbf{J}$, and the interaction Hamiltonian is then

$$H = -\Gamma(g_J - 1)\mathbf{s} \cdot \mathbf{J}. \tag{1.77}$$

For determining $\rho_m$ the Hamiltonian in Eq. 1.76 will be used. The results of using Eq. 1.77 may be shown via simple substitution of $S(S+1) \rightarrow (g_J - 1)^2 J(J+1)$.

The interaction for the full lattice is

$$H = -\sum_{k,k',n} \Gamma e^{i\mathbf{q}\cdot\mathbf{R}_n} \mathbf{S}_n \cdot \mathbf{s}_{k,k'}, \tag{1.78}$$

where the point interaction approximation, $\Gamma(\mathbf{r}) = \Gamma\delta(\mathbf{r})$, has been assumed. For the scattering problem the Born approximation is used to calculate the differential cross-section. It is also assumed that only elastic collisions play a role in the scattering mechanisms. The result for the differential cross-section is

$$\frac{d\sigma}{d\Omega} = \frac{\sigma_0}{4\pi} \sum_n \gamma_n e^{i\mathbf{q}\cdot\mathbf{R}_n}, \tag{1.79}$$

where

$$\gamma_n = \frac{\langle \mathbf{S}_0 \cdot \mathbf{S}_n \rangle - \langle \mathbf{S} \rangle^2}{S(S+1)}; \qquad \sigma_0 = \frac{1}{4\pi}\left(\frac{m\Gamma}{\hbar^2}\right)^2 S(S+1). \tag{1.80}$$

If the conduction electrons are assumed to occupy a single parabolic conduction band, then in the relaxation-time approximation the semi-classical theory predicts the resistivity to be [30, 63]

$$\rho_m = \frac{m^*}{ze^2\tau} \tag{1.81}$$

where $m^*$ is the effective electron mass, $z$ is the number of electrons per atom, and $\tau$ is the relaxation time. The reciprocal relaxation time is

$$\frac{1}{\tau} = \frac{\hbar k_F}{m} 2\pi \int_0^\pi \sin\theta d\theta \, (1 - \cos\theta) \, \frac{d\sigma}{d\Omega}. \tag{1.82}$$

Taking the $T \to \infty$ limit (which corresponds with $T \gg T_c$, the paramagnetic state), it follows that all the spins are randomly disordered and uncorrelated, so $\langle \mathbf{S} \rangle = 0$, $\langle \mathbf{S}_0 \cdot \mathbf{S}_n \rangle = 0$ for $n \neq 0$, and $\langle S_0^2 \rangle = S(S+1)$. Combining this with Eqs. 1.80, 1.81, & 1.82, the magnetic resistivity in the disordered state, also referred to as the spin-disorder resistivity (SDR), is predicted to be

$$\rho_m^0 = \frac{\hbar k_F}{4\pi z}\left(\frac{m\Gamma}{e\hbar^2}\right)^2 S(S+1). \tag{1.83}$$

If the Hamiltonian in Eq. 1.77 were used instead, then the above expression becomes

$$\rho_m^0 = \frac{\hbar k_F}{4\pi z}\left(\frac{m\Gamma}{e\hbar^2}\right)^2 (g_J - 1)^2 J(J+1). \tag{1.84}$$

The results of Eqs. 1.83 & 1.84 are simple expressions based on the assumption of an isotropic crystal structure. The hcp structure of the heavy rare-earth metals is highly anisotropic, as are the Fermi surfaces [58], suggesting that the electron velocities at the Fermi energy and cross-sections of the Fermi surface differ significantly along different crystallographic directions. The following general semi-classical conductivity tensor $\sigma_{ij}$ in the relaxation time approximation can better account for such features:

$$\sigma_{ij} = \frac{e^2\tau}{4\pi^2\hbar}\iint_{E(\mathbf{k})} v_i dS_j \tag{1.85}$$

where $v_i$ is the component of the velocity along axis $i$ and $dS_j$ is the projection of the element $dS$ of the Fermi surface on axis $j$. The temperature-dependent resistivity curves from single-crystal measurements of the electrical resistivity in the Gd-Tm series [7–12, 64–68] reveal that the magnetic scattering parallel to the $c$-axis and along the in-plane direction can be quite different.

The single-crystal electrical resistivity experiments allow the compilation of the SDR in the in-plane and c-axis directions, which can be compared with Eqs. 1.83 & 1.84. If the atomic spins are better described by $\mathbf{S}$, then $\rho_m^{(0)} \sim S^2(S+1)/S$, and if the spins are described by $\mathbf{J}$ and $J = L+S$ as per Hund's rules, then plugging this into the Landé g-factor in Eq. 1.20 predicts $\rho_m^{(0)} \sim S^2(J+1)/J$. Comparing with experiment, the factor $S^2(J+1)/J$ appears to agree reasonably well with experimental data [69, 70], but only after an empirical electronic correction to account for the variation of the in-plane Fermi surface projection in the Gd-Tm series ($dS_j$ in Eq. 1.85 where $j$ is the in-plane direction) is included [70].

## 1.7 Organization of dissertation

The aim of this dissertation is to further the understanding of the areas of magnetism outlined above using modeling and ab-initio methods. The models used in chapters 3 & 4 will be explained in their respective chapters. The ab-initio method of choice is density functional theory (DFT), which is the topic of Chapter 2 where the theorems of DFT are reviewed. Modern DFT calculations are possible because of the Kohn-Sham equations, which replace the many-body electronic structure problem with an independent electron approach to solve for the electronic density of solids self-consistently; the Kohn-Sham equations are also reviewed in the chapter. Finally, such calculations require the choice of a basis set and in this dissertation linear muffin tin orbitals are used, which are reviewed at the close of the chapter.

In Chapter 3, a classical model that can interpolate between the localized Heisenberg model and band Stoner model is explored. Using this model, the thermodynamics of itinerant magnets is studied with a single parameter characterizing the degree of itinerancy. Monte Carlo simulations for bcc and fcc lattices are compared with the mean-field approximation and with the Onsager cavity field approximation extended to itinerant systems. The qualitative features of thermodynamics are similar to the known results of the functional integral method, another unified approach to magnetism. It is found that magnetic short-range order is weak and almost independent on the degree of itinerancy, and the mean-field approximation describes the thermodynamics reasonably well. Ambiguity of the phase space measure for classical models is emphasized. The Onsager cavity field method is extended to itinerant systems, which involves the renormalization of both the Weiss field and the on-site exchange interaction. The predictions of this approximation are in excellent agreement with Monte Carlo results.

In Chapter 4, a posited solution to the conductivity mismatch problem is studied in detail. Spin injection from a half-metallic electrode in the presence of thermal spin disorder is analyzed using a combination of random matrix theory, spin-diffusion theory, and explicit simulations for the tight-binding *s*-*d* model. It is shown that efficient spin injection from a half-metal is possible as long as the effective resistance of the normal metal does not exceed a characteristic value, which does not depend on the resistance of the half-metallic electrode, but is rather controlled by spin-flip scattering at the interface. This condition can be formulated as $\alpha \lesssim l/l_{sf}^N T_c^{-1}$, where $\alpha$ is the relative deviation of the magnetization from saturation, $l$ and $l_{sf}^N$ are the mean-free path and the spin-diffusion length in the non-magnetic channel respectively, and $T_c$ is the transparency of the tunnel barrier at the interface (if present). The general conclusions are confirmed by tight-binding *s*-*d* model calculations. A rough estimate suggests that efficient spin injection from true half-metallic ferromagnets into silicon or copper may be possible at room temperature across a transparent interface.

In Chapter 5, the spin-disorder resistivity is calculated for the Gd-Tm series of metals in the paramagnetic state. Calculations are performed within the tight-binding linear muffin-tin orbital method using two complementary methods: (1) averaging of the Landauer-Büttiker conductance of a supercell over random noncollinear spin-disorder configurations, and (2) linear response calculations with the spin-disordered state described in the coherent potential approximation. The agreement between these two methods is found to be excellent. The spin-disorder resistivity in the series follows an almost universal dependence on the exchange splitting. While the crystallographic anisotropy of the spin-disorder resistivity agrees well with experiment, its magnitude is significantly underestimated compared to experiment. A simple quantum correction improves agreement with experiment but does not fully account for the discrepancy, suggesting that more complicated scattering mechanisms may be important.

Chapter 6 is the follow-up study to Chapter 5, where atomic displacements are included along with spin disorder. Experimental determination of the SDR involves fitting to high-temperature resistivity data and extrapolating to $T = 0$ K. The ab-initio calculations of the SDR in Chapter 5, which were underestimated compared to experiment, only included spin disorder; there was no fit to high-"temperature" results and an extrapolation back to zero temperature. A better comparison of theory and experiment is to calculate the resistivity dependence of a spin-disordered system on the mean-square atomic displacements. The mutual effects of phonon and spin-disorder scattering in Fe and Gd are investigated using the supercell approach in Chapter 5, with the atomic positions displaced with a Gaussian distribution. At small displacements the resistivity increases non-linearly, modestly in Fe and substantially in Gd, and at large displacements the resistivity increases linearly. Fitting the linear region of $\rho(\Delta^2_{\mathrm{ph}})$ in Gd yields an intercept $\sim 2.5$ times larger than the "bare" SDR, significantly improving agreement with experiment. This resistivity behavior is electronic in origin, and an investigation of the spectral function reveals that the rapid increase in the resistivity of Gd can be traced an interaction between its hole and electron Fermi surfaces activated by disorder. The linear behavior at large displacements is a saturation effect due to strong disorder.

## Chapter 2

# First-principles methods

## 2.1 Introduction

In the past several decades the toolkit available to condensed matter theorists to investigate the vast number of properties of material systems has expanded greatly. This has been due in large part to the development and subsequent implementation of density functional theory (DFT), a general first-principles approach that simplifies the complicated many-electron problem by reducing the problem from needing to solve for the many-body wave function to solving for the electron density, a local variable. The Thomas-Fermi approximation [71, 72] is the first known density functional approach, which Dirac extended to include exchange via a local approximation [73], providing a method in which the electron density serves as a basic variable that, in principle, can determine all the properties of a system. Later, Hohenberg and Kohn in their seminal paper [74] put the density functional approach on firm theoretical footing, and Kohn and Sham developed a practical method for implementing it [75], which is still in use to this day.

This chapter is a review of the theorems of DFT and the Kohn-Sham equations, which are central to the methodology used in later chapters to solve for the electronic structure. The formulation of first-principles methods begins with the fundamental dynamical equations appropriate to the system, in this case the Schödinger equation, with the end goal being the accurate calculation of material properties and quantitative predictions for real systems with a minimal amount of input parameters (some methods need only the charge, mass, and number of the different particles in the system). In practice, a series of careful approximations are needed to make the calculations tractable. The following discussion of first-principles DFT is based on the reasoning in Ref. [76], to which the reader is referred for further details.

The Hamiltonian for a material system with $N_I$ nuclei and $N$ electrons is

$$\widehat{H} = -\frac{\hbar^2}{2m_e}\sum_i \nabla_i^2 - \sum_{i,I}\frac{Z_I e^2}{|\mathbf{r}_i - \mathbf{R}_I|} + \frac{1}{2}\sum_{i\neq j}\frac{e^2}{|\mathbf{r}_i - \mathbf{r}_j|} - \sum_I \frac{\hbar^2}{2M_I}\nabla_I^2 + \frac{1}{2}\sum_{I\neq J}\frac{Z_I Z_J e^2}{|\mathbf{R}_I - \mathbf{R}_J|}, \tag{2.1}$$

where $Z_I$, $M_I$, $\mathbf{R}_I$ are the charge, mass, and position of nucleus $I$, $m_e$ and $e$ are the absolute charge and mass of the electron, and $\mathbf{r}_i$ is the position of electron $i$. The solutions to the Schrödinger equation $\widehat{H}\Psi = E\Psi$ are the many-body wave functions $\Psi \equiv \Psi(\mathbf{r}_1, \mathbf{r}_2, \ldots, \mathbf{r}_n, \mathbf{R}_1, \mathbf{R}_2, \ldots, \mathbf{R}_N)$. It is not possible to analytically or numerically solve for the many-body wave function in condensed matter systems, so approximations must be made. In Eq. 2.1 the parameter $1/M_I$ is several orders of magnitude smaller than $1/m_e$, and in a zeroth order approximation can be ignored, removing the kinetic energy of the nuclei (fourth term) and freezing their positions. This is known as the Born-Oppenheimer (adiabatic) approximation [77], and in Rydberg atomic units ($\hbar = 2m_e = 1, e^2 = 2$) Eq. 2.1 is rewritten as

$$\widehat{H} = \widehat{T} + \widehat{V}_{\text{ext}} + \widehat{V}_{\text{int}} + E_{II}, \tag{2.2}$$

where $\widehat{T}$ is the electron kinetic energy operator

$$\widehat{T} = \sum_i -\nabla_i^2, \tag{2.3}$$

$\widehat{V}_{\text{int}}$ is the electron-electron interaction potential

$$\widehat{V}_{\text{int}} = \sum_{i \neq j} \frac{1}{|\mathbf{r}_i - \mathbf{r}_j|}, \tag{2.4}$$

$\widehat{V}_{\text{ext}}$ is the potential due to the nuclei acting on the electrons

$$\widehat{V}_{\text{ext}} = \sum_{i,I} V_I \left( |\mathbf{r}_i - \mathbf{R}_I| \right), \tag{2.5}$$

and $E_{II}$ is the classical electrostatic interaction between nuclei. When solving for the electronic wave function, $E_{II}$ can be ignored and reintroduced when the total energy of the system is calculated. The Born-Oppenheimer approximation reduces the problem to solving for the electron wave function only, but in the current formulation it is still not solvable.

The particle density operator is defined as $\widehat{n}(\mathbf{r}) \equiv \sum_{i=1}^{N} \delta(\mathbf{r} - \mathbf{r}_i)$. If the wave function is known, then the electron density can be directly calculated (for simplicity spin is ignored, noting that adding it in is straightforward)

$$n(\mathbf{r}) = \frac{\langle \Psi | \, \widehat{n}(\mathbf{r}) \, | \Psi \rangle}{\langle \Psi | \Psi \rangle} = N \frac{\int d\mathbf{r}_2 d\mathbf{r}_3 \ldots d\mathbf{r}_N |\Psi(\mathbf{r}_1, \mathbf{r}_2, \ldots, \mathbf{r}_N)|^2}{\int d\mathbf{r}_1 d\mathbf{r}_2 \ldots d\mathbf{r}_N |\Psi(\mathbf{r}_1, \mathbf{r}_2, \ldots, \mathbf{r}_N)|^2}. \tag{2.6}$$

The total energy of the system is

$$\begin{aligned} E &= \frac{\langle\Psi|\,\widehat{H}\,|\Psi\rangle}{\langle\Psi|\Psi\rangle} \\ &\equiv \langle\widehat{H}\rangle = \langle\widehat{T}\rangle + \langle V_{\text{int}}\rangle + \int d\mathbf{r} V_{\text{ext}}(\mathbf{r}) n(\mathbf{r}) + E_{II}, \end{aligned} \tag{2.7}$$

where the interaction of the electrons in the external potential due to the nuclei is written as an integral over the electron density. The electron density is the central variable in DFT, which can be used in functional equations to determine basic properties such as the ground state energy.

## 2.2 Density functional theory theorems

There are two theorems for DFT that establish the electron density as a basic variable for a system. The theorems are (quoting Ref. [76]):

- "*Theorem I*: For any system of interacting particles in an external potential $V_{\text{ext}}(\mathbf{r})$, the potential $V_{\text{ext}}(\mathbf{r})$ is determined uniquely, except for a constant, by the ground state particle density $n_0(\mathbf{r})$.
- *Theorem II*: A universal functional for the energy $E[n]$ in terms of the density $n(\mathbf{r})$ can be defined, valid for any external potential $V_{\text{ext}}(\mathbf{r})$. For any particular $V_{\text{ext}}(\mathbf{r})$, the exact ground state energy of the system is the global minimum value of this functional, and the density $n(\mathbf{r})$ that minimizes this functional is the exact ground state density $n_0(\mathbf{r})$."

The following is a proof of each theorem.

### 2.2.1 Proof of theorem I

Assume that there are two external potentials, $V_{\text{ext}}^{(1)}(\mathbf{r})$ and $V_{\text{ext}}^{(2)}(\mathbf{r})$ that define two separate Hamiltonians $\widehat{H}^{(1)}$ and $\widehat{H}^{(2)}$. The respective ground state wave functions for each Hamiltonian are $\Psi^{(1)}$ and $\Psi^{(2)}$, and when plugged into Eq. 2.6 the result is the *same* ground state electron density $n_0(\mathbf{r})$. Now, since $\Psi^{(2)}$ is not the ground state wave function of $H^{(1)}$ (for simplicity, the ground state is assumed to be non-degenerate, see Ref. [78] for proof including degeneracy), it follows that

$$\langle\Psi^{(1)}|\,\widehat{H}^{(1)}\,|\Psi^{(1)}\rangle < \langle\Psi^{(2)}|\,\widehat{H}^{(1)}\,|\Psi^{(2)}\rangle\,. \tag{2.8}$$

The right-hand side can be rewritten as

$$\begin{aligned}\langle\Psi^{(2)}|\,\widehat{H}^{(1)}\,|\Psi^{(2)}\rangle &= \langle\Psi^{(2)}|\,\widehat{H}^{(2)}\,|\Psi^{(2)}\rangle + \langle\Psi^{(2)}|\,\widehat{H}^{(1)} - \widehat{H}^{(2)}\,|\Psi^{(2)}\rangle \\ &= E^{(2)} + \int d\mathbf{r}\left[V_{\text{ext}}^{(1)}(\mathbf{r}) - V_{\text{ext}}^{(2)}(\mathbf{r})\right] n_0(\mathbf{r}),\end{aligned} \tag{2.9}$$

and therefore

$$E^{(1)} < E^{(2)} + \int d\mathbf{r}\left[V_{\text{ext}}^{(1)}(\mathbf{r}) - V_{\text{ext}}^{(2)}(\mathbf{r})\right] n_0(\mathbf{r}). \tag{2.10}$$

If the above logic is repeated beginning with $\langle\Psi^{(2)}|\,\widehat{H}^{(2)}\,|\Psi^{(2)}\rangle < \langle\Psi^{(1)}|\,\widehat{H}^{(2)}\,|\Psi^{(1)}\rangle$, then it follows that

$$E^{(2)} < E^{(1)} + \int d\mathbf{r}\left[V_{\text{ext}}^{(2)}(\mathbf{r}) - V_{\text{ext}}^{(1)}(\mathbf{r})\right] n_0(\mathbf{r}). \tag{2.11}$$

Adding Eqs. 2.10 & 2.11 together leads to the inequality

$$E^{(1)} + E^{(2)} < E^{(1)} + E^{(2)}, \tag{2.12}$$

which is a contradiction. Therefore it follows that $n_0(\mathbf{r})$ is unique to a specific $V_{\text{ext}}(\mathbf{r})$, within a constant.

### 2.2.2 Proof of theorem II

In this proof the densities $n(\mathbf{r})$ are restricted to those that are ground state densities of some Hamiltonian with some external potential $V_{\text{ext}}(\mathbf{r})$, called a "V-representable" density. In DFT, all material properties are defined as functionals of $n(\mathbf{r})$, which includes the total energy. Eq. 2.7 suggests that the total energy functional is

$$\begin{aligned} E_{\text{HK}} &= T[n] + E_{\text{int}}[n] + \int d\mathbf{r} V_{\text{ext}}(\mathbf{r}) n(\mathbf{r}) + E_{II} \\ &\equiv F_{\text{HK}}[n] + \int d\mathbf{r} V_{\text{ext}}(\mathbf{r}) n(\mathbf{r}) + E_{II}, \end{aligned} \tag{2.13}$$

where

$$F_{\text{HK}}[n] = T[n] + E_{\text{int}}[n]. \tag{2.14}$$

Consider a system with ground state density $n^{(1)}(\mathbf{r})$, potential $V_{\text{ext}}(\mathbf{r})$, ground state wave function $\Psi^{(1)}$, and ground state energy $E^{(1)} = E_{\text{HK}}[n^{(1)}] = \langle \Psi^{(1)} | \widehat{H}^{(1)} | \Psi^{(1)} \rangle$. Now consider another density $n^{(2)}(\mathbf{r})$ associated with the wave function $\Psi^{(2)}$. It is clear that

$$E^{(1)} = \langle \Psi^{(1)} | \widehat{H}^{(1)} | \Psi^{(1)} \rangle < \langle \Psi^{(2)} | \widehat{H}^{(1)} | \Psi^{(2)} \rangle = E^{(2)}, \tag{2.15}$$

from which it follows that the correct ground state density has the lowest energy, and all other densities and associated wave functions correspond to higher energy states. What this means is if $F_{\mathrm{HK}}[n]$ in Eq. 2.14 were known exactly, then finding a global minimum for Eq. 2.13 with respect to $n(\mathbf{r})$ will produce the correct ground state density.

It is worth noting that an alternate and more general version of this proof that relaxes the "V-representable" constraint was formulated by M. Levy [79–81] and E. Lieb [82–84]. The reader is referred to the cited publications or Ref. [76] for more details.

## 2.3 The Kohn-Sham equations

The DFT method in the form discussed in the previous section, while appearing to simplify things by changing the problem from finding a complicated many-body wave function to finding the electron density that minimizes the energy, does not contain a "recipe" for solving for the electronic structure. Kohn and Sham [75] developed a solution to this problem through an ansatz: assume that the ground state density of the original interacting system is equal to that of some chosen non-interacting system. This replaces the many-body Hamiltonian with a single-particle Hamiltonian, otherwise known as the independent particle approximation. In the "non-interacting" independent particle approximation the electrons obey the Pauli exclusion principle but otherwise are assumed to be uncorrelated, so the effective potential in the single-particle Hamiltonian contains an approximate description of exchange and correlation effects, and in practice all the many-body terms are incorporated into an exchange-correlation functional of the density. This approach has proven to be very effective and is the underpinning of many modern first-principles electronic structure calculations.

The Kohn-Sham approach is based on two assumptions (quoting Ref. [76]):

1. "The exact ground state density can be represented by the ground state density of an auxiliary system of non-interacting particles. This is called "non-interacting V-representibility." Note that there are no rigorous proofs of this for real systems.

2. The auxiliary Hamiltonian is chosen to have the usual kinetic operator and an effective local potential $V^{\sigma}_{\text{eff}}(\mathbf{r})$ acting on an electron of spin $\sigma$ at point $\mathbf{r}$. The local form is not essential, but it is an extremely useful simplification."

Below the Kohn-Sham equations are derived. This time spin is included in the derivation.

An auxiliary independent-particle Hamiltonian is defined as

$$\widehat{H}^{\sigma}_{\text{aux}} = -\nabla^2 + V^{\sigma}(\mathbf{r}). \tag{2.16}$$

In the system there are $N = N^{\uparrow} + N^{\downarrow}$ independent electrons, and in the ground state, per the Pauli exclusion principle, one electron occupies the $N^{\sigma}$ orbitals $\Psi^{\sigma}_i(\mathbf{r})$ with the lowest eigenvalues $\varepsilon^{\sigma}_i$. The electron density of the auxiliary system is calculated as

$$n(\mathbf{r}) = \sum_{\sigma} n(\mathbf{r}, \sigma) = \sum_{\sigma} \sum_{i=1}^{N^{\sigma}} |\Psi^{\sigma}_i(\mathbf{r})|^2. \tag{2.17}$$

The kinetic energy operator $\widehat{T}_s$ for the auxiliary system is

$$\widehat{T}_s = -\sum_{\sigma} \sum_{i=1}^{N^{\sigma}} \langle \Psi^{\sigma}_i | \nabla^2 | \Psi^{\sigma}_i \rangle = \sum_{\sigma} \sum_{i=1}^{N^{\sigma}} \int d\mathbf{r} |\nabla \Psi^{\sigma}_i(\mathbf{r})|^2. \tag{2.18}$$

Finally, the classical Coulomb interaction energy of the electron density interacting with itself can be defined as

$$E_{\text{Hartree}}[n] = \int d\mathbf{r}d\mathbf{r}' \frac{n(\mathbf{r})n(\mathbf{r}')}{|\mathbf{r}-\mathbf{r}'|}, \tag{2.19}$$

which is the Hartree energy written as a functional of $n$.

The Kohn-Sham approach requires that the electron density for the auxiliary and real systems are identical. To connect the two systems, the energy functional in Eq. 2.13 is rewritten as

$$E_{\text{KS}}[n] = T_s[n] + \int d\mathbf{r}V_{\text{ext}}(\mathbf{r})n(\mathbf{r}) + E_{\text{Hartree}}[n] + E_{II} + E_{xc}[n], \tag{2.20}$$

where $V_{\text{ext}}(\mathbf{r})$ is the external potential due to the nuclei and any applied external fields. For Eqs. 2.20 & 2.13 to be equivalent, it follows that the exchange-correlation energy functional is

$$\begin{aligned} E_{xc}[n] &= F_{\text{HK}}[n] - (T_s[n] + E_{\text{Hartree}}[n]) \\ &= \langle \widehat{T} \rangle - T_s[n] + \langle \widehat{V}_{\text{int}} \rangle - E_{\text{Hartree}}[n]. \end{aligned} \tag{2.21}$$

This defines the exchange-correlation functional, which is the kinetic and interaction energies of the true system with the single-particle kinetic and Hartree energies of the auxiliary system subtracted away. Determining the exchange-correlation functional is the main problem of the Kohn-Sham approach, for if an exact expression for $E_{xc}[n]$ were known, then solving the Kohn-Sham problem would yield the exact ground state electron density and energy.

Next the variational approach will be used to derive the Kohn-Sham equations, where Eq. 2.20 will be varied with respect to the complex conjugate of the wave function, $\delta\Psi_i^{\sigma *}(\mathbf{r})$. The kinetic energy operator $T_s$ is a functional of the orbital wave functions, as seen in Eq. 2.18, while the rest of the terms are functionals of the density. Therefore, applying the variation and using the chain rule yields

$$\frac{\delta E_{\mathrm{KS}}}{\delta\Psi_i^{\sigma *}(\mathbf{r})} = \frac{\delta T_s}{\delta\Psi_i^{\sigma *}(\mathbf{r})} + \left[\frac{\delta E_{\mathrm{ext}}}{\delta n(\mathbf{r},\sigma)} + \frac{\delta E_{\mathrm{Hartree}}}{\delta n(\mathbf{r},\sigma)} + \frac{\delta E_{xc}}{\delta n(\mathbf{r},\sigma)}\right] \frac{\delta n(\mathbf{r},\sigma)}{\delta\Psi_i^{\sigma *}(\mathbf{r})} = 0, \tag{2.22}$$

subject to the orthonormalization constraint $\langle\Psi_i^{\sigma}|\Psi_j^{\sigma'}\rangle = \delta_{i,j}\delta_{\sigma,\sigma'}$. It follows from Eqs. 2.17 & 2.18 that

$$\frac{\delta T_s}{\delta\Psi_i^{\sigma *}(\mathbf{r})} = -\nabla^2\Psi_i^{\sigma}(\mathbf{r}), \tag{2.23}$$

$$\frac{\delta n(\mathbf{r},\sigma)}{\delta\Psi_i^{\sigma *}(\mathbf{r})} = \Psi_i^{\sigma}(\mathbf{r}). \tag{2.24}$$

It follows from combining Eqs. 2.22, 2.23, & 2.24 that

$$\frac{\delta E_{\mathrm{KS}}}{\delta\Psi_i^{\sigma *}(\mathbf{r})} = \left[-\nabla^2 + V_{\mathrm{KS}}^{\sigma}\right]\Psi_i^{\sigma}(\mathbf{r}) = 0, \tag{2.25}$$

where

$$\begin{aligned} V_{\mathrm{KS}}^{\sigma}(\mathbf{r}) &= \frac{\delta E_{\mathrm{ext}}}{\delta n(\mathbf{r},\sigma)} + \frac{\delta E_{\mathrm{Hartree}}}{\delta n(\mathbf{r},\sigma)} + \frac{\delta E_{xc}}{\delta n(\mathbf{r},\sigma)} \\ &= V_{\mathrm{ext}}(\mathbf{r}) + V_{\mathrm{Hartree}}(\mathbf{r}) + V_{xc}^{\sigma}(\mathbf{r}) \end{aligned} \tag{2.26}$$

is the Kohn-Sham potential. Defining the Kohn-Sham Hamiltonian

$$\widehat{H}_{\mathrm{KS}}^{\sigma} = -\nabla^2 + V_{\mathrm{KS}}^{\sigma}(\mathbf{r}), \tag{2.27}$$

and using the method of Lagrange multipliers to enforce the orthonormalization condition yields

$$\delta \left[ \langle \Psi | \, \widehat{H}_{\mathrm{KS}} \, | \Psi \rangle - E_{\mathrm{KS}} \left( \langle \Psi | \Psi \rangle - 1 \right) \right] = 0, \tag{2.28}$$

which is equivalent to the Rayleigh-Ritz principle [85, 86], which leads to a set of Schrödinger-like equations

$$\left( H^{\sigma}_{\mathrm{KS}} - \varepsilon^{\sigma}_{i} \right) \Psi^{\sigma}_{i}(\mathbf{r}) = 0. \tag{2.29}$$

Eqs. 2.26, 2.27, & 2.29 are the Kohn-Sham equations that form the basis of many modern first-principles methods to calculate the electronic structure.

## 2.4 Local spin density approximation (LSDA)

Solving the Kohn-Sham equations requires an explicit form of the exchange-correlation functional and an exact form is currently unknown. Remarkably, approximations to the exchange-correlation functional have been quite successful in describing the properties of many solids, and developing newer and better functionals is an active area of research [76, 87–99]. Kohn and Sham indicated in their original paper [75] that many solids are close to the limit of the homogeneous electron gas. Since the exchange-correlation term is separated from the kinetic energy and long-range Hartree terms, Kohn and Sham's observation suggests the exchange-correlation functional can reasonably approximated as a local functional of the density. This is the local spin density approximation (LSDA), which is parameter-free (i.e. the method is fully ab-initio) and is the conventional starting point when calculating the properties of a material system. The LSDA functional is used in the calculations presented in Chapters 5 and 6.

As discussed, the LSDA can be deduced through the observation that the electrons in many solids are close to the homogeneous electron gas limit where exchange and correlation effects are local in character. This suggests that the exchange-correlation functional can be approximated as an integral of the electron density and the exchange-correlation energy over all space, where the exchange-correlation energy at each point is assumed to be the same as in a homogeneous electron gas with the same density. Formally,

$$\begin{aligned} E_{xc}^{\mathrm{LDSA}}[n^{\uparrow}, n^{\downarrow}] &= \int d\mathbf{r} n(\mathbf{r}) \epsilon_{xc}^{\mathrm{hom}}(n^{\uparrow}(\mathbf{r}), n^{\downarrow}(\mathbf{r})) \\ &= \int d\mathbf{r} n(\mathbf{r}) \left[\epsilon_{x}^{\mathrm{hom}}(n^{\uparrow}(\mathbf{r}), n^{\downarrow}(\mathbf{r})) + \epsilon_{c}^{\mathrm{hom}}(n^{\uparrow}(\mathbf{r}), n^{\downarrow}(\mathbf{r}))\right] \end{aligned} \tag{2.30}$$

where in the second step the exchange and correlation terms are separated. The functional may equivalently be expressed in terms of the total density $n(\mathbf{r})$ and the spin polarization

$$\zeta(\mathbf{r}) = \frac{n^{\uparrow} - n^{\downarrow}}{n(\mathbf{r})}. \tag{2.31}$$

Note that the spin-independent local density approximation (LDA) may be recovered by setting $n^{\uparrow}(\mathbf{r}) = n^{\downarrow}(\mathbf{r}) = n(\mathbf{r})/2$. Defining the effective radius

$$r_s = \left(\frac{3}{4\pi n}\right)^{1/3} \tag{2.32}$$

the exchange-correlation potential is related to the exchange-correlation energy functional as shown in Eq. 2.26, and has a simple form in the LSDA:

$$V_{xc}^{\sigma}(\mathbf{r}, \zeta) = \epsilon_{xc}(r_s, \zeta) - \frac{r_s}{3} \frac{\partial}{\partial r_s} \epsilon_{xc}(r_s, \zeta) + [\mathrm{sgn}(\sigma) - \zeta] \frac{\partial}{\partial \zeta} \epsilon_{xc}(r_s, \zeta), \tag{2.33}$$

where sgn(↑) = 1 and sgn(↓) = −1.

U. von Barth and L. Hedin solved this equation for the exchange energy of the spin-polarized homogeneous electron gas [100]. The exchange energy is

$$\epsilon_x(r_s,\zeta) = \epsilon_x(r_s,0) + \left[\epsilon_x(r_s,1) - \epsilon(r_s,0)\right] f(\zeta) \tag{2.34}$$

where

$$f(\zeta) = \frac{1}{2}\frac{(1+\zeta)^{4/3} + (1-\zeta)^{4/3} - 2}{2^{1/3}-1}, \tag{2.35}$$

$$\epsilon_x(r_s,0) = -\frac{K}{r_s}, \tag{2.36}$$

$$\epsilon_x(r_s,1) = 2^{1/3}\epsilon_x(r_s,0), \tag{2.37}$$

$$K = \frac{3}{2\pi}\left(\frac{9\pi}{4}^{1/3}\right). \tag{2.38}$$

The correlation term was approximated to have the same form as the exchange term:

$$\epsilon_c(r_s,\zeta) = \epsilon_c(r_s,0) + \left[\epsilon_c(r_s,1) - \epsilon(r_s,0)\right] f(\zeta) \tag{2.39}$$

where

$$\epsilon_c(r_s,0) = -C^P G\left(\frac{r_s}{r^P}\right), \tag{2.40}$$

$$\epsilon_c(r_s,1) = -C^F G\left(\frac{r_s}{r^F}\right), \tag{2.41}$$

$$G(x) = \left(1+x^3\right)\ln\left(1+\frac{1}{x}\right) + \frac{x}{2} - x^2 - \frac{1}{3}. \tag{2.42}$$

The typical values used for parameters $C^P$, $C^F$, $r^P$, and $r^F$ were derived from many-body perturbation theory by Hedin and Lundqvist [101]. The values are, according to Moruzzi *et. al.* [102], $C^P = 0.045$, $C^F = C^P/2 = 0.0225$, $r^P = 21$, and $r^F =$

$2^{4/3}r^P = 52.92$. It is worth noting that there are alternate ways to parameterize the correlation term in LSDA, such as the parameterization by Perdew and Zunger [88] based on the quantum Monte Carlo calculations of the electron gas by Ceperley and Alder [103], as well as the parameterization suggested by Vosko, Wilkes, and Nusiar [104]. The reader is referred to Appendix B of Ref. [76] for details.

While the LSDA has been rather successful at describing the properties of materials, it has some known shortcomings that should be noted. Because the exchange term is based on a local approximation, there is a spurious self-interaction term that is small for a homogeneous electron gas but large in confined systems such as atoms [76]. The LSDA, in particular, is most accurate in systems where the electronic density varies slowly over the de Broglie wavelength of a characteristic electron. The LSDA tends to predict a systematic overbinding, such that the binding energies are too large, and the band gaps in semiconductors and insulators are typically underestimated by $\sim 40\%$ [105].

## 2.5 Noncollinear spin density

Density functional theory can be extended to noncollinear spin structures by defining a local spin density matrix

$$\rho^{\alpha\beta}(\mathbf{r}) = \sum_i f_i \Psi_i^{\alpha *}(\mathbf{r}) \Psi_i^{\beta}(\mathbf{r}). \tag{2.43}$$

This can also be thought of as associating the density at every point in space with a vector representing the spin direction. Introducing this requires that the Kohn-Sham

Hamiltonian in Ref. 2.27 be re-expressed as a 2 × 2 matrix

$$H_{KS}^{\alpha\beta}(\mathbf{r}) = -\nabla^2 + V_{KS}^{\alpha\beta}(\mathbf{r}). \tag{2.44}$$

While this looks like a rather complicated addition to the Kohn-Sham problem, in the LSDA it just requires finding the local axis of spin quantization.

## 2.6 Kohn-Sham in solids

The discussion of DFT so far has been general and, in principle, can be applied to any type of system. The goal is to solve the electronic structure of a solid. Solids, as long as they are not amorphous, have a periodic translational symmetry and it follows that the effective potential will reflect this periodicity:

$$V_{\text{eff}}(\mathbf{r} + \mathbf{T}) = V_{\text{eff}}(\mathbf{r}) \tag{2.45}$$

where **T** is a translation vector of the crystal lattice. This symmetry introduces the wave-vector **k** and leads to the well-known Bloch theorem, which states that wave function solutions for potentials of the type Eq. 2.45 have the general form

$$\Psi_{\mathbf{k}}(\mathbf{r}) = e^{i\mathbf{k}\cdot\mathbf{r}} u_{\mathbf{k}}(\mathbf{r}) \tag{2.46}$$

where $u_{\mathbf{k}}(\mathbf{r})$ is a periodic function of the crystal lattice. Because of the translational symmetry, the wave function need not be solved for all possible values of **k** and instead need only be evaluated within the first Brillouin zone (BZ). Additional symmetries in the lattice reduce the problem further, carving out a small irreducible wedge in reciprocal space that, upon application of the various symmetry transformations, produces the entire BZ.

To solve the Kohn-Sham equations, the wave functions need to be expanded into a complete basis set $\chi_{i\mathbf{k}}(\mathbf{r})$ that obeys the Bloch condition

$$\Psi_{n\mathbf{k}}(\mathbf{r}) = \sum_i c_{i,n\mathbf{k}} \chi_{i\mathbf{k}}(\mathbf{r}). \tag{2.47}$$

Note that $n$ is the band counting index, which follows from restricting $\mathbf{k}$ to the BZ. The following set of equations

$$0 = \sum_j \left[ \langle \chi_{i\mathbf{k}} | H | \chi_{j\mathbf{k}} \rangle - \epsilon_{n\mathbf{k}} \langle \chi_{i\mathbf{k}} | \chi_{j\mathbf{k}} \rangle \right] c_{j,n\mathbf{k}} \tag{2.48}$$

determine the coefficients when solved. The energies $\epsilon_{n\mathbf{k}}$ are determined by the familiar secular equation

$$0 = \det \left[ \langle \chi_{i\mathbf{k}} | H | \chi_{j\mathbf{k}} \rangle - \epsilon_{n\mathbf{k}} \langle \chi_{i\mathbf{k}} | \chi_{j\mathbf{k}} \rangle \right]. \tag{2.49}$$

The general procedure block-diagonalizes the Hamiltonian. Each "block" corresponds to a specific choice of $\mathbf{k}$[1] and the block size is the number of basis orbitals per atom, multiplied by the number of atoms per unit cell. For example, in an unpolarized system with one atom per unit cell and a basis set consisting of one $s$ orbital, three $p$ orbitals, and 5 $d$ orbitals, the block size is $9 \times 9$.

Once the basis set is chosen, an iterative procedure to achieve self-consistency is started to solve for the electronic structure. The steps are

1. Start with an initial guess of the electron density $n_{\text{in}}(\mathbf{r}) = n_0(\mathbf{r})$.

2. Calculate $V_{KS}$ using $n(\mathbf{r})$.

---

[1] While $\mathbf{k}$ itself a continuous vector, in numerical calculations, $\mathbf{k}$ is broken down into a finite grid of k-points.

3. Solve the Kohn-Sham equations.
4. Calculate the electronic density $n_{\text{out}}(\mathbf{r})$.
5. Does $n_{\text{in}}(\mathbf{r}) = n_{\text{out}}(\mathbf{r})$?
    a) If yes → Output total energy and other quantities.
    b) If no → Go back to step 2 and use $n_{\text{out}}(\mathbf{r})$ to generate a new $V_{KS}$ and repeat process.

## 2.7 Linear muffin-tin orbitals (LMTO)

As shown in the previous section, the wave function must be expanded into a specific basis set in order to solve the Kohn-Sham equations. One particular basis set is linear muffin-tin orbitals (LMTO), which forms a minimal basis leading to very efficient calculations with reasonable accuracy. The derivation of the LMTO basis set is involved and there are many details to be considered, and so only the important points will be described here. The reader is referred to Refs. [105, 106] for a complete discussion.

The name LMTO is based on the muffin-tin potential approximation, where the full effective potential is approximated as a collection of spherically symmetric potentials with a finite radius centered on the atomic sites at lattice positions $\mathbf{R}$ and a flat potential in the interstitial regions. The whimsical name “muffin tins” is clear if the potential is plotted for a two-dimensional sheet, with $x$ and $y$ corresponding to spatial directions and $z$ the magnitude of the potential. The resulting potential landscape resembles the type of dish used to bake muffins shown in Fig. 2.1. In the interstitial region the potential is constant and solutions to the Schrödinger equation

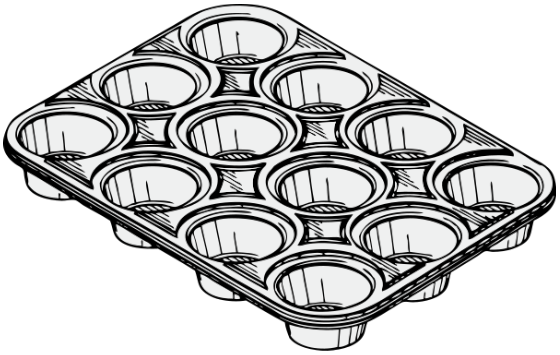

Figure 2.1: An illustration of a muffin tin. The muffin-tin potential approximation is so named because the resulting potential landscape resembles a muffin tin.

depend on evaluating structure constants which depend on the kinetic energy $E - V_0$ of the free electrons in the interstitial regions.

A further simplification to the problem is the atomic sphere approximation (ASA), which consists of using spherically symmetric, slightly overlapping, space-filling Wigner-Seitz spheres with Wigner-Seitz radius $s_{\mathbf{R}}$ centered on the atomic sites. Since this fills all space, the interstitial region is removed and the kinetic energy of the interstitial region can be neglected. This approximation works well for close-packed structures such as fcc and bcc lattices. For more open structures such as the diamond lattice, empty spheres can be introduced to fill the spatial gaps.

In the theoretical construction, the overlap of the spheres in the ASA is ignored and like in the regular muffin-tin potential the Kohn-Sham equation is defined with an interstitial region (note that, as per the approximation, the kinetic energy is ignored):

$$\left[-\nabla^2 + V(\mathbf{r}) - E\right]\Psi(\mathbf{r}) = 0; \qquad r \in A, \tag{2.50}$$

$$-\nabla^2\Psi(\mathbf{r}) = 0; \qquad r \in I, \tag{2.51}$$

$$V(\mathbf{r}) = V_{\mathbf{R}}(r_{\mathbf{R}}); \qquad r_{\mathbf{R}} \leq s_{\mathbf{R}}. \tag{2.52}$$

Eq. 2.51 is the Laplace equation, and its solutions are regular and irregular:

$$J_L(\mathbf{r}) = J_\ell(r) Y_L(\widehat{\mathbf{r}}); \qquad J_\ell(r) = \frac{1}{2(2\ell+1)} \left(\frac{r}{w}\right)^\ell, \tag{2.53}$$

$$K_L(\mathbf{r}) = K_\ell(r) Y_L(\widehat{\mathbf{r}}); \qquad K_\ell(r) = \left(\frac{w}{r}\right)^{\ell+1}, \tag{2.54}$$

where $w = (\frac{3}{4\pi}\Omega_0)^{1/3}$ is the average Wigner-Seitz radius of the lattice, $\Omega_0$ is the average volume per one atomic sphere, and $Y_L(\widehat{\mathbf{r}})$ is a spherical harmonic. The irregular solution $K_L$ may be expanded into a linear combination of regular solutions $J_L$ in regions centered about another atomic sphere:

$$K_L(\mathbf{r_R}) = -\sum_{L'} S_{\mathbf{R}L,\mathbf{R}'L'} J_{L'}(\mathbf{r}_{\mathbf{R}'}); \qquad \mathbf{R}' \neq \mathbf{R}. \tag{2.55}$$

The quantities $S_{\mathbf{R}L,\mathbf{R}'L'}$ are called the canonical structure constants and are given by

$$S_{\mathbf{R}'L',\mathbf{R}''L''} = \sum_L (-1)^{\ell''+1} \frac{8\pi\,(2\ell-1)!!C_{LL'L''}}{(2\ell'-1)!!\,(2\ell''-1)!!} K_L(\mathbf{R}''-\mathbf{R}'), \tag{2.56}$$

$$C_{LL'L''} = \int Y_L(\widehat{\mathbf{r}}) Y_{L'}(\widehat{\mathbf{r}}) Y_{L''}(\widehat{\mathbf{r}}) d\widehat{\mathbf{r}}. \tag{2.57}$$

The structure constants and the solutions to the Laplace equation will be important later when defining the explicit form of the LMTO basis set and a transformation of the Hamiltonian.

The Kohn-Sham equation may be solved using the variational approach, where the eigenvalue problem takes on a secular equation form similar to Eq. 2.49:

$$\det\left[EO_{ij} - H_{ij}\right] = 0, \tag{2.58}$$

$$\int_A \Psi^2(\mathbf{r}) d\mathbf{r} = 1, \tag{2.59}$$

where $O_{ij}$ and $H_{ij}$ are the overlap and Hamiltonian matrix elements, with the explicit forms

$$H_{ij} = \int_A \chi_i(\mathbf{r}) \left[-\nabla^2 + V(\mathbf{r})\right] d\mathbf{r} + \int_I \chi_i(\mathbf{r}) \left[-\nabla^2\right] d\mathbf{r}, \tag{2.60}$$

$$O_{ij} = \int_A \chi_i(\mathbf{r})\chi_j(\mathbf{r}) d\mathbf{r}. \tag{2.61}$$

In this formulation of the secular equation, the basis set functions $\chi_i$ must be energy independent. Regular muffin-tin orbitals (MTO), the energy-dependent basis set defined for muffin-tin potentials, are clearly not, but this can be fixed by making an expansion of the radial part of the wave function about a linearization energy. Choosing the linearization energy $E_{\nu,\mathbf{R}\ell}$, typically chosen to be the center of the occupied part of the $\mathbf{R}\ell$-projected valence DOS, the expansion is

$$\varphi_{\mathbf{R}\ell}(r, E) \approx \phi_{\mathbf{R}\ell}(r) + \dot{\phi}_{\mathbf{R}\ell}(r)(E - E_{\nu,\mathbf{R}\ell}) \tag{2.62}$$

where $\phi_{\mathbf{R}\ell}(r) = \varphi_{\mathbf{R}\ell}(r, E_{\nu,\mathbf{R}\ell})$ and $\dot{\phi}$ is the energy derivative.

To derive the LMTO basis set, we first begin with the irregular solution to the Laplace equation $K_L(\mathbf{r_R})$ centered at site $\mathbf{R}$ extended over all space. Using Eq. 2.55, the irregular solution can be rewritten in terms of regular solutions inside the other atomic spheres. Next, inside the spheres, we replace the radial parts of the regular and irregular solutions, $K_\ell$ and $J_\ell$, with linear combinations of $\phi_{\mathbf{R}\ell}(r)$ and $\dot{\phi}_{\mathbf{R}\ell}(r)$ and require that there is a smooth matching of the radial functions across the atomic sphere boundaries. This defines the energy-independent LMTO basis set

$$\begin{aligned}
\chi_{\mathbf{R}L}(\mathbf{r}) &= -\{K,\dot{\phi}\}_{\mathbf{R}\ell}\phi_{\mathbf{R}L}(\mathbf{r}_{\mathbf{R}}) + \{K,\phi\}_{\mathbf{R}\ell}\dot{\phi}_{\mathbf{R}L}(\mathbf{r}_{\mathbf{R}}) && r_{\mathbf{R}} < s_{\mathbf{R}} \\
&= \sum_{L'} S_{\mathbf{R}L,\mathbf{R}'L'}\left[\{J,\dot{\phi}\}_{\mathbf{R}'\ell'}\phi_{\mathbf{R}'L'}(\mathbf{r}_{\mathbf{R}'}) - \{J,\phi\}_{\mathbf{R}'\ell'}\dot{\phi}_{\mathbf{R}'L'}(\mathbf{r}_{\mathbf{R}'})\right] && r_{\mathbf{R}'} \leq s_{\mathbf{R}'} \\
&= K_L(\mathbf{r}_{\mathbf{R}}) && \mathbf{r} \in I
\end{aligned} \tag{2.63}$$

where

$$\{K,\phi\}_{\mathbf{R}\ell} = \{K_\ell(r),\phi_{\mathbf{R}\ell}(r)\}|_{r=s_{\mathbf{R}}} \tag{2.64}$$

and terms in curly brackets are Wronskians, defined as

$$\{f_1(r),f_2(r)\} = r^2\left[f_1(r)f_2'(r) - f_1'(r)f_2(r)\right]. \tag{2.65}$$

A convenient transformation orthogonalizes the LMTO basis set and keeps eigenvalues accurate to second order in $(E - E_\nu)$. Applying the transformation simplifies the secular equation

$$\det\left[E\delta_{\mathbf{R}L,\mathbf{R}'L'} - H^{\text{orth}}_{\mathbf{R}L,\mathbf{R}',L'}\right] = 0 \tag{2.66}$$

where the overlap matrix is replaced with the Kronecker delta. The orthogonal Hamiltonian can be parameterized using the following potential parameters:

$$C_{\mathbf{R}\ell} = E_{\nu,\mathbf{R}L} - \frac{\{K,\phi\}_{\mathbf{R}\ell}}{\{K,\dot{\phi}\}_{\mathbf{R}\ell}}, \tag{2.67}$$

$$\Delta_{\mathbf{R}\ell} = \frac{w}{2}\frac{1}{\{K,\dot{\phi}\}^2_{\mathbf{R}\ell}}, \tag{2.68}$$

$$\gamma_{\mathbf{R}\ell} = \frac{\{J,\dot{\phi}\}_{\mathbf{R}\ell}}{\{K,\dot{\phi}\}_{\mathbf{R}\ell}}, \tag{2.69}$$

leading to the simple form in matrix notation

$$H^{\text{orth}} = C + \sqrt{\Delta} S \left(1 - \gamma S\right)^{-1} \sqrt{\Delta}. \tag{2.70}$$

The Hamiltonian in Eq. 2.70 is in the canonical representation with the structure constants defined in Eq. 2.56. The canonical structure constants are long-ranged, which is inconvenient for calculation. The structure constants can be re-expressed in a screened form and a proper choice of screening constants transforms them into short-ranged quantities where typically only next-nearest neighbor terms in the sum need to be included. The transformation should also be applied to $H^{\text{orth}}$. This is called the tight-binding LMTO representation (the full acronym is TB-LMTO-ASA), which is extremely convenient to use. The first-principles calculations in Chapters 5 & 6 use TB-LMTO-ASA.

## Chapter 3

# Thermodynamics of itinerant magnets in a classical spin fluctuation model

## 3.1 Introduction

The thermodynamics of magnetic materials is often described using the Heisenberg model in which the spins are attached to lattice sites. Real magnets are much more complicated, because the magnetization is due to band electrons whose degree of localization varies between different materials. This so-called *itinerancy* manifests itself in the fluctuation of the magnitudes of the local moments, which may be defined in a muffin tin sphere or using a projection in an appropriate basis. Thus, the degree of itinerancy may be characterized by the relative importance of longitudinal and transverse (rotational) fluctuations of the local moments [107]. In the localized (Heisenberg) limit the longitudinal spin fluctuations (LSF) have a large energy scale and are suppressed. This limit is approached in some magnetic insulators. Metals, on the other hand, are often quite far from this limit, because the exchange splitting and the bandwidth are typically of the same order. Experimentally, itinerancy is most clearly revealed in the paramagnetic susceptibility by the deviation of the effective moment found from the Curie-Weiss constant from the true local moment, as well as by the deviations from the Curie-Weiss law.

A large amount of work has been devoted to the thermodynamics of itinerant magnets using phenomenological Ginzburg-Landau models for weak ferromagnets [107–109] or the Hubbard model and the functional integral methods [107, 110–112]. These studies have clarified the role of LSF in thermodynamics and explained the observed behavior of the paramagnetic susceptibility. However, these methods are unsuitable for quantitative studies of realistic materials. Ginzburg-Landau expansions, as is well known, correctly describe only the contribution of long-wave fluctuations and must always be rigged with a wavevector cut-off. Such models are useful in the studies of critical phenomena, but they are irrelevant to the determination of the critical temperature itself, which is determined by *short-range* fluctuations [113]. An unsatisfactory signature of Ginzburg-Landau models is the absence of any information on the short-wave components of the exchange interaction in the resulting expressions for the Curie temperature [108, 109, 114]. In our opinion, the neglect of short-wave fluctuations in these models makes their predictions for magnetic short-range order (MSRO) also unreliable. The functional integral method, on the other hand, suffers from the necessity to make severe and ambiguous approximations [115].

Magnetic thermodynamics has also been studied using density functional theory (DFT) by treating spin fluctuations within the adiabatic approximation [116] assuming that the relevant fluctuations are well represented by constrained [117] noncollinear ground states. The most widespread approach is the disordered local moment (DLM) approximation [116, 118] which relies on the single-site approximation and is designed to approximate the DFT ground state of a system with random directions of the local moments. The LSF have been neglected in all implementations of this approach so far, restricting its application to magnets which are close to the localized limit. In particular, the DLM method neglecting LSF fails for (strongly itinerant) nickel where it finds vanishing local moment in the paramagnetic phase [119].

Other authors studied *itinerant* thermodynamics by mapping the results of first-principles energies for various spin configurations (including both transverse and longitudinal fluctuations) to a classical Hamiltonian in which variable local moments play the role of dynamical variables, and then exploring the thermodynamics of this Hamiltonian using either the variational principle in reciprocal space [120] or Monte Carlo (MC) simulations in real space [121–123]. These calculations clearly show that LSF, as expected, are very important in nickel. Moreover, they revealed only weak magnetic short-range order (MSRO) above the Curie temperature $T_c$ for both Fe and Ni, which is similar to the Heisenberg model. These results are consistent with the fact that in any lattice model with no frustration all correlation corrections to the mean-field approximation (outside of the critical region) should be small in the parameter $1/z$, where $z$ is the number of neighbors within the interaction range [98]. On the other hand, very strong MSRO above $T_c$ was found [124] in Ni using the *ab initio* spin dynamics method, which, similar to DLM, is based on the adiabatic approximation and neglects LSF.

Classical models with variable local moments seem to capture the important qualitative features of the thermodynamics of itinerant magnets which are similar to the predictions of the functional integral method. However, these models have been built and studied only for a few particular materials, and a general study of their thermodynamic properties has not been undertaken. Such a study is useful as a step to more refined models with the advantage that numerically exact results for a classical model are easily accessible through Monte Carlo simulations. Therefore, in this chapter we explore the thermodynamics of a classical spin fluctuation model as a function of the degree of itinerancy using MC simulations and simple analytic approximations. We emphasize that here we are not concerned with the “mapping” procedure (which can be quite challenging) but rather focus on the other separate part of the program, i.e. on the determination of thermodynamics once the Hamiltonian has been defined. We therefore restrict ourselves to the simplest possible realization of this model which includes only *one* free parameter characterizing the degree of itinerancy.

## 3.2 Model

Our model is a lattice version of the phenomenological model of Murata and Doniach [108] written with a vector order parameter [107]:

$$\begin{aligned} H &= \frac{1}{2}\sum_{\mathbf{q}} \chi^{-1}(\mathbf{q})\mathbf{m}_{\mathbf{q}}\mathbf{m}_{-\mathbf{q}} + \frac{B}{4}\sum_i m_i^4 \\ &= \sum_i \left[\frac{1}{2}\left(\chi_{00}^{-1} - I\right) m_i^2 + \frac{B}{4} m_i^4\right] - \frac{1}{2}\sum_{i\neq j} J_{ij}\mathbf{m}_i\mathbf{m}_j. \end{aligned} \tag{3.1}$$

Here $\mathbf{m}_i$ denotes the magnetic moment at site $i$ whose length is unrestricted, and $I$ the Stoner exchange-correlation parameter. We have separately written the local $\chi_{00}^{-1} = \partial B_i/\partial m_i$ and nonlocal $J_{ij} = -\chi_{ij}^{-1}$ parts of the unenhanced inverse susceptibility. This model involves a number of simplifying assumptions: (1) It is classical in the sense that $\mathbf{m}_i$ are dynamical variables and not operators. (2) Both local and nonlocal parts of the inverse susceptibility are considered to be independent of the magnetic state and *isotropic*. In general, $\chi_{ij}^{-1}$ is a Cartesian tensor which depends on the magnetic state and reduces to a scalar only in the paramagnetic state. (3) Nonlinear effects are included only through a local fourth-order term, similar to the Murata-Doniach model.

Eq. 3.1 is somewhat similar to that used to represent the unified spin fluctuation

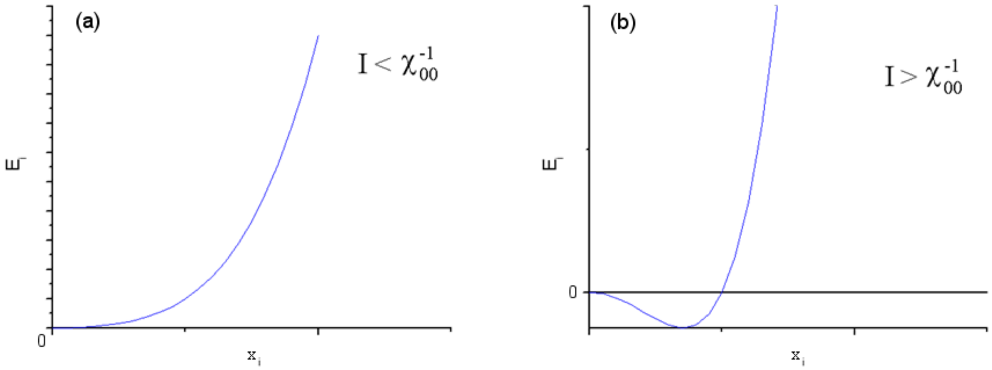

Figure 3.1: A schematic in arbitrary units of the function $E(x)$ in Eq. 3.2 for varying $x$. (a) When $I < \chi_{00}^{-1}$ and the Anderson criterion is not satisfied. (b) When $I > \chi_{00}^{-1}$ and the Anderson criterion is satisfied.

theory [110] classically (see Ref. [107], Ch. 7, and also Ref. [125]), with an important difference: the energy of LSFs is included as a function of local dynamical variables $\mathbf{m}_i$, rather than that of one global parameter $\langle m_i^2 \rangle$. This difference is similar to that between the Heisenberg model and the spherical approximation to it.

In the ground state all local moments are parallel and we recover the Stoner model which is ferromagnetic if $IN(E_F) > 1$, where $N(E_F) = \chi(0)$ is the density of states at the Fermi level in the nonmagnetic state. This Stoner criterion can also be written as $(I + J_0) > \chi_{00}^{-1}$ where $J_0 = \sum_j J_{ij}$. On the other hand, in the paramagnetic or non-magnetic matrix, local moments exist in the Anderson sense only if $I > \chi_{00}^{-1}$ which is stricter than the Stoner criterion. We will call this the Anderson criterion.[1] An illustration of the Anderson criterion is in Fig. 3.1, showing the energy profile absent the Heisenberg-like term in Eq. 3.1.

Introducing reduced local moments $\mathbf{x}_i = \mathbf{m}_i / m_0$, where $m_0$ is the value of all $m_i$

---

[1] Note that $\chi_{00}^{-1} \neq 1/\chi_{00}$.

at $T = 0$, the Hamiltonian in Eq. 3.1 can be conveniently parameterized:

$$H' \equiv \frac{H}{J_0 m_0^2} = \sum_i E(x_i) - \frac{1}{2}\sum_{i \neq j} \frac{J_{ij}}{J_0} \mathbf{x}_i \cdot \mathbf{x}_j, \tag{3.2}$$

where $E(x) = [ax^2/2 + bx^4/4]/J_0$ with $a = \chi_{00}^{-1} - I$ and $b = Bm_0^2 = J_0 - a$. For the nearest neighbor model with coordination number $z$ we have $J_{nn}/J_0 = 1/z$, and for the given lattice $H'$ contains only one parameter, which we define as $\alpha = \arctan b/a$. Note that $b > 0$ is equivalent to the Stoner criterion, and $a < 0$ is equivalent to the Anderson criterion.[2] Applying the definition of $\alpha$ to Eq. 3.2, $E(x)$ becomes

$$E(x_i) = \left(\frac{1}{1 + \tan\alpha}\right)\left(\frac{x_i^2}{2} + \frac{\tan\alpha}{4} x_i^4\right). \tag{3.3}$$

The effect of the parameter is isolated to the intra-site energy terms only.

To understand the meaning of the parameter $\alpha$, consider the ground state of Hamiltonian $H$ with a single-site excitation, i.e. the state with $\mathbf{m}_i = \mathbf{m}_0$ for all $i$ except $i = c$. The energy of this state has a minimum at $\mathbf{m}_c = \mathbf{m}_0$ and its curvature with respect to the longitudinal fluctuation of $\mathbf{m}_c$ is $K_\parallel = J_0 + 2b$, while the curvature with respect to transverse fluctuations is $K_\perp = J_0$. Their ratio $K_\parallel/K_\perp = 1 + (2b/J_0)$ characterizes the relative importance of longitudinal and transverse fluctuations. If $b \gg J_0$, the fluctuations are mainly transverse, and we have the localized (Heisenberg) limit for which $a \approx -b$ and $\alpha \approx 3\pi/4$. If $b \ll J_0$, the transverse and longitudinal spin fluctuations are equally important; this limit corresponds to $\alpha = 0$. The Anderson criterion is equivalent to $\alpha > \pi/2$. Thus, the parameter $\alpha$ characterizes the degree of itinerancy and is similar to those appearing in other theories [107, 110]. Note that we always have $K_\parallel/K_\perp > 1$, even though the *macroscopic* longitudinal stiffness is

---

[2] We are grateful to V. P. Antropov for his suggestion that the Anderson criterion can be used to quantify the degree of itinerancy.

proportional to $b$ and tends to zero at $\alpha \to 0$.

Evaluation of the thermodynamic properties involves taking a trace over the quantum states, known as the partition function

$$Z = \sum_n e^{-\frac{E_n}{k_B T}}. \tag{3.4}$$

For a classical system, the trace may be replaced with a functional integral over the classical degrees of freedom. To our knowledge, in all classical models reported so far and based on *ab initio* calculations, the uniform measure in the space of $\mathbf{m}_i$ was used [120–123]. However, our dynamical variables are not canonical, and therefore the PSM is not known. In the case when LSF are important, the PSM has to be supplied along with the Hamiltonian as an additional phenomenological ingredient. Strictly speaking, it is not possible to disentangle the measure from quantum statistics; for example, in the atomic limit only integer moments with atomic multiplet degeneracies should be present. Ambiguity of PSM is intrinsic to all microscopic classical spin fluctuation models including the classical version of the "unified theory" of Moriya and Takahashi (Ref. [107], Sec. 7) and its extensions [125], as well as the functional integral approach combined with the static approximation which destroys the correct quantum operator properties. In the latter case, the Hubbard-Stratonovich transformation can be applied with the interaction term written in different ways, which produce different results after the static approximation is made [111, 115]. Two particular choices discussed by Hubbard [111] result in different measures in the space of fluctuating fields $\mathbf{v}_i$: uniform in one case, and involving the weighting factor $\prod_i v_i^{-2}$ in another. To explore the influence of PSM on thermodynamics, we will consider these two measures in the space of the local moments $\mathbf{m}_i$.

## 3.3 Thermodynamic properties: Monte Carlo and mean-field results

Monte Carlo simulations for the model in Eq. 3.2 were performed using the Metropolis algorithm for bcc and fcc lattices with nearest neighbor exchange. At each step the new random direction and magnitude of the moment on one site was tried, and sampling of the moment magnitude was performed according to the chosen PSM. We used supercells with up to 3456 or 6912 sites for bcc or fcc lattices ($12 \times 12 \times 12$ unit cells with periodic boundary conditions). The reduced Curie temperature $t_c = T_c/(J_0 m_0^2)$ was found using the fourth-order cumulant method [126], and the paramagnetic susceptibility was calculated using the fluctuation-dissipation theorem.

The mean-field approximation (MFA) is applied in the same manner as in Sec. 1.4.2. The MFA to the Hamiltonian in Eq. 3.2 is

$$H'_{\mathrm{MFA}} = \sum_i \left[ E(x_i) + \frac{\langle x_z \rangle_i^2}{2} - h_{W,i} x_i \cos\theta_i \right], \tag{3.5}$$

where $h_W = \langle x_z \rangle$ is the reduced Weiss field. The single-site partition sum is easily found:

$$\begin{aligned} Z_1 &= \int_0^{2\pi} d\phi \int_0^{\infty} dx \int_{-1}^{1} g(x) x^2 e^{-\beta[E(x)+\langle x_z\rangle^2/2 - h_W x \cos\theta]} d\cos\theta \\ &= \frac{4\pi}{\beta h_W} e^{-\beta\langle x_z\rangle^2/2} \int_0^{\infty} g(x) x \sinh(\beta h_W x) e^{-\beta E(x)} dx \end{aligned} \tag{3.6}$$

where $t = \frac{k_B T}{J_0 m_0^2}$ is the reduced temperature and $\beta = 1/t$ is its inverse, and $g(x)$ is the weighting factor, which is either 1 or $x^{-2}$ for the two chosen PSM's. With the partition sum calculated, the reduced single-site free energy $f' \equiv \frac{f}{J_0 m_0^2}$ is found to be

$$\begin{aligned} f' &= -\frac{1}{\beta}\ln\left(Z_1\right) \\ &= \frac{\langle x_z\rangle^2}{2} - \frac{1}{\beta}\ln\left[\left(\frac{4\pi}{\beta h_W}\right)\int_0^\infty g(x)x\sinh(\beta h_W x)e^{-\beta E(x)}dx\right]. \end{aligned} \tag{3.7}$$

The magnetization is found by minimizing the free energy with respect to $\langle x_z\rangle$, which leads to the self-consistent equation

$$\langle x_z\rangle = -\frac{1}{\beta h_W} + \frac{\int_0^\infty g(x)x^2\cosh(\beta h_W x)e^{-\beta E(x)}dx}{\int_0^\infty g(x)x\sinh(\beta h_W x)e^{-\beta E(x)}dx}. \tag{3.8}$$

The average square of the local moment is

$$\begin{aligned} \langle x^2\rangle &= \frac{1}{Z_1}\int x^2 e^{-\beta H'_{\mathrm{MFA},i}(x)}d\mathbf{x} \\ &= \frac{\int_0^\infty g(x)x^3\sinh(\beta h_W x)e^{-\beta E(x)}dx}{\int_0^\infty g(x)x\sinh(\beta h_W x)e^{-\beta E(x)}dx}. \end{aligned} \tag{3.9}$$

To obtain the expression for the magnetic susceptibility above $t_c$, we need to consider the response of the system to an external magnetic field. The result of adding the term $-\sum_i \mathbf{x}_i\cdot\mathbf{h}$ to the Hamiltonian in Eq. 3.2, where $h = \frac{Hg\mu_B}{J_0 m_0}$ is the reduced external field, is to replace $h_W$ with $h_{\text{eff}} \equiv h_W + h$ in Eqs. 3.5-3.9. The hyperbolic functions in the self-consistent equation Eq. 3.8 then are expanded to third order in $h_{\text{eff}}$, which after some algebra leads to the expression

$$\langle x_z\rangle\left(1 + \frac{\beta^2 h_{\text{eff}}^2}{6}\left.\langle x^2\rangle\right|_{h_{\text{eff}}\to 0}\right) = \frac{\beta h_{\text{eff}}}{3}\left.\langle x^2\rangle\right|_{h_{\text{eff}}\to 0} \tag{3.10}$$

where $\langle x^2\rangle|_{h_{\text{eff}}\to 0}$ is Eq. 3.9 for vanishing Weiss and external fields. The magnetic susceptibility, defined as $\chi = \frac{d\langle x_z\rangle}{dh}$, is found by taking the derivative of Eq. 3.10 with respect to $h$ and then taking the limit of $h \to 0$ and $h_W = \langle x_z \rangle \to 0$, obtaining

$$\chi_{\text{MFA}} = \frac{\frac{1}{3}\langle x^2 \rangle}{t - \frac{1}{3}\langle x^2 \rangle} \tag{3.11}$$

where in this context $\langle x^2 \rangle \equiv \langle x^2 \rangle |_{h_{\text{eff}} \to 0}$.

To calculate the above thermodynamic quantities in the mean-field approximation, the self-consistent magnetization needs to be determined for a specified $\alpha$, temperature $t$, and PSM $g(x)$. This requires a looping algorithm to calculate $\langle x_z \rangle$ as a function of $t$. For our calculations we used Mathematica to calculate the MFA solutions in Figs. 3.2 & 3.6. The input code used in the Mathematica notebooks to perform these calculations can be found in Appendix 3.A.

Fig. 3.2 shows the temperature dependence of magnetization, the average square of the local moment and the paramagnetic susceptibility using the reduced variables according to Eq. 3.2. Results are shown for two values of $\alpha$: $0.48\pi$ and $0.69\pi$. In both cases the agreement between MC and the MFA results is very good for all properties (the MFA overestimates $T_c$ by 20% or less). The results strongly depend on PSM, especially in the more itinerant case $\alpha = 0.48\pi$. In particular, for the uniform PSM a second-order phase transition occurs for both values of $\alpha$, but for the PSM with $g(x) = x^{-2}$ the phase transition is of first order for $\alpha = 0.48\pi$, and $T_c$ is nearly 2.8 times smaller compared to that for $g(x) = 1$.

As seen in Fig. 3.2, below $T_c$ the average $\langle x^2 \rangle$ declines with temperature due to the decrease of the Weiss field, which causes the maximum of the distribution function to shift to smaller moments. This is in agreement with earlier results [107, 111, 112, 120, 121, 123]. The behavior of $\langle x^2 \rangle$ may be understood by considering the distribution function, several of which are plotted in Fig. 3.3. The width of the distribution function increases with temperature, which counteracts the decrease of

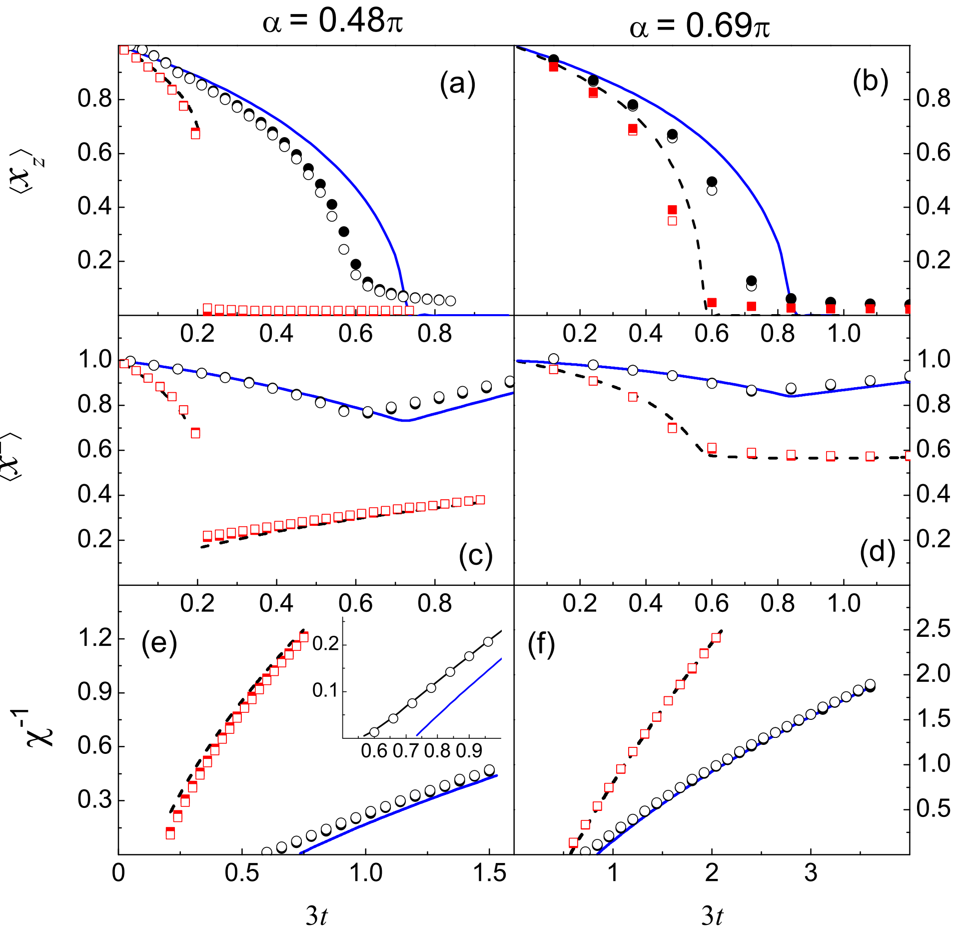

Figure 3.2: (a-b) Reduced magnetization $\langle x_z \rangle$, (c-d) mean squared local moment $\langle x^2 \rangle$, and (e-f) inverse paramagnetic susceptibility $\chi^{-1}$ as a function of the reduced temperature $t = T/(J_0 m_0^2)$. The MFA results are shown by solid blue lines for $g(x) = 1$ and by dashed black lines for $g(x) = x^{-2}$. MC results are displayed by black circles for $g(x) = 1$ and by red squares for $g(x) = x^{-2}$ (in both cases the symbols are filled for fcc and empty for bcc lattice). The inset in panel (e) highlights the region close to $t_c$ for the bcc lattice with $g(x) = 1$ and also shows the results of the generalized Onsager method (black line connecting the MC points).

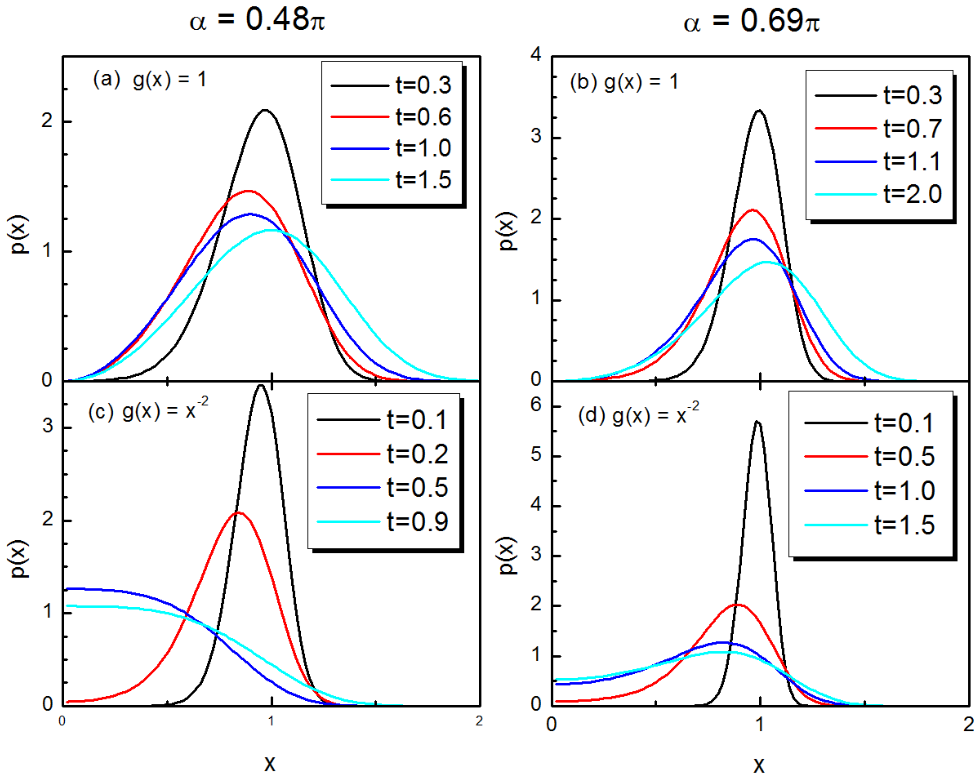

Figure 3.3: The distribution function $p(x)$ calculated at several reduced temperatures for two different values of $\alpha$ and two different PSMs.

the local moment. The PSM with $g(x) = x^{-2}$ puts less weight on the states with large moments, and hence $\langle x^2 \rangle$ drops much faster compared to the uniform PSM. If the Anderson criterion is not satisfied ($\alpha < \pi/2$) then the most probable moment in the paramagnetic state is zero, as seen in Fig. 3.3(c). In this case, $\langle x^2 \rangle$ increases with temperature above $T_c$ as seen in Fig. 3.2(c). On the other hand, if the Anderson criterion is satisfied, the local moment may slightly decrease in a range of temperatures above $T_c$, as seen for $g(x) = x^{-2}$ in Fig. 3.2(d). Looking at the distribution function in Fig. 3.3(d), this is the result of finite weight appearing above $t_c$ for zero local moment, while the most probable moment remains finite.

The magnetic susceptibility above $T_c$ is shown in Figs. 3.2(e) & 3.2(f). In MC

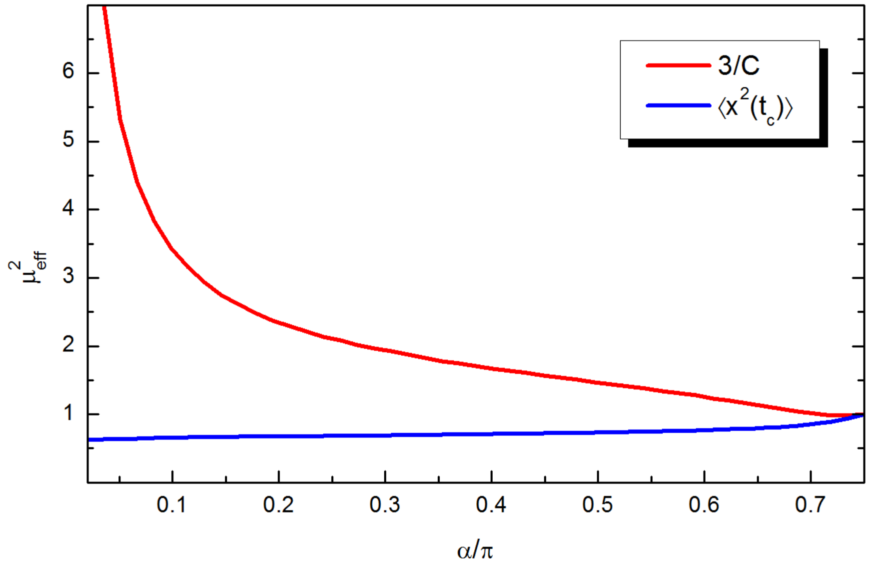

Figure 3.4: The change of the effective moment $\mu_{\text{eff}}^2$ as the itinerancy parameter $\alpha$ is varied. The blue line shows the average square of the moment from Eq. 3.9 evaluated at $t_c$ and the red line shows the effective moment found from the Curie constant from Eq. 3.12 for $g(x) = 1$ in the MFA.

simulations it is calculated using fluctuation-dissipation theorem, while for the MFA Eq. 3.11 is used. Excellent agreement between the MFA and MC is observed except for the small error in $T_c$. Eq. 3.11 looks similar to the Curie-Weiss expression in the Heisenberg model, but here $\langle x^2\rangle$ depends on temperature, which leads to a renormalization of the CW constant and deviations from the CW law. The CW constant $C = d\chi^{-1}/dt$ (for a second-order phase transition) is now given by

$$C = \frac{3}{\langle x^2(t_c)\rangle}\left[1 - \left.\frac{d\log\langle x^2\rangle}{d\log t}\right|_{t_c}\right]. \tag{3.12}$$

Thus, in addition to the usual Heisenberg term the Curie constant has a contribution due to the temperature dependence of $\langle x^2\rangle$ (second term in square brackets in Eq. 3.12). As a result, the effective moment squared $\mu_{\text{eff}}^2 = 3/C$ deviates from $\langle x^2\rangle$ as shown in Fig. 3.4. In the local limit $\mu_{\text{eff}}$ naturally tends to 1. However, as $\alpha$ is

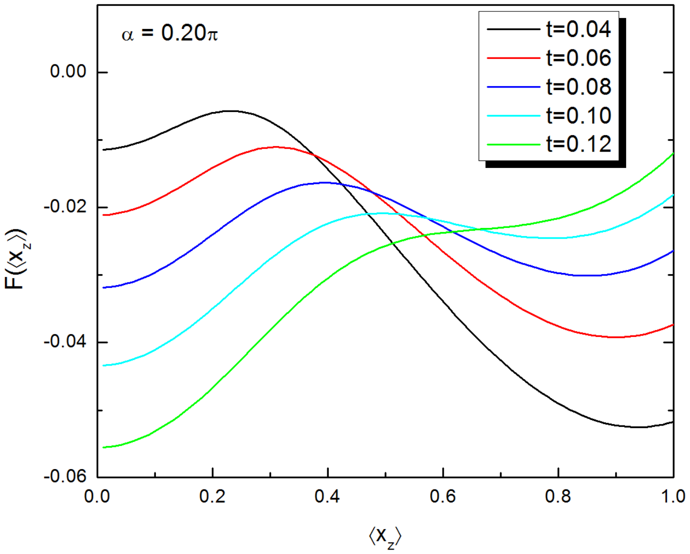

Figure 3.5: The free energy in Eq. 3.7 calculated for $\alpha = 0.20\pi$ using several reduced temperatures.

decreased towards zero, the ratio $\mu_{\rm eff}^2/\langle x^2(t_c)\rangle$ increases and eventually becomes much larger than 1. Similar behavior is found in functional integral theories [107]. As discussed above, $\langle x^2\rangle$ usually increases with temperature above $T_c$, which, according to Eq. 3.12, reduces $C$ and increases $\mu_{\rm eff}^2$. Moreover, for the uniform PSM $\langle x^2\rangle$ increases faster with temperature compared to PSM with $g(x) = x^{-2}$, and hence the CW constant is much smaller in this case (see Fig. 3.2(f), and also Fig. 3.2(e) where the transition is however of first order).

In Fig. 3.6 $t_c$ and the magnetic short range order parameter are plotted as a function of the itinerancy parameter $\alpha$. From Eq. 3.11 it follows that the MFA value of $t_c$ for the second-order phase transision is found by solving the equation $3t_c = \langle x^2(t_c)\rangle$, where $\langle x^2(t)\rangle$ is fully determined by $E(x)$ in Eq. 3.2. This is an easy way to estimate $T_c$ for an itinerant system using first-principles data for $E(x)$, $J_0 m_0^2$, and the assumed PSM. However, for PSM with $g(x) = x^{-2}$ the transition is of first order except for a small region close to the local moment limit (in the MFA the tricritical point where the order of the phase transition changes is at $\alpha_{tr} = 0.632\pi$). Therefore, in general one must consider the minima of the free energy as a function of the magnetization, which can also be easily done in the MFA as shown in Fig. 3.5. In particular, Fig. 3.5 shows that for small $\alpha$ there are metastable values of $\langle x_z \rangle$, which can lead to incorrect predictions of $t_c$ if the rest of the free energy profile is ignored. Note that the order of the phase transition depends on the details of the model and can change if, for example, the dependence of the exchange parameter on the magnetization is taken into account. In particular, the phase transition for the model of Ni is of first order in Ref. [120] (as seen from the abrupt drop of $M(T)$ and $M_s$ at $T_c$ in their Fig. 2) and in Ref. [123] (as seen from the abrupt drop of $\overline{m}$ in their Fig. 6), even though the uniform PSM was used in both of these models.

From Fig. 3.6 we see that when the transition is of second order, the MFA overestimates $T_c$ by about 20%, which is typical for the Heisenberg model. When the transition is of first order, the MFA gives an almost exact $T_c$. It is important that even for the second-order transition the overestimation of $T_c$ in the MFA does not depend on the degree of itinerancy. This is consistent with the fact that the degree of MSRO, which is shown in Fig. 3.6(b) for $T = 1.1T_c$, is quite small and stays essentially constant in the whole range of $\alpha$. Thus, in our model itinerancy does not lead to strong short-range order. This result agrees with Refs. [121, 123] where weak short-range order was found for the models of Fe and Ni. Note that if the exchange interaction extends to more than one shell of neighbors and stays mainly ferromagnetic, the MFA validity criterion is satisfied even better, and the MSRO parameter should further decrease. Similar to the Heisenberg model, strong MSRO may only be expected in low-coordinated lattices or in the presence of frustration when for some pairs $J_{ij}/kT_c$ is not small.

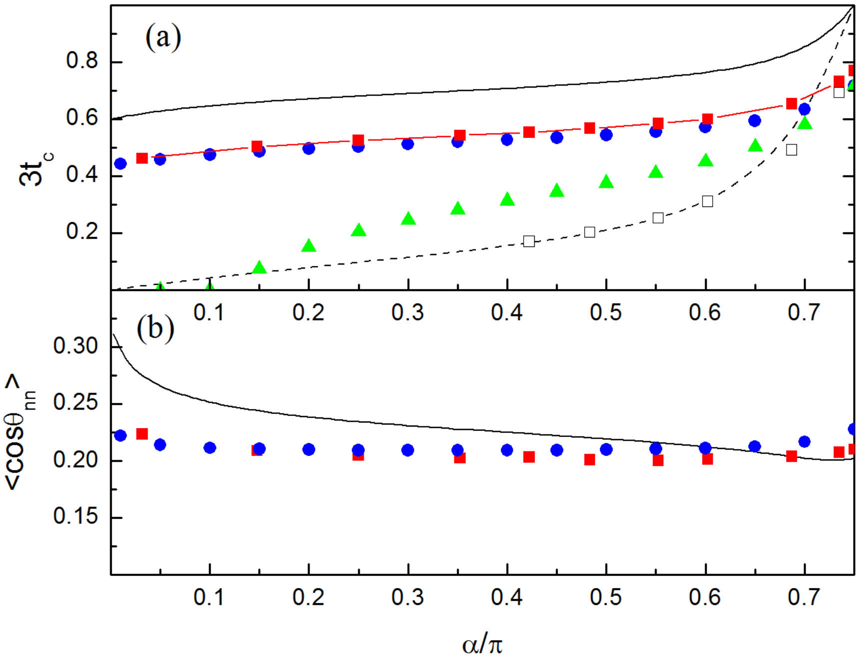

Figure 3.6: (a) Reduced Curie temperature $t_c$ and (b) MSRO parameter $\langle \cos\theta_{nn} \rangle$ at $T = 1.1T_c$ as a function of the itinerancy parameter $\alpha$ for the bcc lattice. Solid black line, red squares, and blue circles show the results of the MFA, MC, and the generalized Onsager method for $g(x) = 1$, respectively. Dashed black line and empty black squares depict the MFA and MC results for $g(x) = x^{-2}$. Green triangles represent the incomplete Onsager reaction field correction with the on-site interaction left unrenormalized. The blue dash-dotted line in the upper panel shows the effective moment $x^2_{\text{eff}}$ found from the Curie constant for $g(x) = 1$ in the MFA. Very similar results were obtained for the fcc lattice (not shown).

## 3.4 Generalized Onsager correction for itinerant systems

Onsager introduced the concept of a *cavity field* in the theory of polar liquids, which is designed to go beyond the molecular field approximation (MFA) by including short-range order effects [127]. The cavity field is the *effective* internal field which orients polar molecules in the ferroelectric phase. Onsager observed that each molecule polarizes the surrounding liquid and thereby generates a *reaction field* acting back on the molecule. However, this field is always parallel to the molecule's dipole moment and hence does not affect its orientation. Therefore, for a liquid with *permanent* dipoles the reaction field must be subtracted from the mean molecular field, the result being the cavity field. Onsager also noted that the reaction field enhances the dipole moments of real molecules due to their polarizability.

The cavity field method was successfully applied to Ising [128] and Heisenberg [129] magnets which have permanent magnetic moments. Cyrot [130, 131] noted that Moriya-Kawabata's self-consistent renormalization theory for the Hubbard model may be essentially reproduced by using Onsager-like arguments; more recently this method was implemented numerically [132, 133]. However, the actual physics there is very different; Cyrot's approach seeks the correlation correction with respect to the Hartree-Fock solution, which is unrelated to short-range order. Onsager's method was also applied to itinerant nickel [119], but, as we will see below, correct generalization to itinerant systems with LSF requires an additional ingredient which was missed in Ref. [119].

We now generalize Onsager's method to magnets with LSF described by the Hamiltonian in Eq. 3.1. Consider Eq. 3.1 above $T_c$ in a small external collinear magnetic field $H_i^{ext}\mathbf{e}_z$. We pick site 0 and integrate out the degrees of freedom from all the other sites in the partition function to obtain the effective Hamiltonian in the form of a generating functional for the lattice with a cavity [98]. Expanding this functional around the atomic limit to order $1/z$ we obtain

$$H_{\text{eff}}^0 = E(m_0) - \mathbf{m}_0 \left( \mathbf{H}_0^{ext} + \sum_i J_{0i} \langle \mathbf{m}_i^c \rangle \right) - \frac{m_0^2}{2} \sum_{ij} J_{0i} J_{0j} \chi_{ij}^c \tag{3.13}$$

where the superscript $c$ refers to the lattice with a cavity, i.e. with site 0 removed, and we used the fluctuation-dissipation theorem to express the pair correlator through the susceptibility.

In order to find the magnetization and susceptibility of the lattice with a cavity we need to solve the "impurity problem." Using the linked-cluster expansion technique [134], the longitudinal susceptibility of the original lattice can be written as follows:

$$\widehat{\chi} = \widehat{\Pi} + \widehat{\Pi}\widehat{W}\widehat{\Pi}, \tag{3.14}$$

where $\widehat{W}$ is the effective interaction that satisfies the equation $\widehat{W} = \widehat{J} + \widehat{J}\widehat{\Pi}\widehat{W}$, and $\widehat{\Pi}$ is the 1-bond-irreducible "polarization operator" which may be shown to be local to first order in $1/z$ [135]. (All quantities in Eq. 3.14 are matrices in site indices.) Removal of site 0 may be formally represented by a perturbation $\Delta\widehat{\Pi} = -\Pi_{00}\delta_{0i}\delta_{0j}$ to $\widehat{\Pi}$. (The renormalization of $\Pi_{jj}$ for $j \neq 0$ due to removal of site 0 is at least of order $1/z^2$.) Thus, denoting the effective interaction matrix for the cavity lattice as $\widehat{W_c}$, we may write $\widehat{W}_c^{-1} - \widehat{W}^{-1} = -\Delta\widehat{\Pi}$. Using Eq. 3.14 and the fact that $\widehat{\Pi}$ is diagonal, we find

$$\chi^c_{ij} = \chi_{ij} - \frac{\chi_{i0}\chi_{0j}}{\chi_{00}}. \tag{3.15}$$

The average local moments $\mathbf{M}^c_i = \langle \mathbf{m}^c_i \rangle$ for the lattice with a cavity are:

$$M^c_i = \sum_j \chi^c_{ij} H^{ext}_j = M_i - \frac{\chi_{i0}}{\chi_{00}} M_0, \tag{3.16}$$

where $M_i$ are the average local moments of the complete lattice without the cavity. The value of $\mathbf{H}^{ext}_0$ does not affect $M^c_i$ (as expected), therefore in the right-hand side of Eq. 3.16 we may take $M_i$ and $M_0$ for the actual field distribution.

From the effective Hamiltonian in Eq. 3.13 we can find the magnetization at site

0:

$$M_0 = \tilde{\chi}^0 \tilde{H}_W \tag{3.17}$$

where

$$\tilde{H}_W = H_0^{ext} + \sum_i J_{0i} \left( M_i - \frac{\chi_{i0}}{\chi_{00}} M_0 \right) \tag{3.18}$$

is the renormalized effective field (cavity field), and $\tilde{\chi}^0$ is the *renormalized* bare (atomic-limit) susceptibility. The latter may be written as $\tilde{\chi}^0 = \langle m^2 \rangle_\lambda / 3T$, where the average paramagnetic squared local moment $\langle m^2 \rangle_\lambda$ is calculated using a renormalized on-site exchange $\widetilde{I} = I + \lambda$ with $\lambda = \sum_{ij} J_{0i} J_{0j} \chi^c_{ij}$. This renormalization of the bare susceptibility is the essential ingredient needed to extend Onsager's theory to itinerant magnets. It has no effect in the localized limit where $m^2$ is constant.

As usual, we now obtain the Fourier transform of the susceptibility:

$$\chi_{\mathbf{q}} = \frac{\tilde{\chi}^0}{1 - \tilde{\chi}^0 (J_{\mathbf{q}} - \lambda)} \,, \tag{3.19}$$

where $\lambda = \sum_{\mathbf{q}} J_{\mathbf{q}} \chi_{\mathbf{q}} / \chi_{00}$. We used the same symbol $\lambda$ as above in the definition of $\widetilde{I}$, because these expressions are identical, as can now be shown with the help of Eqs. 3.19 & 3.15. Eq. 3.19 with the definitions of $\lambda$, $\tilde{\chi}^0$ and $\widetilde{I}$ form a closed set of equations for the paramagnetic susceptibility. Note that Eq. 3.19 *automatically* leads to a sum rule $\chi_{00} = \tilde{\chi}^0$, which agrees with the fluctuation-dissipation theorem.

At the Curie temperature $\chi_{\mathbf{q}}$ diverges at $\mathbf{q} = 0$. Therefore, from Eq. 3.19 we obtain $T_c = \frac{1}{3} J_0 \langle m^2(T_c) \rangle_\lambda / G$, where $G = \sum_{\mathbf{q}} (1 - J_{\mathbf{q}}/J_0)^{-1}$ is the diagonal element of the lattice Green's function [129]. Note that the value of $\lambda$ at $T_c$ is equal to $J_0(1 - G^{-1})$ and independent of the degree of itinerancy $\alpha$.

The reduced Curie temperature $t_c$ and MSRO parameter $\langle \cos\theta_{nn} \rangle$ at $T = 1.1T_c$ calculated in this way are shown in Fig. 3.6 for the bcc lattice and the PSM with $g(x) = 1$. The agreement with MC results is excellent in the whole range of $\alpha$. We repeated these calculations for the fcc lattice and found excellent agreement with MC as well. The accuracy of the predicted $t_c$ may be seen from Table 1. Similar performance for bcc and fcc lattices suggests that this approximation is not very sensitive to the connectivity of the lattice. The paramagnetic susceptibility is also shown in Fig. 3.2(e) for $\alpha = 0.48\pi$, bcc lattice, and uniform PSM. The agreement with MC results is essentially perfect outside of the narrow critical region.

Table 3.1: Reduced Curie temperature $t_c$ for bcc and fcc lattices for PSM with $g(x) = 1$: Results of the mean-field approximation (MFA), Horwitz-Callen approximation (HC), generalized Onsager method (GO) and Monte Carlo (MC).

| $\alpha/\pi$ | bcc | | | | fcc | | | |
|---|---|---|---|---|---|---|---|---|
| | MFA | HC | GO | MC | MFA | HC | GO | MC |
| 0.032 | 0.621 | 0.449 | 0.451 | 0.462(1) | 0.621 | 0.465 | 0.466 | 0.480(2) |
| 0.148 | 0.660 | 0.484 | 0.486 | 0.504(2) | 0.660 | 0.501 | 0.502 | 0.520(5) |
| 0.250 | 0.681 | 0.503 | 0.504 | 0.525(2) | 0.681 | 0.519 | 0.520 | 0.540(5) |
| 0.352 | 0.699 | 0.518 | 0.520 | 0.543(2) | 0.699 | 0.535 | 0.536 | 0.562(2) |
| 0.422 | 0.712 | 0.529 | 0.530 | 0.553(1) | 0.712 | 0.546 | 0.547 | 0.570(5) |
| 0.483 | 0.723 | 0.539 | 0.541 | 0.568(1) | 0.723 | 0.557 | 0.558 | 0.584(2) |
| 0.553 | 0.745 | 0.555 | 0.557 | 0.585(2) | 0.745 | 0.572 | 0.574 | 0.600(1) |
| 0.602 | 0.765 | 0.570 | 0.573 | 0.600(2) | 0.765 | 0.589 | 0.590 | 0.617(2) |
| 0.687 | 0.834 | 0.619 | 0.622 | 0.654(3) | 0.834 | 0.640 | 0.642 | 0.672(6) |
| 0.735 | 0.942 | 0.683 | 0.688 | 0.732(2) | 0.942 | 0.708 | 0.711 | 0.753(6) |
| 0.750 | 1 | 0.713 | 0.718 | 0.770 [136] | 1 | 0.740 | 0.743 | 0.788(3) |

The first-order terms in the $1/z$ expansion derived above introduce two corrections to the MFA calculation. The first one is the subtracted *mean* reaction field; this correction reduces the magnetization. This is the only correction in Onsager's method for systems with permanent moments. The second correction described by the last term in Eq. 3.13 adds back the *fluctuating* reaction field which is always parallel to the moment on the central site. For the Heisenberg (or Ising) model this second correction has no effect, but in itinerant systems it always increases the local moments and hence the Curie temperature. There is a strong cancelation between these two corrections in itinerant systems, and improvement compared to the MFA may be achieved only if both of them are included. Indeed, if the renormalization of the Stoner parameter is not taken into account (i.e. if the last term in Eq. 3.13 is dropped), we find a spurious strong suppression of $T_c$ for itinerant systems, as shown in Fig. 3.6(a).

It is interesting to compare the generalized Onsager method with the Horwitz-Callen (HC) approximation which is based on the "ring subset" of diagrams for the generating functional $\Phi$ in the linked-cluster technique [134, 137]. In this method, the second-order self-field $G_2$ is found by differentiating $\Phi$ with respect to the renormalized second cumulant $M_2$, while $M_2$ is represented by an integral containing $G_2$ as a parameter. This technique does not assume any particular form for the atomic limit, and therefore it can be used in our case including LSF as well. In the HC method, the on-site correlator may be found as $K_{00} = M_2 + 2M_2^2 G_2$, and the sum rule $K_{00} = 1$ is not satisfied in the paramagnetic Heisenberg magnet. However, it is easy to check that the value of $K_{00}$ at $T_c$ is smaller than 1 by less than a percent in bcc and fcc lattices. In Onsager's method for the Heisenberg model, the sum rule $K_{00} = 1$ is used to fix $M_2$ instead of the integral representation as in the HC method. The results for $T_c$ are therefore very close. We found that this close similarity remains in the entire range of $\alpha$, as seen from Table 1. The generalized Onsager's method is, however, technically much simpler.

## 3.5 Conclusions

We have studied the thermodynamics of a simple classical spin fluctuation model allowing for a variable degree of itinerancy. This model is qualitatively similar to those used before to study the thermodynamics of Fe and Ni using first-principles data [120, 121, 123]. It is worth emphasizing that the main drawback of using classical spin models of this type is the ambiguity of the phase space measure. As we showed above, the thermodynamics is very sensitive to this measure for systems with even intermediate degree of itinerancy. While the energetics of constrained spin configurations may, at least in principle, be accurately mapped using DFT calculations, it is not known (to our knowledge) how and whether the phase space measure can be supplied in a realistic way.

In the present work, we focused on the general features of the model rather than on the determination of its parameters from first principles. We found that the thermodynamic properties are similar to the results of the functional integral approach [107, 110–112]. Further, we found that the mean-field approximation is qualitatively valid, and short-range order is weak and almost independent on the degree of itinerancy up to the strongly itinerant limit where the paramagnetic susceptibility is dominated by longitudinal fluctuations. This is in agreement with earlier results for the models of Fe and Ni; [121, 123] it is clear that this is a general feature of the classical model with no frustration.

Further, we generalized the Onsager cavity field method to itinerant systems using an expansion around the atomic limit to first order in $1/z$. Both the interatomic exchange constant and the Stoner parameter are renormalized by short-range order. When both these corrections are included, the Curie temperature is in excellent agreement with Monte Carlo results. However, simple subtraction of the Onsager reaction field is a very poor approximation.

## 3.A Mathematica input code

Mathematica was used to calculate the solutions to the mean-field approximation. Below is the input code used to calculate the thermodynamic quantities discussed in the chapter.

- Solving for the self-consistent magnetization in Eq. 3.8

$$F[\mathrm{x\_},\alpha\_]{:=}(1/(1+\mathrm{Tan}[\alpha]))*\left(\tfrac{1}{2}x{}^\wedge 2+\tfrac{\mathrm{Tan}[\alpha]}{4}x{}^\wedge 4\right);$$

$$A[\mathrm{hW\_},\alpha\_,\mathrm{t\_}]{:=}\mathrm{NIntegrate}\left[g[x]*x*\mathrm{Sinh}\left[\tfrac{3*\mathrm{hW}*x}{t}\right]*e{}^\wedge\left(-\tfrac{3*F[x,\alpha]}{t}\right),\right.$$

$$\{x,0,\infty\}];$$

$$B[\mathrm{hW\_},\alpha\_,\mathrm{t\_}]{:=}\mathrm{NIntegrate}\left[g[x]*x{}^\wedge 2*\mathrm{Cosh}\left[\tfrac{3*\mathrm{hW}*x}{t}\right]*e{}^\wedge\left(-\tfrac{3*F[x,\alpha]}{t}\right),\right.$$

$$\{x,0,\infty\}];$$

$$H[\mathrm{hW\_},\alpha\_,\mathrm{t\_}]{:=}\mathrm{hW}{}^\wedge 2+\tfrac{t}{3}-\mathrm{hW}*\tfrac{B[\mathrm{hW},\alpha,t]}{A[\mathrm{hW},\alpha,t]};$$

$$f[\mathrm{hW\_},\alpha\_,\mathrm{t\_}]{:=}-(t)/3*\left(\mathrm{Log}\left[\tfrac{4*\pi*t}{3*\mathrm{hW}}*\mathrm{NIntegrate}[g[x]*\right.\right.$$

$$\left.\left.x*\mathrm{Sinh}\left[\tfrac{3*\mathrm{hW}}{t}*x\right]*e{}^\wedge\left(-\tfrac{3*F[x,\alpha]}{t}\right),\{x,0,\infty\}]\right]\right)+\tfrac{\mathrm{hW}{}^\wedge 2}{2};$$

$$g[\alpha\_,\mathrm{t\_}]{:=}-(t)/3*\left(\mathrm{Log}\left[4*\pi*\mathrm{NIntegrate}\left[g[x]*x{}^\wedge 2*e{}^\wedge\left(-\tfrac{3*F[x,\alpha]}{t}\right),\right.\right.\right.$$

$$\{x,0,\infty\}]]);$$

$$\mathrm{Clear}[a];$$

$$g[\mathrm{x\_}]{:=}1;$$

$$\alpha=0.48*\mathrm{Pi};$$

$$t=0.01;$$

$$p=1;$$

$$\mathrm{While}[t\leq 1,a[p,1]=t;$$

$\text{For}[\text{hW} = 1, H[\text{hW}, \alpha, t] > 10\hat{}(-8), \text{hW} = \text{hW} - 0.0005, \text{If}[\text{hW} < 0, \text{Break}[]]];$

$\text{If}[g[\alpha, t] \leq f[\text{hW}, \alpha, t], a[p, 2] = 0, a[p, 2] = \text{hW}];$

$p = p + 1;$

$t = t + 0.025];$

$\text{Clear}[t];$

$\text{ListPlot}[\text{Array}[a, \{p - 1, 2\}], \text{PlotRange} \to \{0, 1\},$

$\text{AxesLabel} \to \{t, \text{magnetization}\}]$

$\text{Array}[a, \{p - 1, 2\}]$

- Solving for the average square of the moment in Eq. 3.9

$F[\text{x}\_, \alpha\_] := (1/(1 + \text{Tan}[\alpha])) * \left(\frac{1}{2}x\hat{}2 + \frac{\text{Tan}[\alpha]}{4}x\hat{}4\right);$
$A[\text{hW}\_, \alpha\_, \text{t}\_] := \text{NIntegrate}\left[g[x] * x * \text{Sinh}\left[\frac{3*\text{hW}*x}{t}\right] * e\hat{}\left(-\frac{3*F[x,\alpha]}{t}\right),\right.$

$\left.\{x, 0, \infty\}\right];$

$B[\text{hW}\_, \alpha\_, \text{t}\_] := \text{NIntegrate}\left[g[x] * x\hat{}2 * \text{Cosh}\left[\frac{3*\text{hW}*x}{t}\right] * e\hat{}\left(-\frac{3*F[x,\alpha]}{t}\right),\right.$

$\left.\{x, 0, \infty\}\right];$

$Z[\text{hW}\_, \alpha\_, \text{t}\_] := \text{NIntegrate}\left[g[x] * x\hat{}3 * \text{Sinh}\left[\frac{3*\text{hW}*x}{t}\right] * e\hat{}\left(-\frac{3*F[x,\alpha]}{t}\right),\right.$

$\left.\{x, 0, \infty\}\right];$

$a[\alpha\_, \text{t}\_] := \text{NIntegrate}\left[g[x] * x\hat{}2 * e\hat{}\left(-\frac{3*F[x,\alpha]}{t}\right),\right.$

$\left.\{x, 0, \infty\}\right];$

$z[\alpha\_, \text{t}\_] := \text{NIntegrate}\left[g[x] * x\hat{}4 * e\hat{}\left(-\frac{3*F[x,\alpha]}{t}\right),\right.$

$\left.\{x, 0, \infty\}\right];$

$H[\text{hW}\_, \alpha\_, \text{t}\_] := \text{hW}\hat{}2 + \frac{t}{3} - \text{hW} * \frac{B[\text{hW},\alpha,t]}{A[\text{hW},\alpha,t]};$

$f[\text{hW}\_, \alpha\_, \text{t}\_] := -(t)/3 * \left(\text{Log}\left[\frac{4*\pi*t}{3*\text{hW}} * \text{NIntegrate}[g[x]*\right.\right.$

$\left.\left. x * \text{Sinh}\left[\frac{3*\text{hW}}{t} * x\right] * e\hat{}\left(-\frac{3*F[x,\alpha]}{t}\right), \{x, 0, \infty\}]\right]\right) + \frac{\text{hW}\hat{}2}{2};$

$g[\alpha\_, \text{t}\_] := -(t)/3 * \left(\text{Log}\left[4 * \pi * \text{NIntegrate}\left[g[x] * x\hat{}2 * e\hat{}\left(-\frac{3*F[x,\alpha]}{t}\right),\right.\right.\right.$

$\left.\left.\left.\{x, 0, \infty\}\right]\right]\right);$

```
x2[α_, t_, hW_]:=Z[hW, α, t]/A[hW, α, t];
x2tc[α_, t_]:=z[α, t]/a[α, t];


g[x_]:=1;
t = 0.01;
α = 0.48 ∗ Pi;
p = 1;
q = 1;
While[t ≤ 1, c[p, 1] = t;
For[hW = 1, H[hW, α, t] > 10^(−8), hW = hW − 0.0005, If[hW < 0, Break[]]];
If[g[α, t] ≤ f[hW, α, t], c[p, 2] = x2tc[α, c[p, 1]];
Break[], d[q] = hW];
c[p, 2] = x2[α, c[p, 1], d[q]];
p = p + 1;
q = q + 1;
t = t + 0.025];
While[t ≤ 1.6, c[p, 1] = t;
c[p, 2] = x2tc[α, c[p, 1]];
p = p + 1;
t = t + 0.025];
Clear[t];
ListPlot[Array[c, {p − 1, 2}], AxesLabel → {t, moment^2}]
Array[c, {p − 1, 2}]
```

- Solving for the paramagnetic susceptibility in Eq. 3.11

$F[\mathrm{x\_},\alpha\_]{:=}(1/(1+\mathrm{Tan}[\alpha]))*\left(\frac{1}{2}x{}^\wedge 2+\frac{\mathrm{Tan}[\alpha]}{4}x{}^\wedge 4\right);$

$a[\alpha\_,\mathrm{t\_}]{:=}\mathrm{NIntegrate}\left[g[x]*x{}^\wedge 2*e{}^\wedge\left(-\frac{3*F[x,\alpha]}{t}\right),\right.$

$\{x,0,\infty\}];$

$z[\alpha\_,\mathrm{t\_}]{:=}\mathrm{NIntegrate}\left[g[x]*x{}^\wedge 4*e{}^\wedge\left(-\frac{3*F[x,\alpha]}{t}\right),\right.$

$\{x,0,\infty\}];$

$\chi_P[\alpha\_,\mathrm{t\_}]{:=}\frac{\frac{1}{3}\frac{z[\alpha,t]}{a[\alpha,t]}}{\frac{t}{3}-\frac{1}{3}*\frac{z[\alpha,t]}{a[\alpha,t]}};$

$g[\mathrm{x\_}]{:=}1;$

$\alpha=0.48*\mathrm{Pi};$

$p=1;$

$t=0.01;$

$\mathrm{While}[t\leq 2,c[p,1]=t;$

$c[p,2]=\chi_P[\alpha,t];$

$p=p+1;$

$t=t+0.025];$

$\mathrm{pp2}=\mathrm{Plot}\left[1/\chi_P[\alpha,t]\right],\{t,0.05,4\},$

$\mathrm{PlotStyle}\to\mathrm{Hue}[.7],\mathrm{AxesLabel}\to\{t,\chi{}^\wedge(-1)\}];$

$\mathrm{Show}[\mathrm{pp2},\mathrm{AxesLabel}\to\{t,\chi{}^\wedge(-1)\}]$

$\mathrm{Array}[c,\{p-1,2\}]$

- Solving for $t_c$ as a function of $\alpha$ for uniform measure $g(x)=1$

$F[\mathrm{x\_},\alpha\_]{:=}(1/(1+\mathrm{Tan}[\alpha]))*\left(\frac{1}{2}x{}^\wedge 2+\frac{\mathrm{Tan}[\alpha]}{4}x{}^\wedge 4\right);$

$a[\alpha\_,\mathrm{t\_}]{:=}\mathrm{NIntegrate}\left[g[x]*x{}^\wedge 2*e{}^\wedge\left(-\frac{3*F[x,\alpha]}{t}\right),\right.$

$\{x,0,\infty\}];$

$z[\alpha\_,\mathrm{t\_}]{:=}\mathrm{NIntegrate}\left[g[x]*x{}^\wedge 4*e{}^\wedge\left(-\frac{3*F[x,\alpha]}{t}\right),\right.$

$\{x,0,\infty\}];$

$M[\alpha\_,\mathrm{t}\_]{:=}\left(\frac{z[\alpha,t]}{a[\alpha,t]}\right)-t;$

$g[\mathrm{x}\_]{:=}1;$

$\alpha=0.01;$

$p=1;$

$\mathrm{While}[\alpha\leq 3*\mathrm{Pi}/4, c[p,1]=\alpha;$

$\mathrm{For}[t=0.001, M[\alpha,t]>10\hat{}(-9), t=t+0.0005, \mathrm{If}[t>2,\mathrm{Break}[]]];$

$c[p,2]=t;$

$p=p+1;$

$\alpha=\alpha+0.05];$

$\mathrm{Clear}[\alpha];$

$\mathrm{Clear}[t];$

$\mathrm{ListPlot}[\mathrm{Array}[c,\{p-1,2\}],\mathrm{AxesLabel}\to\{\alpha,t\}]$

$\mathrm{Array}[c,\{p-1,2\}]$

- Solving for $t_c$ as a function of $\alpha$ for reduced measure $g(x)=x^{-2}$

$F[\mathrm{x}\_,\alpha\_]{:=}(1/(1+\mathrm{Tan}[\alpha]))*\left(\frac{1}{2}x\hat{}2+\frac{\mathrm{Tan}[\alpha]}{4}x\hat{}4\right);$

$A[\mathrm{hW}\_,\alpha\_,\mathrm{t}\_]{:=}\mathrm{NIntegrate}\left[g[x]*x*\mathrm{Sinh}\left[\frac{3*\mathrm{hW}*x}{t}\right]*e\hat{}\left(-\frac{3*F[x,\alpha]}{t}\right),\right.$

$\left.\{x,0,\infty\}\right];$

$B[\mathrm{hW}\_,\alpha\_,\mathrm{t}\_]{:=}\mathrm{NIntegrate}\left[g[x]*x\hat{}2*\mathrm{Cosh}\left[\frac{3*\mathrm{hW}*x}{t}\right]*e\hat{}\left(-\frac{3*F[x,\alpha]}{t}\right),\right.$

$\left.\{x,0,\infty\}\right];$

$H[\mathrm{hW}\_,\alpha\_,\mathrm{t}\_]{:=}\mathrm{hW}\hat{}2+\frac{t}{3}-\mathrm{hW}*\frac{B[\mathrm{hW},\alpha,t]}{A[\mathrm{hW},\alpha,t]};$

$f[\mathrm{hW}\_,\alpha\_,\mathrm{t}\_]{:=}-(t)/3*\left(\mathrm{Log}\left[\frac{4*\pi*t}{3*\mathrm{hW}}*\mathrm{NIntegrate}[g[x]*\right.\right.$

$\left.\left.x*\mathrm{Sinh}\left[\frac{3*\mathrm{hW}}{t}*x\right]*e\hat{}\left(-\frac{3*F[x,\alpha]}{t}\right),\{x,0,\infty\}]\right]\right)+\frac{\mathrm{hW}\hat{}2}{2};$

$g[\alpha\_,\mathrm{t}\_]{:=}-(t)/3*\left(\mathrm{Log}\left[4*\pi*\mathrm{NIntegrate}\left[g[x]*x\hat{}2*e\hat{}\left(-\frac{3*F[x,\alpha]}{t}\right),\right.\right.\right.$

$\left.\left.\left.\{x,0,\infty\}\right]\right]\right);$

```
g[x_]:=1/x^2;
t = 0.001;
α = 0.01;
p = 1;
While[α ≤ 3 ∗ Pi/4, c[p, 1] = α;
While[t < 0.4,
For[hW = 1, H[hW, α, t] > 10^(−9), hW = hW − 0.0005, If[hW < 0, Break[]]];
If[g[α, t] ≤ f[hW, α, t], c[p, 2] = t;
Break[]];
If[hW < 0.002, c[p, 2] = t;
Break[], t = t + 0.0025]];
Clear[t];
p = p + 1;
t = 0.001;
α = α + 0.05]
Clear[t];
Clear[α];
ListPlot[Array[c, {p − 1, 2}], AxesLabel → {α, t}]
Array[c, {p − 1, 2}]
```

- Solving for $x_{\text{eff}}^2 = 3/C$ and $\langle x^2(t_c)\rangle$ as a function of $\alpha$ for uniform measure $g(x) = 1$

```
F[x_, α_]:=(1/(1 + Tan[α])) ∗ (1/2 x^2 + Tan[α]/4 x^4);
A[α_, t_]:=NIntegrate[g[x] ∗ x^2 ∗ (3 ∗ F[x, α]) ∗ e^(−3∗F[x,α]/t),
{x, 0, ∞}];
```

$Z[\alpha\_,\mathrm{t\_}]\text{:=}\mathrm{NIntegrate}\left[g[x]*x\textasciicircum 4*(3*F[x,\alpha])*e\textasciicircum\left(-\frac{3*F[x,\alpha]}{t}\right),\right.$

$\{x,0,\infty\}];$

$a[\alpha\_,\mathrm{t\_}]\text{:=}\mathrm{NIntegrate}\left[g[x]*x\textasciicircum 2*e\textasciicircum\left(-\frac{3*F[x,\alpha]}{t}\right),\right.$

$\{x,0,\infty\}];$

$z[\alpha\_,\mathrm{t\_}]\text{:=}\mathrm{NIntegrate}\left[g[x]*x\textasciicircum 4*e\textasciicircum\left(-\frac{3*F[x,\alpha]}{t}\right),\right.$

$\{x,0,\infty\}];$

$M[\alpha\_,\mathrm{t\_}]\text{:=}\left(\frac{z[\alpha,t]}{a[\alpha,t]}\right)-t;$

$m[\alpha\_,\mathrm{t\_}]\text{:=}3/\mathrm{x2tc}[\alpha,t]*(1+1/(t*\mathrm{x2tc}[\alpha,t])*$

$(z[\alpha,t]/(a[\alpha,t])\textasciicircum 2*A[\alpha,t]-Z[\alpha,t]/a[\alpha,t]));$

$\mathrm{x2tc}[\alpha\_,\mathrm{t\_}]\text{:=}z[\alpha,t]/a[\alpha,t];$

$g[\mathrm{x\_}]\text{:=}1;$

$\alpha=0.01;$

$p=1;$

$\mathrm{While}[\alpha\leq 3*\mathrm{Pi}/4,c[p,1]=\alpha;$

$d[p,1]=\alpha;$

$\mathrm{For}[t=0.001,M[\alpha,t]>10\textasciicircum(-8),t=t+0.001,\mathrm{If}[t>2,\mathrm{Break}[]]];$

$c[p,2]=3/(m[\alpha,t]);$

$d[p,2]=\mathrm{x2tc}[\alpha,t];$

$p=p+1;$

$\alpha=\alpha+0.05];$

$\mathrm{plot1}=\mathrm{ListPlot}[\mathrm{Array}[c,\{p-1,2\}],\mathrm{AxesLabel}\to\{\alpha,3/C\}];$

$\mathrm{Array}[c,\{p-1,2\}]$

$\mathrm{plot2}=\mathrm{ListPlot}[\mathrm{Array}[d,\{p-1,2\}],\mathrm{AxesLabel}\to\{\alpha,x\textasciicircum(-2)\}];$

$\mathrm{Array}[d,\{p-1,2\}]$

$\mathrm{Show}[\{\mathrm{plot1},\mathrm{plot2}\}]$

## Chapter 4

# Spin injection from a half-metal at finite temperatures

## 4.1 Introduction

Many spintronic devices depend on the injection, manipulation, and detection of spin-polarized currents in semiconductors or normal metals [138–140]. Spin injection can also be utilized as a tool to probe the spectroscopic properties of strongly correlated and spin-orbit-coupled systems [138, 141]. Thus, understanding the mechanisms of spin injection is of interest for a variety of fundamental and practical applications. Basic theory of spin injection across an F/N (ferromagnet/normal metal) interface in the linear response regime was worked out by Johnson and Silsbee [38]. As shown in Sec. 1.5 and Eq. 1.74, the spin polarization of the injected current may be conveniently expressed as [43, 138]

$$P_j = \frac{P_\sigma r_F + P_\Sigma r_c}{r_F + r_N + r_c}, \tag{4.1}$$

where $P_\sigma = (\sigma_\uparrow - \sigma_\downarrow)/(\sigma_\uparrow + \sigma_\downarrow)$, $\sigma_\uparrow$ and $\sigma_\downarrow$ are the spin-resolved conductivities of the ferromagnetic electrode, $P_\Sigma$ is defined similar to $P_\sigma$ for the spin-dependent interface conductance, while $r_F$ and $r_N$ are effective resistances of the ferromagnet and normal metal, respectively. The effective interface resistance is denoted $r_c$. For the ferromagnet $r_F = (\sigma_\uparrow + \sigma_\downarrow) l_{sf}^F / (4\sigma_\uparrow\sigma_\downarrow)$ and for the normal metal $r_N = l_{sf}^N/\sigma_N$, where $l_{sf}^F$ and $l_{sf}^N$ are the spin-diffusion lengths in the ferromagnet and in the normal metal. The quantities $r_F$ and $r_N$ are called effective resistances. Eq. 4.1 is valid under the assumptions of the two-current model [50], i. e. when the spin-diffusion lengths are much longer than the mean-free paths [41]. Note that nonlinear effects in bipolar semiconducting junctions [142, 143] can not be described within the linear-response theory and are beyond the scope of the present consideration.

Spin injection from a ferromagnet into a semiconductor is subject to the so-called conductivity mismatch problem [51]. For a typical choice of materials we have $l_{sf}^N \gg l_{sf}^F$ and $\sigma_N \ll \sigma_\uparrow\sigma_\downarrow/(\sigma_\uparrow+\sigma_\downarrow)$. This implies that $r_F \ll r_N$, and if the interface resistance $r_c$ is also small compared to $r_N$, the injected current is unpolarized, $P_j \ll 1$. In order to circumvent this problem, one can introduce a highly resistive, spin-selective barrier at the interface, such as a naturally occurring Schottky barrier or an artificially inserted tunnel junction [43]. According to Eq. 4.1, large $r_c$ (comparable to or greater than $r_N$) combined with appreciable $P_\Sigma$ results in a finite $P_j$. Efficient spin injection into GaAs and Si from transition-metal electrodes was successfully achieved based on this principle [144–147].

The situation can be visualized with the help of an effective resistor circuit, such that in each spin channel $s$ the ferromagnet and the normal metal have resistances $l_{sf}^F/\sigma_s$ and $2l_{sf}^N/\sigma_N$, respectively, and the two spin channels are connected in parallel [53]. This effective circuit correctly reproduces both the spin polarization of the current near the interface and the resistance of the junction in excess of what would be measured if the interface were replaced by a node in the circuit [53].

Half-metallic ferromagnets [148] are conducting in one spin channel and insulating in the other, which makes them attractive candidates as electrode materials for spintronic devices [138]. The situation at zero temperature is simple, as there is only one conducting channel ("spin up"), and the injected current should be fully spin-polarized. Many materials, particularly among Heusler compounds, have been theoretically predicted using band structure calculations to be half-metallic [149], although reliable experimental confirmation is often complicated by surface effects [150]. High magnetoresistance values were achieved in magnetic tunnel junctions [151–154] and spin valves [155] with epitaxial Co-based Heusler-alloy electrodes. Large nonlocal spin signals, 10 times higher compared to conventional electrodes, were also demonstrated in lateral spin valves with transparent ohmic interfaces [156–158]. In all of these experiments the spin signal is considerably reduced at room temperature but remains appreciable. Further, Ramsteiner *et al.* [159] demonstrated spin injection from $Co_2FeSi$ into an (Al,Ga)As light-emitting diode (LED) structure with an efficiency of at least 50%. Based on their device design, they concluded that the Schottky barrier can not be present at the interface and argued that the observed efficient spin injection "casts doubt onto the common belief that tunneling is a prerequisite for spin injection from a metal into a semiconductor."

So far the theoretical analysis of spintronic devices with half-metallic electrodes was based [156–158] on the standard spin-diffusion model [38, 41, 43, 138, 160], which assumes the existence of two weakly coupled conducting channels in each material [41, 50]. However, these validity criteria are not satisfied in true half-metals, and our present goal is to develop an appropriate formalism for such devices, which should include the effects of thermal spin fluctuations at finite temperatures. Due to these fluctuations, the electron wavefunctions lose their pure spin character, and the density of states (DOS) in a half-metal acquires non-zero projection onto the "spin down" channel, which is gapped at zero temperature. However, this state can be viewed as a small perturbation of the fully collinear spin state by fluctuating transverse magnetic fields, so that the local spin direction for all electronic eigenstates is fluctuating within a narrow cone around the magnetization direction. In other words, the number of eigenstates is not doubled, but rather they acquire a small spin-down component. In this situation one can not apply the two-current model, in which independent distribution functions are introduced for spin-up and spin-down electrons, and the concept of the spin-diffusion length also becomes meaningless. Therefore, Eq. 4.1 can not be directly applied to spin injection from a half-metallic electrode at $T \neq 0$.

In the following, we analyze the spin injection from a half-metallic electrode in the linear response regime but without making the assumptions of the two-current model leading to Eq. 4.1. We start with general considerations in Sec. 4.2 and then proceed to analyze the elastic scattering region using the random matrix theory in Sec. 4.3. Here we derive the formula for spin injection efficiency, which is similar to Eq. 4.1 but with the effective resistance $\tilde{r}_F$ being controlled by spin-flip scattering probabilities at the interface. A generalized statement of the conductivity mismatch follows from the unitarity of the scattering matrix. Based on these results, we then describe the half-metallic spin-injection system within the spin-diffusion theory in Sec. 4.4. The formula for spin-injection efficiency is generalized in a natural way to the case of finite spin-diffusion length in the normal region. In Sec. 4.5 we discuss the behavior of spin-injection efficiency, and finally in Sec. 4.6 we support our conclusions with explicit tight binding *s*-*d* model calculations. The conclusions are summarized in Sec. 4.7.

## 4.2 Half-metal at a finite temperature

The electronic structure of a half-metal at $T = 0$ has a band gap in one of the spin channels. If we now consider a thermal fluctuation resulting in a small canting of individual local spin moments, we can imagine, on the level of an the self-consistent field theory in the localized basis, that the effective fields on different atomic sites have been rigidly rotated off of the magnetization axis by small angles. (The tight-binding representation is assumed for simplicity and is not essential for the physical argument.) This is a common approach to spin fluctuations within the noncollinear density functional theory, whereby the spin moments are assumed to fluctuate adiabatically slowly compared with electron hopping times [116]. This approximation is justified by the fact that typical times associated with magnon dynamics are much longer compared to the electron momentum relaxation time. The Hamiltonian of the system with such adiabatic spin fluctuation can then be represented as [161]

$$H\{\widehat{n}_i\} = \sum_i U(\widehat{n}_i) H_i U^+(\widehat{n}_i) + K \tag{4.2}$$

where $\widehat{n}_i$ is the unit vector parallel to the spin moment on site $i$, $H_i$ is the on-site contribution to the Hamiltonian from site $i$, and $K$ is the spin-diagonal kinetic (hopping) part. We can now make a unitary transformation to the new "rotated" local basis in which $H_i$ is diagonal, which is effected by unitary matrices $U(\widehat{n}_i)$. In this new basis the Hamiltonian is

$$\tilde{H}\{\widehat{n}_i\} = \sum_i H_i + \sum_{ij} U^+(\widehat{n}_i) K_{ij} U(\widehat{n}_j). \tag{4.3}$$

At zero temperature there are only states of a particular spin (say, "up") near the Fermi level. Deviation of the unitary matrices in Eq. 4.3 from unity at $T \neq 0$

introduces hybridization between local spin-up and spin-down states, as well as some randomness in the spin-conserving hopping matrix elements. The Bloch states near the Fermi level acquire a small admixture of spin-down character, and the DOS in the global basis acquires a spin-down component, but no new Bloch states appear near the Fermi level. This means that the bulk of a half-metal at finite (but low) temperatures can be treated as having one effective spin channel. This situation is qualitatively different from a conventional ferromagnet with two independent spin channels, even if they have very different resistivities. While the conventional ferromagnet has two independent occupation functions and chemical potentials for the two spin channels, a half-metal has only one. Transport across an interface with a normal metal is discussed in the subsequent sections.

## 4.3 Spin injection in the scattering formalism

A spin injection device can be analyzed by treating the F/N interface as an elastic scattering region embedded between diffusive regions, and by matching the solution of the scattering problem with the solution of the spin-diffusion equation. For a conventional two-channel ferromagnetic electrode the well-known result is given by Eq. 4.1. However, as we have argued in Sec. 4.2, the two-current model is inapplicable for a half-metallic electrode. The purpose of this section is to understand the role of spin coherence for spin injection from the half-metal at finite temperatures, i. e. in the presence of spin disorder.

Since the half-metal, as argued above, has only one effective spin channel, there is no analog of the spin-diffusion length for it. Therefore, inelastic scattering should not affect the properties of spin injection, and we may treat the whole half-metallic electrode as an elastic scatterer. As we will see in the next section, matching with the solution of the spin-diffusion equation in the normal metal should simply replace the resistance of the normal region by its effective resistance $r_N = \rho_N l_{sf}^N$. Therefore, we first consider the entire spin-injection device disregarding inelastic scattering altogether.

An elastic spin-injection device can be considered in the formalism of the scattering theory. We assume that the F-N device is connected on both sides to equilibrium reservoirs via ideal Landauer leads. Apart from these leads we introduce an auxiliary lead in the N region at such distance from the interface (a few mean-free paths) that the quantum interference effects occurring at the interface are left entirely on the left-hand side of this lead. Each of the two regions can be described by a scattering matrix:

$$\widehat{S}_F = \begin{pmatrix} \widehat{r}_1 & \widehat{t}'_1 \\ \widehat{t}_1 & \widehat{r}'_1 \end{pmatrix} \quad , \quad \widehat{S}_N = \begin{pmatrix} \widehat{r}_2 & \widehat{t}'_2 \\ \widehat{t}_2 & \widehat{r}'_2 \end{pmatrix}, \tag{4.4}$$

where, in the standard way, the matrix $\widehat{t}_1$ contains amplitudes for transmission from the conducting channels of the left electrode across F into the conducting channels of the fictitious lead, and similarly for the other subblocks. At this point we allow the F region to have an arbitrary magnetic configuration. The transmission matrix $\widehat{t}$ of the entire F-N junction is

$$\widehat{t} = \widehat{t}_2(1 - \widehat{r}'_1\widehat{r}_2)^{-1}\widehat{t}_1. \tag{4.5}$$

The charge and spin currents flowing across the junction are proportional, respectively, to $C$ and $C_s$:

$$C = \mathrm{Tr}\, \widehat{t}\widehat{t}^{+} \quad , \quad C_s = \mathrm{Tr}\, \widehat{\sigma}_z \widehat{t}\widehat{t}^{+}, \tag{4.6}$$

and we are interested in the spin polarization $P_j = C_s/C$. Since we are considering the junction as an elastic scattering region, the spin current in the normal region is conserved. There is no loss of generality from singling out the $z$ axis, because its direction is unspecified.

Following the approach of Waintal *et al.* [162], we now introduce the polar decomposition [163] of the matrix $\widehat{S}_N$:

$$\widehat{S}_N = \begin{pmatrix} \widehat{U} & 0 \\ 0 & \widehat{V}' \end{pmatrix} \begin{pmatrix} \sqrt{1-T} & i\sqrt{T} \\ i\sqrt{T} & \sqrt{1-T} \end{pmatrix} \begin{pmatrix} \widehat{U}' & 0 \\ 0 & \widehat{V} \end{pmatrix} \tag{4.7}$$

where $T$ is the matrix of the eigenvalues of $\widehat{t_2}\widehat{t_2^+}$, while $\widehat{U}$, $\widehat{U}'$, $\widehat{V}$, and $\widehat{V}'$ are unitary matrices, which are all diagonal in spin space. Since the fictitious node can be introduced at a sufficient distance from the surface to eliminate all quantum interference effects, we can safely use the isotropic approximation [164], i. e. assume that the spatial factors of the unitary matrices $\widehat{U}$, $\widehat{U}'$, $\widehat{V}$, and $\widehat{V}'$ are distributed uniformly in the unitary group. We substitute Eq. 4.5 in Eq. 4.6, use Eq. 4.7 for $\widehat{t_2}$ and $\widehat{r'_2}$, and integrate over the unitary ensemble. This integration is easily performed using the method of Ref. [165] to the leading order in the number of conducting channels in the leads. In this leading order, each unitary matrix is matched to its own conjugate, resulting in a ladder diagram [165]. Averaging over the eigenvalues of $\widehat{t_2}\widehat{t_2^+}$ is performed simultaneously. The result can be written in this form:

$$C_s = \sum_{\lambda\mu} \sigma^z_\lambda \left[1 - \widehat{R}(1-T_N)\right]^{-1}_{\lambda\mu} T_\mu T_N. \tag{4.8}$$

Here $\lambda$ and $\mu$ denote a pair of spin indices, $\sigma^z_\lambda$ is the $\widehat{\sigma}_z$ matrix written as a vector $(1, 0, 0, -1)$, $T_N$ is the probability of transmission through the N region, $\widehat{R}$ is a $4 \times 4$ matrix [162] with elements

$$R_{\lambda\mu} \equiv R_{\sigma\sigma',ss'} = \frac{1}{N_{ch}} \sum_{mn} (r'_1)_{m\sigma,ns} (r'_1)^*_{m\sigma',ns'} \tag{4.9}$$

where $m$, $n$ enumerate the $N_{ch}$ conducting channels in the auxiliary lead, and $T_\mu$ is a 4-vector with elements

$$T_\mu \equiv T_{ss'} = \frac{1}{N_{ch}} \sum_{mn\sigma} (t_1)_{ms,n\sigma} (t_1)^*_{ms',n\sigma}. \tag{4.10}$$

In this last expression $n\sigma$ labels the channels of the lead feeding the F region. The expression for $C$ is obtained from Eq. 4.8 replacing $\sigma^z_\lambda$ by a 4-vector representation of the unit matrix $1_\lambda = (1, 0, 0, 1)$. Note that $T_\mu = \sum_\lambda T_{\mu\lambda} 1_\lambda$, where $T_{\mu\lambda}$ is defined as $R_{\mu\lambda}$ but with matrix elements of $t_1$ instead of $r'_1$.[1]

The unitarity of $\widehat{S}_F$ requires that $\widehat{t}_1 \widehat{t}_1^+ + \widehat{r}' \widehat{r}'^+ = 1$. This condition implies that $T_\lambda = \sum_\mu (\delta_{\lambda\mu} - R_{\lambda\mu}) 1_\mu$. Substituting this in Eq. 4.8 we find that $C_s$ vanishes to first order in $T_N$. Since the charge current is proportional to $T_N$, this leads to $P_j \to 0$ at $T_N \to 0$. In the limit of a two-channel device with weak coupling between the channels, this result reduces to the conductivity mismatch obstacle for spin injection [51]. However, our result is more general, because it is valid for any magnetic structure of the F region and for any choice of the $z$ axis. The only exception is the case of a half-metal at $T = 0$ with no spin-flip scattering at the interface, for which the only non-zero component of $T_\mu$ is $T_{\uparrow\uparrow}$ (in the reference frame where the $z$ axis is aligned with the magnetization). In this exceptional case we obviously have $P_j = 1$ at any $T_N$.

Let us now find the spin polarization $P_j$ for a finite $T_N$, assuming that the electrode is an axially symmetric (i. e. collinear) magnet with spin disorder. For a macroscopic interface, the summation over the conducting channels automatically averages $R_{\lambda\mu}$ and $T_\mu$ in Eq. 4.8 over the spin disorder ensemble. This self-averaging does not necessarily occur in a point-contact, in which case an additional averaging over spin

---

[1] In the notation of Ref. [162], matrices $R_{\lambda\mu}$ and $T_{\lambda\mu}$ correspond to the “hat-matrices” generated by $r'_1$ and $t_1$.

disorder configuration is required for the spin current in Eq. 4.8 and its charge counterpart. Re-expanding the inverse matrix in Eq. 4.8, we can obtain a series of terms describing multiple scatterings at the interface. Since the electron scatters repeatedly from the same spin disorder configuration, the averages of the matrix products do not decouple. However, since correlations between successive scattering events do not change the asymptotic behavior of $P_j$, it is a reasonable approximation to replace $\widehat{R}$ and $T_\mu$ by their averages $\langle\widehat{R}\rangle$ and $\langle T_\mu\rangle$ even for a point contact.

Let us assume that spin-orbit coupling at the surface is weak, and that all spin-flip processes are dominated by spin-disorder scattering. Then the matrices $\langle\widehat{R}\rangle$ and $\langle T_\mu\rangle$ should be invariant with respect to rotation in spin space around the magnetization axis. This condition implies that $\langle T_{\uparrow\downarrow}\rangle$ and $\langle T_{\downarrow\uparrow}\rangle$ vanish, along with all elements $\langle R_{\sigma\sigma',ss'}\rangle$ with $\sigma - \sigma' \neq s - s'$. The $\langle\widehat{R}\rangle$ matrix is thus block-diagonal. From the structure of Eq. 4.8 it is clear that we are only interested in the $2 \times 2$ block spanned by indices 1 and 4. (The 22 and 33 diagonal elements represent the spin-mixing conductance [166], which turns out to be irrelevant to the problem at hand.) As seen from Eq. 4.9, the diagonal elements of this block are the total spin-conserving reflection probabilities for spin-up and spin-down electrons $R_\uparrow = \langle R_{\uparrow\uparrow,\uparrow\uparrow}\rangle$ and $R_\downarrow = \langle R_{\downarrow\downarrow,\downarrow\downarrow}\rangle$, while the off-diagonal elements are the total spin-flip reflection probabilities $R_{\uparrow\downarrow} = \langle R_{\uparrow\uparrow,\downarrow\downarrow}\rangle$. Reciprocity requires that $\langle R_{\uparrow\uparrow,\downarrow\downarrow}\rangle = \langle R_{\downarrow\downarrow,\uparrow\uparrow}\rangle$. Let us also denote $T_\uparrow = T_{\uparrow\uparrow}$ and $T_\downarrow = T_{\downarrow\downarrow}$. (Note that $T_\uparrow$ and $T_\downarrow$ include both spin-conserving and spin-flip processes.) We can now calculate the spin polarization from Eq. 4.8:

$$P_j = \frac{P_t \tilde{r}_F}{\tilde{r}_F + r_N} \tag{4.11}$$

where $P_t = (T_\uparrow - T_\downarrow)/(T_\uparrow + T_\downarrow)$, $r_N G_N = (1 - T_N)/(2T_N)$,

$$\frac{1}{4G_N \tilde{r}_F} = \frac{T_\uparrow T_\downarrow}{T_\uparrow + T_\downarrow} + R_{\uparrow\downarrow}, \tag{4.12}$$

and $G_N = (e^2/h)N_{ch}$. Note that $P_t$ is the spin polarization of the current injected in the auxiliary lead if the N region is detached from it.

The expression in Eq. 4.11 includes the effects of spin disorder, but not the effects of inelastic spin relaxation. For a conventional (not half-metallic) electrode, spin relaxation must be included on both sides of the junction. In the presence of spin-flip processes at the interface, the solution of the spin-diffusion equations becomes rather complicated [44] even if spin-flip reflection $R_{\uparrow\downarrow}$ is neglected. The situation is simpler in the case of a half-metallic electrode, because inelastic spin relaxation should only be included in the N region. In the next section we will see that in this case the elastic resistance of the normal region $r_N$ in Eq. 4.11 should simply be replaced by its effective resistance.

Note that interfacial spin-flip scattering due to spin-orbit interaction was studied in some detail for metallic N/N and F/N interfaces [167, 168]. Temperature-dependent interfacial spin-flip scattering in the presence of non-equilibrium spin accumulation was suggested as a source of asymmetric response in a nonlocal spin valve [169].

## 4.4 Semiclassical theory

In the previous section we found that under rather general assumptions the scattering at the interface between the half-metal and the normal metal is described completely by spin-dependent transmission probabilities and the spin-flip reflection probability on the normal metal side. The effects of spin coherence are effectively eliminated by spin disorder averaging. We can therefore use the standard semi-classical treatment, taking into account that the half-metal has only one spin channel, and incorporating spin-flip scattering at the interface. Apart from giving a complementary picture of spin injection, this treatment confirms the expectation about the role of the spin-diffusion length in the normal metal and shows the invariance of the results with respect to the location of the left lead.

Instead of treating the whole F/N device as an elastic scatterer, we now consider only the interfacial F/N region (a few mean-free paths on both sides) embedded between infinite diffusive regions. The half-metallic (F) region carries only one spin channel (even at finite temperature), but the N region has two channels. Similarly to Rashba's treatment of the F-N junction with spin-flip transmission at the interface [44], the interface is assigned the spin-flip conductance $\Sigma_{\uparrow\downarrow}$ in addition to the spin-conserving $\Sigma_{\uparrow\uparrow}$. In addition to these terms, we also need to introduce spin relaxation in the normal metal due to spin-flip scattering at the interface. Physically, even if the F electrode is insulating, the spin accumulation in the normal metal can relax through interfacial spin-flip scattering. Introducing the appropriate electrochemical potential drops at the interface, the spin-dependent currents on the normal metal side of the interface can be written as follows:

$$j_\uparrow^N(0) = \Sigma_{\uparrow\uparrow}(\zeta_\uparrow^N - \zeta^F) + \tilde{R}_{\uparrow\downarrow}(\zeta_\uparrow^N - \zeta_\downarrow^N), \tag{4.13}$$

$$j_\downarrow^N(0) = \Sigma_{\uparrow\downarrow}(\zeta_\downarrow^N - \zeta^F) + \tilde{R}_{\uparrow\downarrow}(\zeta_\downarrow^N - \zeta_\uparrow^N), \tag{4.14}$$

where the new term is the one with $\tilde{R}_{\uparrow\downarrow}$. Matching with the solution of the spin-diffusion equation can be worked out in the usual way [44]. The terms containing bulk conductivity in the F region drop out, and after some algebra we reproduce Eq. 4.11 with $r_N$ now being the effective resistance $\rho_N l_{sf}^N$ (as anticipated), $P_t$ replaced by $P_\Sigma = (\Sigma_{\uparrow\uparrow} - \Sigma_{\uparrow\downarrow})/(\Sigma_{\uparrow\uparrow} + \Sigma_{\uparrow\downarrow})$, and

$$\frac{1}{4\tilde{r}_F} = \frac{\Sigma_{\uparrow\uparrow}\Sigma_{\uparrow\downarrow}}{\Sigma_{\uparrow\uparrow} + \Sigma_{\uparrow\downarrow}} + \tilde{R}_{\uparrow\downarrow}. \tag{4.15}$$

Eq. 4.15 is equivalent to Eq. 4.12 with the replacement $G_N T_\uparrow \to \Sigma_{\uparrow\uparrow}$, $G_N T_\downarrow \to \Sigma_{\uparrow\downarrow}$, and $G_N R_{\uparrow\downarrow} \to \tilde{R}_{\uparrow\downarrow}$. At first sight, there is a discrepancy, because $\Sigma_{\uparrow\uparrow}$ and $\Sigma_{\uparrow\downarrow}$ are the interface conductances while $T_s$ are the total transmission probabilities of the entire half-metallic electrode. However, these expressions are, in fact, consistent, because $\tilde{r}_F$ is invariant with respect to the choice of the boundary of the interface region at which the chemical potential $\zeta_F$ is evaluated. In order to see this, let us rewrite Eqs. 4.13-4.14 for the same F-N junction with a different choice of this boundary and denote the new chemical potential (at that boundary) by $\zeta_0^F$. This can be viewed as a simple redefinition of the thickness of the interface region. The chemical potentials on the normal side of the interface, however, are evaluated at the same point. The conductance and reflectance parameters corresponding to the new choice of $\zeta_0^F$ will be denoted $\Sigma^0_{\uparrow\uparrow}$, $\Sigma^0_{\uparrow\downarrow}$, and $\tilde{R}^0_{\uparrow\downarrow}$.

For a half-metallic electrode the spin polarization of the current injected into the N region under the condition $\zeta^N_\uparrow = \zeta^N_\downarrow$ is determined by the ratio $\alpha = \Sigma_{\uparrow\downarrow}/\Sigma_{\uparrow\uparrow}$, which should depend only on temperature. Therefore, $\Sigma_{\uparrow\downarrow}/\Sigma_{\uparrow\uparrow} = \Sigma^0_{\uparrow\downarrow}/\Sigma^0_{\uparrow\uparrow}$. The charge current is

$$j = \Sigma_{\uparrow\uparrow}(\xi_\uparrow + \alpha\xi_\downarrow) = \Sigma_F \Delta\zeta_F \tag{4.16}$$

where we denoted $\xi_s = \zeta^N_s - \zeta^F$ and $\Delta\zeta_F = \zeta^F - \zeta^F_0$, and $\Sigma_F$ is the conductance of the half-metallic region between the points where $\zeta^F$ and $\zeta^F_0$ are evaluated.

Equating the two different expressions for the same spin-dependent currents Eqs. 4.13-

4.14, we can write

$$(\Sigma^0 - \Sigma)\xi_\uparrow + \Sigma^0 \Delta\zeta_F + (\tilde{R}^0 - \tilde{R})(\xi_\uparrow - \xi_\downarrow) = 0 \tag{4.17}$$

$$\alpha(\Sigma^0 - \Sigma)\xi_\downarrow + \alpha\Sigma^0 \Delta\zeta_F - (\tilde{R}^0 - \tilde{R})(\xi_\uparrow - \xi_\downarrow) = 0 \tag{4.18}$$

where we simplified the notation by dropping indices: $\Sigma = \Sigma_{\uparrow\uparrow}$, $\tilde{R} = \tilde{R}_{\uparrow\downarrow}$, and similarly for $\Sigma^0$ and $\tilde{R}^0$. Furthermore, substituting $\Delta\zeta_F$ from Eq. 4.16, we obtain a system of two linear homogeneous equations for $\xi_\uparrow$ and $\xi_\downarrow$. For this system to have a solution, the determinant of the coefficient matrix should vanish, which leads to

$$\frac{\alpha}{1+\alpha}(\Sigma^0 - \Sigma) + \tilde{R}_0 - \tilde{R} = 0. \tag{4.19}$$

This expression implies that $\tilde{r}_F$ defined in Eq. 4.15 does not depend on the definition of the boundary of the interface region on the half-metallic side. Physically, this property follows from the unitarity of the scattering matrix and can not be satisfied without introducing the spin-flip reflection terms in Eqs. 4.13-4.14.

Spin injection from a half-metallic electrode may be schematically represented by the equivalent resistor circuit shown in Fig. 4.1. The resistances are defined as $r_{\uparrow\downarrow} = 1/\tilde{R}_{\uparrow\downarrow}$, $r_\uparrow = 1/\Sigma_{\uparrow\uparrow}$, and $r_\downarrow = 1/\Sigma_{\uparrow\downarrow}$. Interestingly, the effective resistance $4\tilde{r}_F$ in Eq. 4.15 can measured between the terminals of $r_{\uparrow\downarrow}$ if the N part of the circuit is disconnecting and the left terminal is left open. $P_\Sigma$ is given by $(r_\downarrow - r_\uparrow)/(r_\downarrow + r_\uparrow)$. The physical location of the left terminal of the circuit can be selected anywhere inside the half-metal. According to the arguments presented above, the change of this location redefines the three resistances $r_\uparrow$, $r_\downarrow$, $r_{\uparrow\downarrow}$ while leaving $r_\uparrow/r_\downarrow \sim \alpha$, $\tilde{r}_F$, and $P_j$ invariant. Note that the degradation of magnetic order at the interface may significantly affect $P_\Sigma$ and $\tilde{r}_F$.

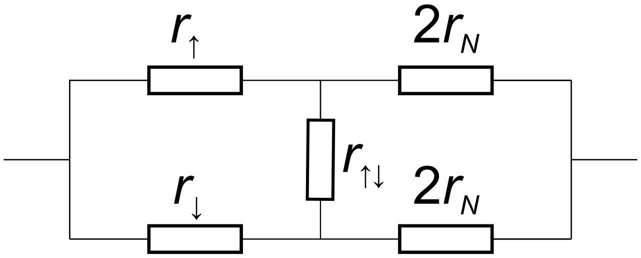

Figure 4.1: Equivalent resistor circuit for spin injection from a half-metal.

## 4.5 Spin injection efficiency for a half-metallic electrode

The conductance and reflectance parameters defined in Eq. 4.13-4.14 depend only on the properties of the interface region and not on the properties of the bulk half-metallic region attached to it. Therefore, the spin injection efficiency does not depend on the thickness of the half-metallic electrode. This result is valid as long as the half-metallic region is not so thin as to violate the assumptions of the diffusion theory. In practice this means that it should be thick compared to the electronic mean-free path.

Using this property, we can formally include an arbitrarily thick half-metallic layer in the definition of the interfacial region, so that the conductances $\Sigma_{\uparrow\uparrow}$, $\Sigma_{\uparrow\downarrow}$ are made very small (and thus the resistances $r_\uparrow$ and $r_\downarrow$ in Fig. 4.1 very large). Then the first term in the right-hand side of Eq. 4.15 is negligible compared to the corresponding asymptotic value $\tilde{R}^\infty_{\uparrow\downarrow}$, which is always finite at finite temperature. Thus, efficient spin-injection is possible only when $\tilde{R}^\infty_{\uparrow\downarrow} \lesssim r_N^{-1}$. In other words, spin injection is suppressed at $r_N \gg (\tilde{R}^\infty_{\uparrow\downarrow})^{-1} = r^\infty_{\uparrow\downarrow}$. On one hand, this condition is similar to the conductivity mismatch, because it sets a certain limit for $r_N$. On the other hand, the physical picture is quite different, because this limit is not related to the conductivity of the half-metal.

For generality let us allow for the existence of a magnetically unpolarized resistive barrier (such as a tunnel junction) at the interface, and let $T_c$ denote the transmission probability across this barrier. From the first term in Eq. 4.15 we can deduce $\tilde{r}_F \sim (\alpha G_N T_c)^{-1}$. Alternatively, we can find $\tilde{R}^{\infty}_{\uparrow\downarrow}$ by adding a large resistor on the left of $T_c$ with transmission probability $T_F \ll T_c$. In order to reflect with a spin-flip, an electron incident from the N side must first tunnel across the barrier in order to reach the spin-disordered region; this gives a factor $T_c$. Since we require $T_F/T_c \to 0$, the electron is reinjected back into the N region with probability 1. The probability of spin flip adds a factor $\alpha$, so we obtain $\tilde{R}^{\infty}_{\uparrow\downarrow} \sim \alpha G_N T_c$ and confirm the above result for $\tilde{r}_F$. An electron can also scatter with a spin flip on the transverse exchange field introduced by the spin density penetrating across the barrier. This mechanism contributes in the same order to $\tilde{R}^{\infty}_{\uparrow\downarrow}$.

In the ohmic regime (low-resistance interface with $T_c \sim 1$), we have $G_N\tilde{r}_F \sim 1/\alpha$. Since $G_N r_N \sim l^N_{sf}/l$, where $l$ is the mean-free path in the normal metal, we find that spin disorder suppresses spin injection when $\alpha \gg l/l^N_{sf}$. At small $T$ we expect $\alpha \approx \langle\theta^2\rangle/4$, where $\theta$ is the polar angle of the injected spinor. The parameter $\alpha$ is approximately related to the reduced magnetization $m = M(T)/M(0)$ of the half-metal as $2\alpha \approx 1-m$. (This quantity is proportional to the partial minority-spin DOS in the global spin basis.) Thus, the above condition shows the range of temperatures for which ohmic spin injection from a half-metal may be possible.

It is interesting to compare this result with the case of a two-channel ferromagnet with the same spin polarization of DOS, for which the efficiency of ohmic spin injection is given by Eq. 4.1 with $r_c = 0$. Setting $\rho_\downarrow \sim \rho_\uparrow/\alpha$, we find $r_F \sim \rho_\uparrow l^F_{sf}/\alpha$, which should be compared to $\tilde{r}_F \sim \rho_N l/\alpha$ in the case of a half-metallic electrode. The dependence on the spin polarization of the globally defined DOS is similar, but the overall factor is different: the product $\rho_\uparrow l_{sf}^F$ is replaced by $\rho_N l$ in the case of a half-metal. For spin injection in semiconductors from metals, typically $\rho_N \gg \rho_\uparrow$, while $l_{sf}^F$ is usually fairly small [167]. Thus, the effective resistance of a half-metallic electrode may be much larger compared to a conventional ferromagnet with a similar spin polarization of the DOS, which is an advantage for practical applications. On the other hand, since $\tilde{r}_F$ does not depend on the resistivity of the half-metal, there is no benefit in increasing this resistivity. In particular, a magnetic semiconductor should not necessarily be a better spin injector than a highly conductive half-metal, assuming that half-metallicity is maintained at the interface in both cases.

For an actual device (e. g. F/N/F) it is necessary that $l_{sf}^N$ is not small compared to the length $L$ of the channel, and $l/l_{sf}^N$ should be replaced by $l/L$ if $l_{sf}^N \gg L$. Thus, for ohmic spin injection from a half-metal it may be beneficial to use a lightly doped semiconducting channel in order to maximize the mean-free path there. This is contrary to the conventional conductance mismatch considerations, according to which it is desirable to decrease $\rho_N$ by increasing the doping concentration. The mean-free path in lightly doped silicon may be as high as 30 nm at room temperature [170]. For a short channel with $L \sim 300$ nm this would allow ohmic spin injection at $\alpha \lesssim 0.1$. Although this is an order-of-magnitude estimate, at face value it allows spin injection for $M(T)/M(0) \gtrsim 0.8$. In elemental transition metals the reduced magnetization drops to 0.8 at about 75% of the Curie temperature, so this limitation is not very restrictive, particularly since the half-metallic gap may be closed by magnetic disorder at much lower temperatures [122]. A similar estimate applies to nonlocal spin valves with a copper channel, where at room temperature the mean-free path is on the order of 30 nm, and the spin-diffusion length is a few hundred nanometers [167]. It is possible that efficient spin injection across a transparent interface observed in Ref. [159] can be understood in a similar way.

From the point of view of interface engineering, it is always necessary to avoid the depletion region near the surface [147]. On the other hand, we would like to point out that in the ohmic regime the existence of interface states in the “wrong” spin channel does not necessarily preclude spin injection, as it would with a tunnel barrier. If these states are strongly hybridized with the normal region, they can be regarded as a part of the corresponding spin channel. (See Ref. [171] for a related discussion.) It is, however, important that the magnetic continuity and ordering at the interface is maintained. Otherwise, partially ordered regions or “loose spins” can provide strong spin-flip scattering at relatively low temperatures, thereby violating the $\alpha \lesssim l/l_{sf}^N$ inequality and suppressing spin injection. Thus, interface design based on chemical similarity of the F and N regions [172] may in practice be counterproductive, because it may be expected to facilitate interdiffusion.

With a tunnel barrier at the interface, the temperature range allowing efficient spin injection extends to $\alpha \lesssim (l/l_{sf}^N)/T_c$. As in the case of a conventional ferromagnetic electrode, the tunnel barrier is favorable for spin injection. In the case $T_c \ll l/l_{sf}^N$ spin injection is possible at any temperature, and its efficiency is proportional to $P_t = (1-\alpha)/(1+\alpha)$. (Of course, this assumes that the half-metal continues to behave as a single-channel conductor at elevated temperatures; real materials with a small half-metallic gap do not necessarily behave in this way.)

## 4.6 Tight-binding calculations

In this section we verify the conclusions of the general theory using tight-binding calculations for a specific realization of a half-metal based on the *s*-*d* model. Static spin disorder is introduced by randomizing the directions of the exchange fields on different sites according to the mean-field distribution function corresponding to the

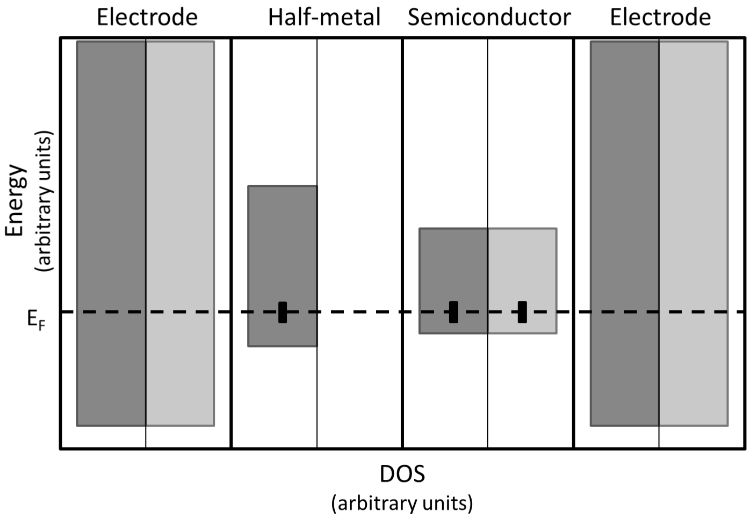

Figure 4.2: Schematic picture of the band alignment for the spin injection device without spin disorder. Darker and lighter bands correspond to majority and minority spins. The minority-spin band in the half-metallic region is shifted up beyond the energy range shown in the figure. The horizontal dashed line shows the Fermi level, and the vertical black bars show the amplitude of random disorder.

specified value of the magnetization. The spin injection device is treated as an elastic system. We use a single-band Hamiltonian with nearest-neighbor interactions in the simple cubic lattice, and

$$H^\sigma = E_s^\sigma - \beta^\sigma - 2\gamma_h\left[\cos(k_x a) + \cos(k_y a) + \cos(k_z a)\right] \tag{4.20}$$

where $E_s^\sigma - \beta^\sigma$ is the band center of spin $\sigma$ and $\gamma_h$ is the spin-independent hopping parameter. See Appendix 4.A for details on using the existing LMTO software (used in Chapters 5 & 6) to simulate Eq. 4.20. For the half-metallic region, the energies in one spin channel are made very large in order to lift it far above the Fermi level. This is the limit of a large *s*-*d* exchange integral. The half-metallic and normal regions are sandwiched between two non-magnetic leads. The hopping and band center parameters are selected as shown schematically in Fig. 4.2. Calculations were performed for

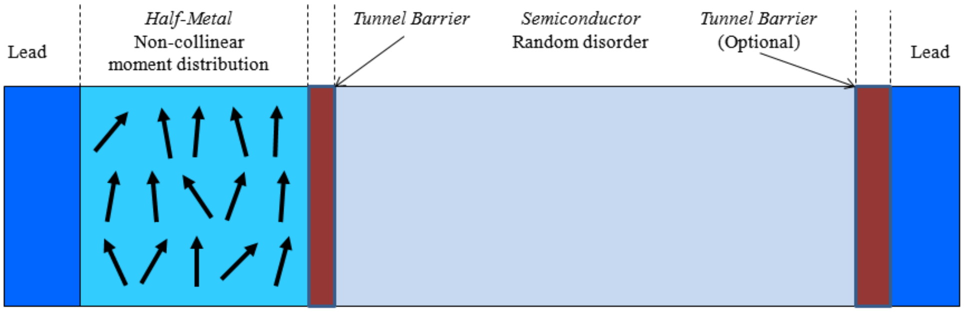

Figure 4.3: A schematic of the supercells used to calculate transport. A tunnel barrier one monolayer in length may be inserted in-between the magnetic and normal regions. The second tunnel barrier on the right is used to simulate large resistances, if needed.

supercells, as shown in Fig. 4.3, with a 10 × 10 cross-section. The 2 × 2 conductance matrix $G_{ss'}$ was obtained using the Landauer-Büttiker approach, averaging over 100 configurations of spin and Anderson[2] (random) disorder. Brillouin zone integration was performed using a 5 × 5 mesh, which was sufficient for convergence. To simulate diffusive transport, random disorder was applied to both half-metallic and semiconductor (normal) regions. Fig. 4.2 illustrates the relative amplitude of random disorder relative to the band widths.

Since the spin current in the normal region is conserved, the spin polarization of the current flowing into the right electrode is identified with the spin injection efficiency:

$$P_G = \frac{G_{\uparrow\uparrow} + G_{\downarrow\uparrow} - G_{\uparrow\downarrow} - G_{\downarrow\downarrow}}{G_{\uparrow\uparrow} + G_{\downarrow\uparrow} + G_{\uparrow\downarrow} + G_{\downarrow\downarrow}}. \tag{4.21}$$

According to the results of the previous sections, the dependence of $P_G$ on the total resistance of the normal layer reflects the dependence of spin injection efficiency on the effective resistance $r_N$.

---

[2] Anderson disorder is applied as a rigid shift of the band centers of individual sites according to a random distribution

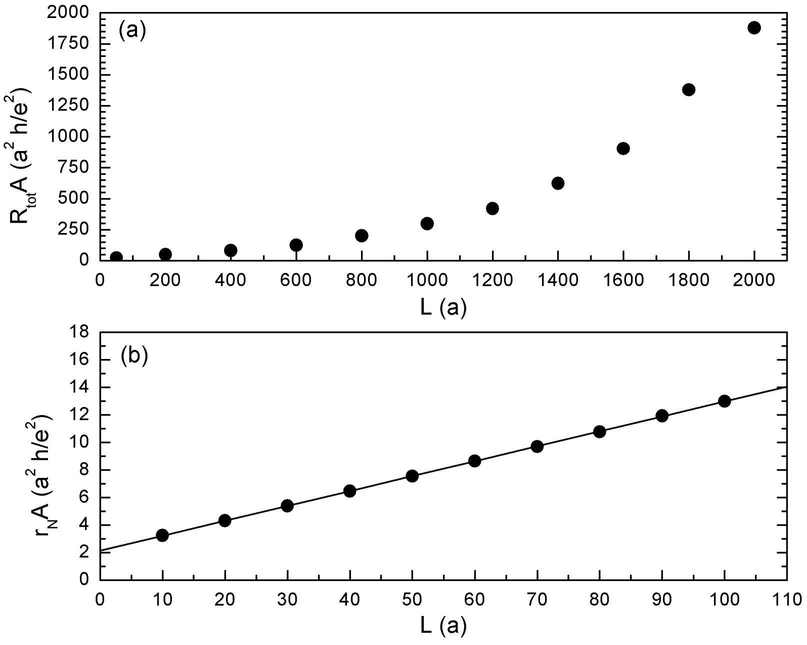

Figure 4.4: (a) The total area-resistance product of a half-metal/semiconductor system with fixed magnetization $m = 0.90$ as a function of the length of the disordered normal region with disorder amplitude $\Delta_{\text{And}} = 1.0$ eV. Note the exponential increase of $R_{\text{tot}}A$, indicating the onset of localization effects. (b) The area-resistance product of the normal region only as a function of the length of the disorder with amplitude $\Delta_{\text{And}} = 1.0$ eV.

In the following we verify the following properties of the spin injection efficiency $P_G$ for a half-metallic electrode: (1) Independence of $P_G$ on the thickness of the half-metal; (2) The form in Eq. 4.11 of the dependence of $P_G$ on the resistance of the normal region; (3) Dependence of $\tilde{r}_F$ on the magnetization of the half-metal, $\tilde{r}_F \sim \alpha^{-1}$; (4) Dependence of $\tilde{r}_F$ on the transparency of a thin tunnel barrier inserted at the interface, $\tilde{r}_F \sim T_c^{-1}$.

The inset of Fig. 4.6(a) shows $P_G$ as a function of the thickness of the half-metallic region at $m = M/M(0) = 0.9$, with a 50-monolayer thick normal region. It is seen that $P_G$ is independent of the thickness of the half-metal, in agreement with the general results. In all subsequent calculations the thickness of the half-metal is fixed

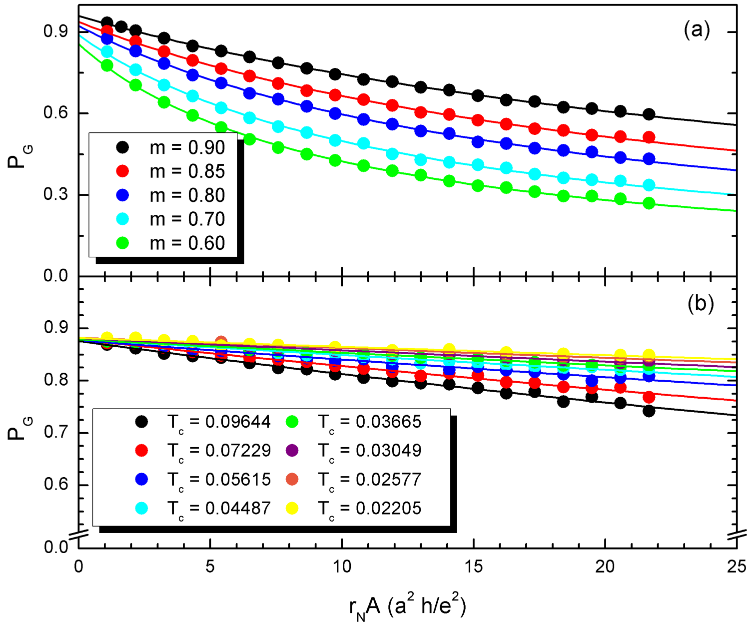

Figure 4.5: The polarization of the half-metal/semiconductor system as a function of the area-resistance product $r_N A$ of the normal region. The points represent calculations and the solid lines are fits to Eq. 4.11. (a) Calculations of $P_G(r_N A)$ for different fixed magnetizations as indicated in the legend. (b) Calculations of $P_G(r_N A)$ for a system with a monolayer tunnel barrier of variable height inserted in-between the half-metal and normal region. The tunnel barrier transmission probabilities $T_c$ are in the legend.

at 5 monolayers.

In order to obtain the asymptotic dependence of $P_G$ on the resistance of the normal region, we have added a tunnel barrier of variable height and thickness between the semiconductor and the right lead as indicated in Fig. 4.3. If the second tunnel barrier is omitted and the length of the normal region varied instead, then as indicated by Fig. 4.4(a), diffusive scaling breaks down for large thicknesses. This is because of localization effects that become important when the disordered normal region is made too long.[3] [173] As such, the length of the normal region is fixed at 50 monolayers.

---

[3] This leads to problems if one attempts to calculate the polarization as a function of the thickness of the normal region. Because of localization effects, the polarization will not trend to zero at large thicknesses (large $r_N$) and appear to indicate efficient spin injection, which is incorrect. The

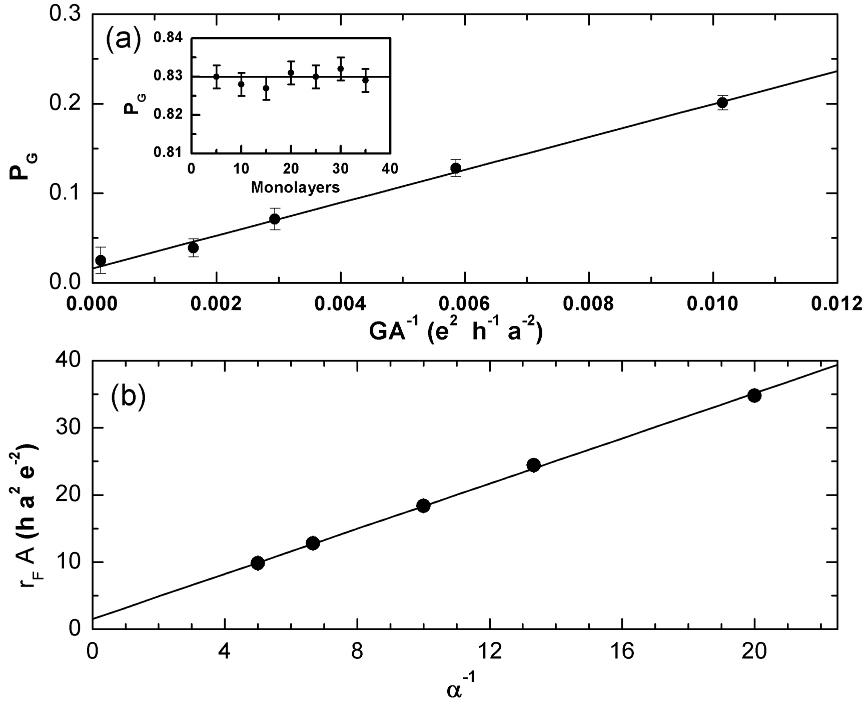

Figure 4.6: (a) Conductance polarization as a function of the inverse resistance-area product for the reduced magnetization $m = 0.8$. Inset: Same quantity as a function of the thickness of the half-metal at $m = 0.9$. (b) Effective resistance $\tilde{r}_F$ as a function of $\alpha^{-1}$, where $\alpha = (1 - m)/2$.

Fig. 4.6(a) shows the dependence of $P_G$ on the total resistance of the scattering region (which is dominated by the auxiliary tunnel barrier) for the reduced magnetization of $m = M/M(0) = 0.8$. It is clearly seen that $P_G$ goes to zero linearly with $r_N^{-1}$, in agreement with Eq. 4.11.

Next we evaluate the dependence of the effective resistance $\tilde{r}_F$ on the magnetization $m$ of the half-metal. To this end, for a given $m$ the $P_G$ is calculated from the configurationally averaged spin-dependence conductances for a set of thicknesses of the normal region ranging from 10 to 200 monolayers (all within the range where weak localization effects are undetectable). The fit in Fig. 4.4(b) was used to deter-

---

localization effects cannot be viewed as just adding resistance to the system, since diffusive transport is no longer valid.

mine $r_N$ for each thickness of the normal region. The results of these calculations are shown in Fig. 4.5(a). The $P_G(r_N)$ dependence is then fitted to Eq. 4.11 for each $m$. The magnitude of $P_t$ decreases with decreasing magnetization but always remains somewhat larger than $m$. (This is likely due to the fact that the conduction electrons sample spin disorder over a few sites, effectively decreasing the transverse fields.) The dependence of $\tilde{r}_F$ on the magnetization is shown in Fig. 4.6(b), where $\alpha = (1-m)/2$, as above. Linear dependence $\tilde{r}_F \propto \alpha^{-1}$ confirms the predictions of the general model, in which $\tilde{r}_F \propto R_{\uparrow\downarrow}^{-1} \sim \alpha^{-1}$. This divergence of $\tilde{r}_F$ at low temperatures may be used experimentally as a signature of a true single-channel half-metal, although at very low temperatures the interfacial spin-orbit scattering may take over and cut off the divergence.

Finally, we considered the effect of a single-monolayer tunnel barrier at the F/N interface. We set $m = 0.6$ for the half-metal and varied the thickness of the semiconductor region from 10 to 200 monolayers, as above. As above, $P_G$ calculated from the averaged spin-dependent conductances, shown in Fig. 4.5(b), was fitted to Eq. 4.11, extracting the $\tilde{r}_F(T_c)$ dependence. $T_c$ was varied by changing the height of the tunnel barrier, with the selected transmission probabilities indicated in the legend in Fig. 4.5(b). Fig. 4.7 shows the results supporting the inverse relationship $\tilde{r}_F \propto T_c^{-1}$. Together with the results shown in Fig. 4.6, we find $\tilde{r}_F \propto (\alpha T_c)^{-1}$, as expected.

## 4.7 Conclusions

We have analyzed the spin injection from a half-metallic electrode into a normal (or semiconducting) region in the presence of thermal spin disorder. The two-current model with independent populations of the two spin channels is inapplicable to a half-metallic ferromagnet. The spin injection efficiency is described by Eq. 4.11, in

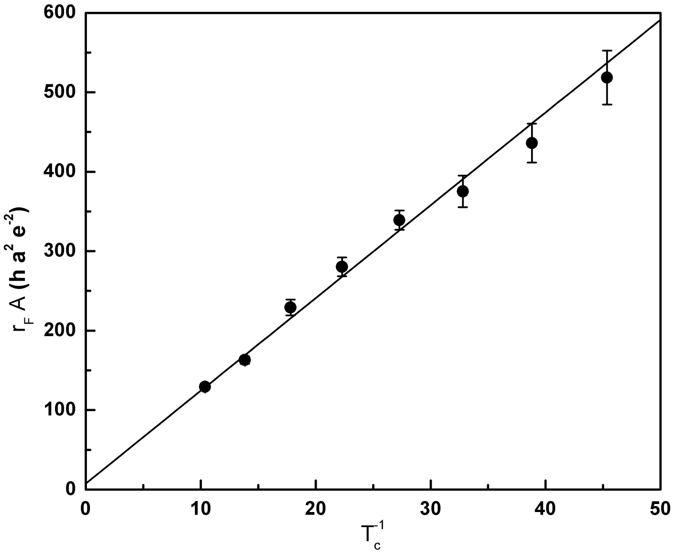

Figure 4.7: Effective resistance $\tilde{r}_F$ as a function of $T_c^{-1}$ for fixed magnetization $m = 0.6$.

which $r_N$ is the conventional effective resistance of the normal metal, while $\tilde{r}_F$ is controlled by spin-flip scattering at the interface with the ferromagnet. Although $\tilde{r}_F$ does not depend on the thickness of the half-metallic layer, its dependence on the spin polarization of the density of states and on the contact resistance is similar to the case of a conventional ferromagnet. Explicit simulations for the tight-binding *s*-*d* model confirm these general conclusions. In the case of a transparent interface, efficient spin injection is possible in the temperature range corresponding to $\alpha \lesssim l/l_{sf}^N$, where $\alpha$ is the relative deviation of the (surface) magnetization from saturation, and $l$ is the mean-free path in the N region. A rough estimates suggests that efficient spin injection from half-metallic Co-based Heusler alloys into silicon or copper may be possible at room temperature across a transparent interface. Adding a tunnel barrier at the interface with transparency $T_c$ extends this temperature range to $\alpha \lesssim l/l_{sf}^N T_c^{-1}$.

## 4.A Implementing tight-binding calculations in LMTO

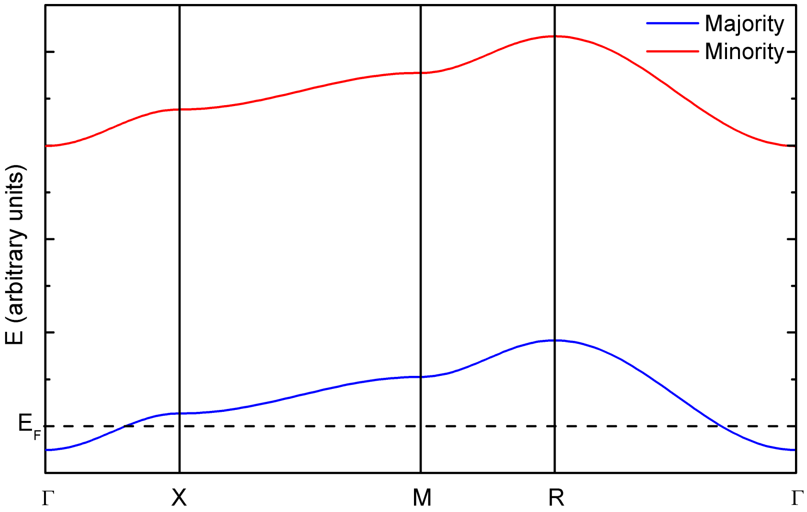

Figure 4.8: An example of a spin-polarized band structure for the nearest-neighbor single-band tight-binding model generated by modifying the LMTO program. The band structure is non-magnetic if the spin-up and spin-down band centers are equal.

Transport calculations using the tight-binding Hamiltonian in Eq. 4.20 were done using the LMTO package maintained by Mark van Schilfgaarde. This required small modifications to the code which are easy to implement. Although this was done in the now out-of-date v6.17 of the code, it is straightforward to port these instructions to later releases.

The orthogonal LMTO Hamiltonian in Eq. 2.70 may be transformed into a different representation in the following way [105]:

$$H^{\mathrm{orth}} = C + \sqrt{\Delta} S^{\alpha} \left[1 + (\alpha - \gamma) S^{\alpha}\right]^{-1} \sqrt{\Delta} \tag{4.22}$$

where $\alpha$ is the chosen screening constant. For a single band Hamiltonian with only nearest-neighbor interactions, choosing the tight-binding screening constant $\alpha = 0.2143$ for the $\ell = 0$ ($s$-like) orbital [105] and setting $\gamma = \alpha$ reduces Eq. 4.22 to Eq. 4.20, with $C$ taking the place of $E_s - \beta$ and $\Delta$ taking the place of $\gamma_h$. The band structure for a particular choice of parameters can be found in Fig. 4.8.

To implement this into the LMTO program, the potential and screening parameters for each atomic sphere must be frozen so that they can be tuned to suit one's needs. In lm-6.17/subs/atomsr.f, comment out lines 1832-1835,

```
C   pp(2,l,i) = e - (phi/phip)*wk/wkdot
C   pp(3,l,i) = -dsqrt(sdivw/2/rmax)/phip/wkdot*scl
C   pp(5,l,i) = sdivw*wjdot/wkdot
C   pp(6,l,i) = pp(5,l,i)
```

In the ctrl file, set GAMMA=0 and TWOC=T to turn off the gamma representation and use the two-center Hamiltonian. When using the Green's function code, use 2nd order potential parameters with GFOPTS=p2. Use a simple cubic structure and set RMAX to only include nearest neighbors when calculating the structure constant. Under the STRUC category, set NL=1 to use only one orbital. For the atomic species, use empty spheres (Z=0).

In the atomic file, set $\gamma = \alpha = 0.2143$, zero out e_nu and 1/sqrt(p) (this should be automatic because of TWOC=T and GFOPTS=p2), then choose C and +/-del to set the band center and hopping parameter. The following is an example of how to set the potential parameters in an atomic file,

```
l        e_nu            C            +/-del        1/sqrt(p)        gam
alp
0   0.00000000   0.17500000   0.11500000    0.0000000   0.21430000
0.21430000
```

```
0  0.00000000  3.42500000  0.11500000   0.0000000  0.21430000
0.21430000
```

If the C parameters in the top and bottom rows (for majority and minority spin) are the same, then the potential is non-magnetic, and if they are different, then the potential is magnetic. To simulate a system with an interface (or multiple interfaces), construct a supercell that is divided up into different regions with different settings for the band centers and hopping parameter.

The above is sufficient to perform empirical tight-binding calculations and can be used with the transport code to calculate the conductance of a model system. It is worth noting that since the system has no charge (because of the empty spheres), it is a waste of computational time to calculate the Madelung matrix for transport since it will be zero. For small systems this is not expensive, but if large supercells are used such as the $10 \times 10$ lateral cells in Sec. 4.6, then transport calculations will hang for some time while the Madelung matrix is generated. Therefore, it is advised to suppress all calls to generate and use the Madelung matrix in the following subroutines: lm-6.17/subs/aioxtn.f, lm-6.17/subs/asalsq.f, lm-6.17/subs/asamad.f, lm-6.17/subs/lmasa.f, lm-6.17/subs/supot.f, lm-6.17/pgf/lmasa-gf.f.

## Chapter 5

# Calculations of spin-disorder resistivity of heavy rare-earth metals: Gd-Tm series

## 5.1 Introduction

Scattering on spin fluctuations in magnetic metals adds an “anomalous” contribution to the electrical resistivity [13, 59, 60]. Contrary to other scattering mechanisms, such as impurity and phonon ones, this spin-disorder scattering is not well understood, because the theory of spin fluctuations at elevated temperatures is far from being complete [107]. The minimal model of spin-disorder resistivity (SDR) is based on the $s$-$d$ (or $d$-$f$) Hamiltonian, containing on-site interaction of the conduction electrons with spins localized on lattice sites, which are subject to thermal fluctuations [61, 174, 175]. This interaction is also responsible for the indirect exchange coupling described by the RKKY theory [57, 58]. Extensions of this model to include Fermi surface anisotropy and the appearance of “superzones” (in the helically ordered state) in the heavy rare-earths have also been proposed [57, 58, 70, 176–178].

First-principles calculations of SDR provide an opportunity to test the models of spin disorder quantitatively by comparing the predicted SDR with experiment. In particular, such a study of spin-disorder resistivity of Fe and Ni [179] suggests that the spin fluctuations in these materials are described reasonably well by slowly rotating, classical local magnetic moments, supporting the widely used “adiabatic” model of spin fluctuations [116].

The series of heavy rare-earth metals (Gd-Tm) provides an interesting case study, because the $4f$ electrons supplying most of the local moment are much more localized compared to the transition metals, while the orbitals moments are not quenched. It may therefore be expected that treatment of spin fluctuations in rare-earth materials as classical spin rotations may be inadequate. Systematic experimental studies of the electrical properties of heavy rare earths were carried out by Legvold *et al.* These included polycrystalline [6, 180] and single-crystal samples [7–12], allowing a compilation of the SDR in the in-plane and $c$-axis directions of the hexagonal crystal structure. Single-crystal resistivity measurements have also been performed by other group [64–68].

In the $f$-$d$ model picture, the assumption that the $4f$ local moment can be treated as a quantum multiplet with a fixed angular momentum $J$ leads to the SDR being proportional to $J(J+1)$ in the paramagnetic state (in the Born approximation). The effective scattering potential is, however, provided largely by spin alone. Therefore, in this picture the SDR in the Gd-Tm series should behave as $S^2(J+1)/J$. This picture appears to agree reasonably well with experimental data [69, 70], but only after an empirical electronic correction is included [70].

The choice of the angular momentum $J$ for the quantum multiplet [69, 70] is based on the assumption that spin-orbit coupling is sufficiently strong to enforce the collinearity of $\mathbf{S}$ and $\mathbf{L}$ at all times. If spin-orbit coupling is small compared to other relevant energy scales, then the role of $J$ should be played by $S$ and SDR should behave as $S(S+1)$ in the Gd-Tm series. However, band structure calculations [181] show that the $4f$ bandwidth is comparable to or greater than the spin-orbit splittings of the localized $4f$ multiplets with different $J$ values, which are of the order of 0.1 eV. The local exchange potential acting on the conduction electrons by the fluctuating $4f$ moments is on the order of 1 eV in Gd and decreases linearly with the $4f$ spin moment later in the series. This fluctuating exchange potential should induce an uncertainty of the conduction electron energy on the order of a few tenths of an eV. Therefore, the assumption that the $J$ value of the fluctuating $4f$ shell should be conserved in the scattering process is not well justified. Since all the relevant energy scales (spin-orbit splittings, exchange splitting, bandwidth) are roughly of the same order of magnitude, the effect of spin and orbital momentum quantization on SDR may be quite complicated.

In this chapter we study the SDR for the Gd-Tm series using first-principles calculations based on density functional theory. We use two complementary approaches, one using supercell averaging of the Landauer-Büttiker conductance, and the other based on linear response calculations applied to the paramagnetic state described within the coherent potential approximation. In most calculations the $4f$ electrons are treated as fully localized, but the effect of including them in the valence basis is also considered. The results of our calculations represent the predictions of the classical spin model. Contrary to the case of transition metals [179], our results for Gd-Tm are systematically and significantly lower compared to experimental data, suggesting that the quantum character of the $4f$ shell is indeed important. However, we found that neither a $(J+1)/J$ nor an $(S+1)/S$ correction brings the results in close agreement with experiment, supporting the qualitative argument that the fluctuations of the $4f$ shell are not well described either by the fixed-$J$ model or by the assumption that **S** and **L** are weekly coupled.

## 5.2 Computational methods

The $4f$ electrons in rare earths are strongly localized and obey Hund's rules, producing large local magnetic moments. These electrons are not well described by the local density approximation [181], which places the $4f$ energy bands close to the Fermi level in disagreement with photoemission experiments [182]. This problem can be addressed in two ways. First, one can use the LDA+$U$ method for the $4f$ electrons, which introduces a correlation gap and removes the $4f$ states from the Fermi level. The second way is to treat the $4f$ orbitals as fully localized by excluding them from the valence basis and filling them in accordance with Hund's rules (the "open-core" approximation). In both cases the partially filled $4f$ states supply local moments and contribute to the scattering (exchange) potential. In the open-core approach they are explicitly prevented from carrying current; in the LDA+$U$ approach their contribution to the current is expected to be small, but they can still affect the scattering rates by modifying the final states. Both solutions produce similar band structures near the Fermi level [181], and therefore they can be expected to produce similar results for transport.

Our calculations of SDR are based on the tight-binding linear muffin-tin orbital (TB-LMTO) method [183]. In most of our calculations we used the open-core approximation [184] for the $4f$ states, but we have also considered the effect of including the $4f$ states in the valence basis. As expected, this inclusion increases the resistivity by a small amount.

We used two approaches for SDR calculations, the Landauer-Büttiker (LB) method and the linear response technique applied within the disordered local moment (DLM)

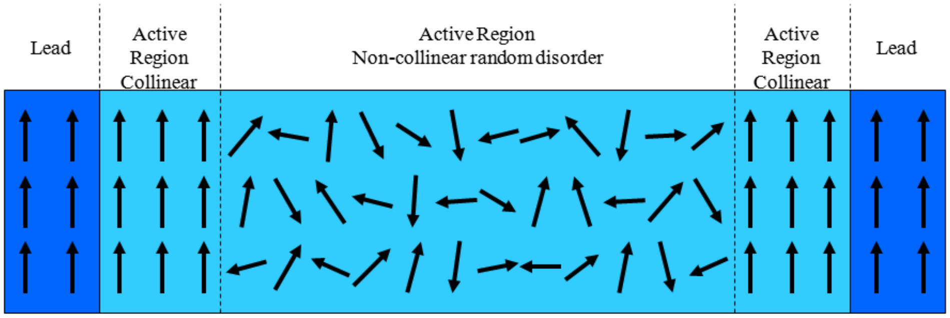

Figure 5.1: A schematic of the supercells used to calculate transport.

model. In all calculations we consider the paramagnetic state to be a completely random, uncorrelated distribution of local moment directions on different atomic sites. The results are compared with experimental data, from which the phonon and impurity contributions have been removed by an appropriate fitting.

While the LB approach can be used for more complicated spin statistics [179], the DLM method is, by design, appropriate only to uncorrelated spin disorder due to its reliance on the single-site approximation. The DLM method uses the bulk geometry and computes the resistivity by a reciprocal-space integration of the Kubo-Greenwood formula, while the LB approach requires the construction of supercells.

### 5.2.1 Landauer-Büttiker approach

The method used for SDR calculations was described in Ref. [179]. Supercells are constructed as in Fig. 5.1 and the potentials taken from self-consistent collinear calculations are frozen. Spin disorder is introduced by randomizing the moment directions by rotating the spin densities of the atomic spheres with reference to a global spin axis. The conductance is calculated using the principle-layer Green's function technique [105, 185] and the Landauer-Büttiker formalism [186], with an implementation that allows noncollinearity in the active region. Since the rotated potentials are not self-consistent, charge neutrality is ensured by applying an appropriate potential shift to the active region.

All heavy rare earth elements examined in this study (Gd, Tb, Dy, Ho, Er and Tm) have a hexagonal close-packed crystal structure. The resistivity tensor has two independent components for current flowing parallel and perpendicular to the hexagonal $c$ axis. For transport along the $c$ axis we used supercells with a $4\times4$ cross-section (16 atoms per monolayer, interlayer spacing $c/2$) of area $8a^2\sqrt{3}$. The in-plane SDR was calculated for the current flowing parallel to one of the in-plane lattice vectors. For this direction we used supercells with $3\times2$ (12 atoms per monolayer, interlayer spacing $a$) rectangular cross-section of width $3a\sqrt{3}$ and height $2c$. The integration of the conductance over the two-dimensional Brillouin zone is performed using a $24\times24$ $k$-point mesh for both transport directions, and the result is averaged over 15 random noncollinear spin distributions. For a convergence test see Appendix 5.A.

Fig. 5.2 shows the configurationally averaged area-resistance product $RA$ as a function of the thickness $L$ of the active disordered region in our supercell calculations for Gd, Tb and Tm for both transport directions. The plots for other three elements (Dy, Ho and Er) are similar. The ohmic regime is quickly reached for all elements. The SDR is obtained from the slope of the fit to the linear region.

To check the validity of the open-core approximation for transport calculations, we include the $4f$ orbitals in the valence basis set and calculate the self-consistent potentials using the fully localized limit of LDA+$U$ [187] applied to the $4f$ electrons. The population of the $4f$ states is specified manually by a diagonal density matrix in the spherical harmonic representation (which is not subject to self-consistency); the orbitals are filled according to Hund's rules. For Gd we used $U = 6.7$ eV and $J = 0.7$ eV. The band structure agrees with Ref. [181] with the unoccupied $4f$ states

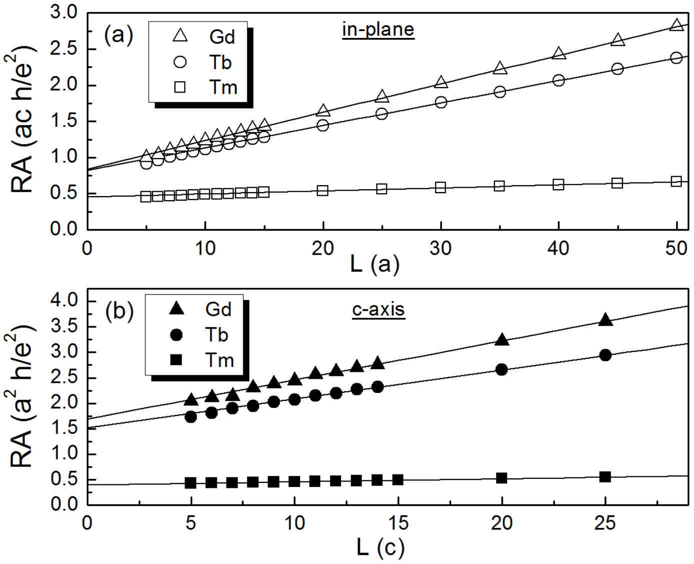

Figure 5.2: Area-resistance product $RA$ $vs$ the thickness $L$ of the disordered region for both transport directions for Gd, Tb and Tm (LB method). Each point corresponds to an average of 15 or more random spin-disorder configurations. (a) In-plane direction, open shapes, (b) $c-$axis direction, closed shapes. Triangles: Gd, Circles: Tb, Squares: Tm.

located 2 eV above the Fermi energy. For Ho we fixed $J = 0.7$ eV and adjusted the $U$ parameter to $U = 8.0$ eV to place the minority-spin $4f$ bands at 2 eV above the Fermi level, according to the photoemission data [182]. For transport calculation we then use the (less expensive) Ising approximation by randomly assigning “up” and “down” directions for the local moments. (This approximation is justified by good agreement with DLM results in all other cases.) The orbital occupations are also adjusted so that the orbital moments are parallel to spin moments on all sites.

### 5.2.2 Disordered local moment (DLM) model

The DLM approach [116] describes the paramagnetic state above the Curie point, approximating it as an ensemble of randomly oriented local magnetic moments. The electronic structure of this state is evaluated self-consistently using the coherent potential approximation (CPA). The solution for the spherically symmetric vector model is conveniently equivalent to that for the fictitious equiconcentrational binary alloy, whose two components represent atoms with antiparallel local moments. The spin-disorder part of the total resistivity can then be associated with the "residual" resistivity of the DLM state viewed as a binary alloy, which is calculated within the Kubo-Greenwood approach [188]. The first implementation of the DLM method for resistivity studies was done in Ref. [189]. Our implementation of the linear response technique within the TB-LMTO-CPA method including disorder-induced vertex corrections is described in Refs. [190] & [191].

As a test case we calculated the SDR for bcc iron using the DLM method and the *spd* basis. The resistivity is 85 $\mu\Omega$ cm, which agrees well both with supercell LB calculations [179] and with experiment, while the value obtained in Ref. [189] is almost twice larger. The origin of this disagreement is unclear. The method of Ref. [189] utilizes a hybrid method where the electronic structure is described by DLM method, but the resistivity is found from the slope in the multilayer geometry as a limit from large imaginary parts of the energy (1 and 2 mRy). This method also neglects vertex corrections, thus violating current conservation.

## 5.3 Review of experimental data

The experimental data in Table 5.1 are those of Legvold and coworkers [6–12] and those of other groups [64, 66–68]. The former set of SDR values for Gd, Tb, Dy, Ho and Er are taken from the compilation plot in Ref. [70] and agree well with our own fits to the single-crystal resistivity data. The in-plane and *c*-axis SDRs for Tm are explicitly reported in Ref. [12], as are the single-crystal data for Gd by Maezawa *et al.* [66] and for Er [68] and Tm [67] by Ellerby *et al.* The additional values for Dy are obtained from the plots of Ref. [64] by an appropriate fitting.

For Gd and Dy the resistivity curves and SDR values reported by different references agree quite well. For Er and Tm the resistivity curves from different measurements are similar in shape and indicate the same transition temperatures, but the absolute values of the residual-subtracted resistivities differ. For Er, the residual-subtracted resistivities reported by Ellerby *et al.* are systematically larger compared to the results of Legvold *et al.* For example, the resistivity at the Néel temperature $T_N = 85$ K is about 6 $\mu\Omega$ cm larger in the $c$-axis direction and about 19 $\mu\Omega$ cm larger in the in-plane direction. The SDRs do not agree either, with SDRs from Ellerby *et al.* being a factor of 1.4 to 1.5 larger. For Tm the disagreement is in the opposite direction; Ellerby *et al.* note that their $c$-axis (in-plane) resistivity curves are a factor of 2 (factor of 1.3) smaller compared to Legvold *et al.* The SDRs in the two studies, however, are in agreement.

The source of these disagreements is currently unknown. Ellerby *et al.* mentioned [67] that the discrepancy might be due to errors in determining the cross-sectional areas of the samples. Another problem may be the purity of the samples. The residual resistivities reported by Legvold *et al.* for Er are rather large and of the same order as the SDRs. In the rest of the heavy rare-earth experiments by Legvold *et al.* the residual resistivities are between 3 and 6 $\mu\Omega$ cm. These discrepancies introduce some ambiguity, at least in the case of Er, when comparing the calculated SDR with experiment.

## 5.4 Results

For each element and transport direction we performed two sets of calculations corresponding to different atomic potentials. The first set of calculations used self-consistent potentials from the collinear ferromagnetic ground state of each metal. These results are listed in the first row for each element in Table 5.1. The second set used potentials with reduced local moments taken from the self-consistent DLM calculations for the paramagnetic state. These results are listed in the second row for each element. To compare the effect of local moment reduction in both methods, the atomic potentials are calculated self-consistently in the presence of an appropriately adjusted external field, constraining the local moments to their DLM values. These atomic potentials are then used in LB calculations. We refer to these as the fixed-spin moment (FSM) calculations.

In order to compare the band structure obtained using the DLM method with explicit supercell calculations (to which DLM is an approximation), we constructed 64-atom supercells for Gd (4 hexagonal monolayers with 16 atoms per monolayer, periodically repeated in three dimensions). We used FSM potentials as input and generated 7 different spin disorder configurations by randomly assigning the directions of all local moments in the supercell. Then the partial density of states (DOS) for each site was calculated in the local reference frame ($z$ axis collinear with local moment direction) and then averaged over all sites and all 7 configurations. At the same time the output local moments were also calculated and averaged. This average output moment was $7.46\mu_B$ with a standard deviation of of $0.03\mu_B$, comparing well with the input moment of $7.44\mu_B$. The averaged local DOS shown in Fig. 5.3 is almost indistinguishable from the self-consistent DLM result of Ref. [1]. This agreement shows that the DLM method provides an accurate description of the band structure of rare-earth metals. This agreement extends to transport calculations, as discussed below.

Table 5.1 lists the SDR results obtained using both LB and DLM methods. SDR

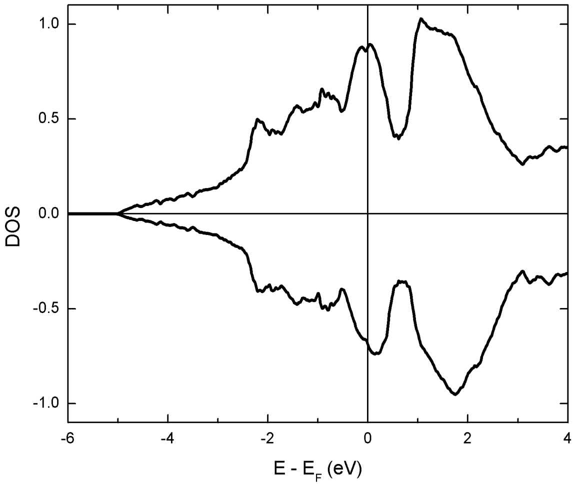

Figure 5.3: Spin-projected local DOS of paramagnetic Gd averaged over 64-atom supercells with random noncollinear local moment orientations. The valence basis includes $s$, $p$, and $d$ states, while the fully spin-polarized $4f$ shell is included in the open-core approximation. The total (input) local moment is $7.44\mu_B$. (Note excellent agreement with the DLM result of Ref. [1].)

for a polycrystal was estimated using the empirical formula [192]

$$\rho_{\text{poly}} = \frac{1}{3}\left(2\rho_{\perp} + \rho_{\parallel}\right). \tag{5.1}$$

The overall trend in the Gd-Tm series is represented by Fig. 5.4, where the LB results are plotted as a function of the square of the exchange splitting $\Delta$. The graphs include the results obtained using both ferromagnetic and FSM input potentials listed in Table 5.1. We also show the $c$-axis SDR in Gd calculated using several other values of the local moment constrained by FSM. The exchange splitting $\Delta$ is defined as the difference between the majority- and minority-spin $5d$ band centers (LMTO $C$ parameters) obtained from the LMTO parametrization of the (third-order) potential function $P(E)$ [105]. To improve the accuracy of this determination, these parameterizations are performed with the LMTO linearization energies $\epsilon_\nu$ for both spins

Table 5.1: SDR of heavy rare-earth metals calculated using Landauer-Büttiker (LB) and disordered local moment (DLM) methods. First (second) row for each element: Atomic potentials taken from the ferromagnetic state (from self-consistent DLM local moments). Experimental data are from Refs. [6–12] or as cited.

| Element | Lattice Parameters (a.u.) | Moment ($\mu_B$) | In-plane SDR ($\mu\Omega$ cm) | | | $c$-axis SDR ($\mu\Omega$ cm) | | | Polycrystal SDR ($\mu\Omega$ cm) | | |
|---|---|---|---|---|---|---|---|---|---|---|---|
| | | | LB | DLM | Exp | LB | DLM | Exp | LB | DLM | Exp |
| Gd | a = 6.858 | 7.72 | 58.9 | 59.1 | 108, 105 [66] | 44.9 | 41.5 | 96, 95 [66] | 54.2 | 53.2 | 106.4 |
| | c = 10.952 | 7.44 | 42.0 | 40.2 | | 31.3 | 26.9 | | 38.4 | 35.7 | |
| Tb | a = 6.805 | 6.64 | 45.6 | 46.0 | 82 | 33.5 | 30.2 | 66 | 41.6 | 40.7 | 85.7 |
| | c = 10.759 | 6.35 | 29.1 | 27.7 | | 22.2 | 17.6 | | 26.8 | 24.3 | |
| Dy | a = 6.784 | 5.58 | 35.4 | 35.3 | 62, 57 [64] | 25.1 | 22.6 | 44, 45 [64] | 32.0 | 31.1 | 57.6 |
| | c = 10.651 | 5.27 | 19.4 | 18.6 | | 14.1 | 11.7 | | 17.6 | 16.3 | |
| Ho | a = 6.760 | 4.46 | 23.8 | 22.8 | 41 | 16.8 | 14.3 | 24 | 21.5 | 20.0 | 32.3 |
| | c = 10.612 | 4.20 | 12.0 | 10.8 | | 7.93 | 6.8 | | 10.6 | 9.43 | |
| Er | a = 6.725 | 3.33 | 13.4 | 12.2 | 21, 32.4 [68] | 8.56 | 7.5 | 13, 18.0 [68] | 11.8 | 10.6 | 23.6 |
| | c = 10.559 | 3.14 | 6.68 | 5.94 | | 4.11 | 3.44 | | 5.82 | 4.81 | |
| Tm | a = 6.685 | 2.21 | 5.96 | 5.23 | 22.3, 21.2 [67] | 3.43 | 3.2 | 7.4, 7.4 [67] | 5.12 | 4.56 | 14.9 |
| | c = 10.497 | 2.088 | 3.00 | 2.32 | | 1.67 | 1.44 | | 2.56 | 2.02 | |

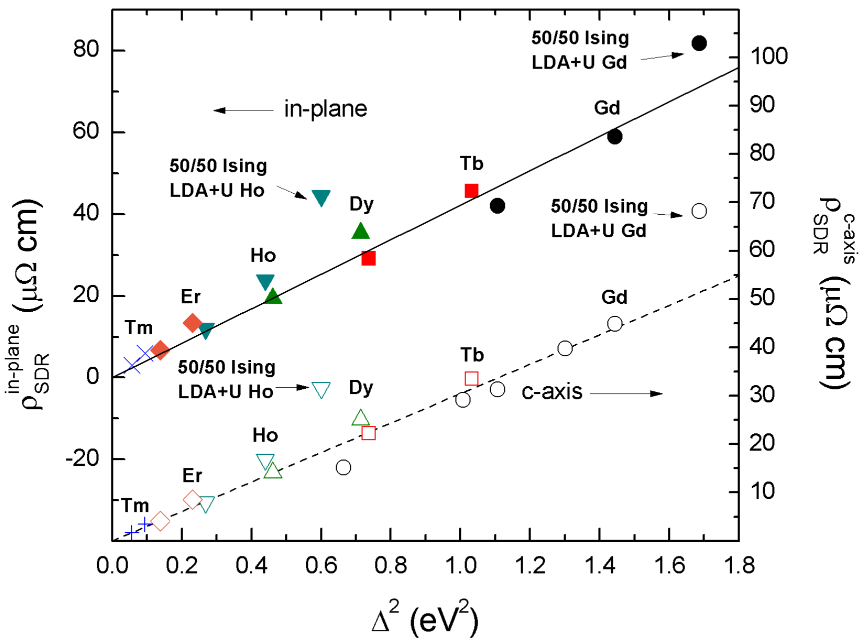

Figure 5.4: SDR as a function of the squared exchange splitting $\Delta^2$ in the open-core approximation (or as indicated). Filled shapes: in-plane SDR; open shapes: *c*-axis SDR. Circles: Gd, squares: Tb, triangles: Dy, inverted triangles: Ho, diamonds: Er, crosses: in-plane Tm, pluses: *c*-axis Tm. Points labeled *50/50 Ising LDA+U*: calculations with LDA+$U$ for $4f$ orbitals in the basis set and Ising spin disorder.

selected so that they are close to the $C$ parameter for the same spin.

Calculated SDR for Gd and Ho with the $4f$ orbitals treated using the LDA+$U$ method are also shown in Fig. 5.4. LDA+$U$ calculations enhance the local moments compared to the open-core approximation to $7.87\mu_B$ for Gd and $4.64\mu_B$ for Ho. The calculated SDR are also enhanced to 81.7 $\mu\Omega$ cm (in-plane) and 68.2 $\mu\Omega$ cm (*c*-axis) for Gd, and to 44.4 $\mu\Omega$ cm (in-plane) and 31.6 $\mu\Omega$ cm (*c*-axis) for Ho.

As seen from Table 5.1, the calculated results are systematically and significantly lower compared to experimental data, particularly when DLM local moments are used. Fig. 5.5 shows the effect of applying quantum corrections according to the models mentioned in Sec. 5.1. For this purpose we used the LB results obtained using the atomic potential from the ferromagnetic state, which are somewhat closer

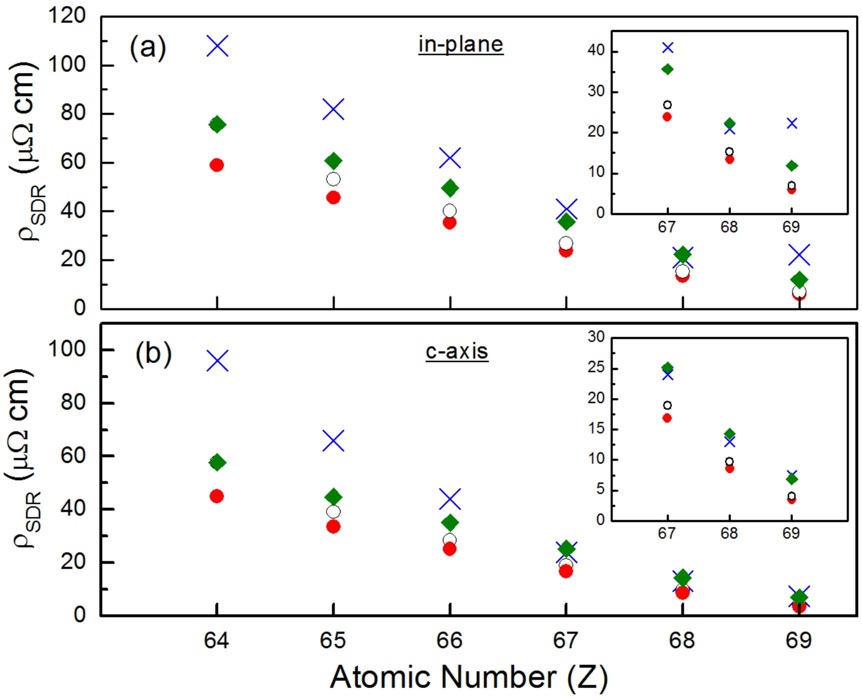

Figure 5.5: Comparison of calculated SDR with experiment and the effect of quantum corrections. (a) In-plane direction, (b) $c$ axis direction. Insets: enlarged scale. Crosses: experimental data (Legvold *et al.*); filled circles: LB calculations with atomic potentials taken from the ferromagnetic state. Filled diamonds: LB results multiplied by $(S+1)/S$; open circles: LB results multiplied by $(J+1)/J$.

to experiment. The experimental data are plotted for comparison.

## 5.5 Discussion

Table 5.1 demonstrates excellent agreement between the LB and DLM methods. Since the DLM method may be viewed as a single-site approximation to LB results, this agreement shows that the DLM method is quite accurate for transport calculations in all of the heavy rare-earth metals. This is not surprising in view of the excellent agreement of the DOS demonstrated above.

The dependence of SDR on $\Delta^2$ shown in Fig. 5.4 indicates a fairly universal linear trend for both crystallographic directions of transport. Since the exchange splitting plays the role of the disorder strength for SDR, this approximately linear dependence is natural. Still, Fig. 5.4 also reveals systematic deviations from this general trend. The $\rho(\Delta^2)$ dependencies for individual elements (obtained using FSM) tend to have a larger slope compared to the universal $\rho \propto \Delta^2$ trend for the series. In particular, when two different elements are constrained by FSM to have the same exchange splitting $\Delta$, the heavier element has a somewhat larger SDR for both crystallographic directions (compare the nearby points for Dy and Tb or those for Ho and Dy). These deviations can at least partially be related to the systematic reduction of the Fermi velocities in the series. Table 5.2 lists the values of the Fermi surface integral, which appears in the semiclassical expression for the conductivity in the $\tau$-approximation. Note, however, that a direct application of the semiclassical theory to the SDR problem would be rather questionable. Indeed, such treatment requires that the electronic bands are well-defined, and that the typical separations between them are small compared to the scattering potential. In the SDR problem the bands are spin-degenerate in the absence of the scattering potential; in the paramagnetic state the band splitting and the scattering potential are of the same order.

Table 5.2: Calculated integrals $\int v_\alpha^2 \delta(E - E_F) d\mathbf{k}$ (atomic units) in the fictitious non-magnetic state

| Element | In-plane | $c$-axis |
|---|---|---|
| Gd | 0.679 | 1.247 |
| Tb | 0.655 | 1.257 |
| Dy | 0.609 | 1.217 |
| Ho | 0.571 | 1.166 |
| Er | 0.548 | 1.135 |
| Tm | 0.532 | 1.108 |

The calculated in-plane resistivity is greater compared to the $c$-axis direction for all elements, and the magnitude of this anisotropy gradually increases in the Gd-Tm series. These features agree very well with the experimental data, suggesting that first-principles calculations correctly capture the anisotropy of the electronic structure near the Fermi surface and its dependence on the local moment of the $4f$ shell. Note that the anisotropy of SDR is much smaller than that of the Fermi surface integral for $\sigma$ in the $\tau$-approximation (see Table 5.2); this latter anisotropy, moreover, barely depends on the nuclear charge.

Contrary to the crystallographic anisotropy of SDR and its trend in the series, the magnitude of the calculated SDR is significantly smaller compared to experiment, even when the atomic potentials from the ferromagnetic state are used (see Table 5.1 and Fig. 5.5). The experimental values are larger by factors of 1.83/2.14 (in-plane/$c$-axis) for Gd, 1.80/1.97 for Tb, 1.75/1.75 for Dy, 1.72/1.43 for Ho, 1.57/1.52 for Er and 3.74/2.16 for Tm. The worst agreement is found for Gd, Tb and especially Tm. Similar disagreement is, of course, found for polycrystals. This systematic underestimation suggests that while the electronic structure is likely described reasonably well, the scattering *rates* are in reality much higher than predicted by our classical frozen-spin-disorder model.

We have verified the reliability of our description of the electronic structure by comparing the electronic bands of Gd to highly precise full-potential calculations and found that a slightly improved treatment with added empty spheres does not materially change the results (see Appendix 5.B for details). We have also checked the effect of including the $4f$ states in the basis set using the LDA+$U$ method, as described in Sec. 5.2.1, using Gd and Ho as representative examples. As shown in Fig. 5.4, the SDR values obtained in this way for both Gd and Ho are enhanced compared to the open-core approximation, but the majority of this enhancement is due to the larger exchange splitting in LDA+$U$ calculation. (This effect is likely due to the dependence of the $f$-$d$ exchange integral on the energy of the $4f$ wavefunction.) There is also a small enhancement of about 5% due to the use of a collinear Ising-like random distribution instead of a fully noncollinear random distribution. After accounting for these contributions, we find that the remaining effect of including the $4f$ states in the basis set is an SDR enhancement in the range of 12-20%. According to photoemission data [182], the $4f$ states of other heavy rare-earth elements also lie far from the Fermi level compared to the exchange splitting and therefore should not strongly affect spin-disorder scattering.

As discussed in Sec. 5.1, the localized character of the $4f$ states suggests that their quantum character needs to be taken into account. In two simple models assuming either very strong or very weak $S$-$L$ coupling in the fully localized $4f$ shell, the quantum correction to our classical results is either $(J+1)/J$ or $(S+1)/S$. In Ref. [70] it was argued that all experimental results agree with the strong-coupling $(J+1)/J$ correction, but only after an empirical electronic correction was introduced. Since in our calculations all electronic structure effects are *already* included, we can see whether a quantum correction can systematically improve agreement with experiment without any additional adjustable parameters. The results predicted by two kinds of quantum corrections are included in Fig. 5.5.

Both correction factors are always greater than 1, and therefore they tend to improve agreement with experiment. It is clear, however, that the $(J+1)/J$ correction is generally insignificant. The $(S+1)/S$ correction provides a much more notable improvement, particularly for Ho and Er, and to a lesser degree for other elements. However, the disagreement for Gd and Tb remains significant, particularly considering that the results shown in Fig. 5.5 are based on the atomic potentials taken from the ferromagnetic state. Therefore, it is likely that the $(S+1)/S$ correction does not fully capture the effects of the quantum character of the $4f$ shell on conduction electron scattering.

Full-potential band structure calculations show that the conduction band structure is quite insensitive to the orbital structure of the $4f$ shell, as long as its total spin is kept fixed (see Appendix 5.C). Therefore, the random multipole potential generated by the (hypothetical) fluctuations of the orbital structure of the $4f$ shell does not provide an important scattering mechanism. Nevertheless, these fluctuations can affect the scattering rates by modifying the allowable sets of initial and final states for electron scattering.

Apart from more complicated quantum corrections, two other mechanisms can further enhance SDR. First, we found that the inclusion of spin-orbit coupling for conduction electrons in DLM increases the resulting SDR of Gd by approximately 20% for both transport directions, and for both ferromagnetic and DLM values of the local moments. Second, the assumption that phonon and spin-disorder scattering mechanisms are entirely independent and contribute additively to the total resistivity may be wrong. If deviations from Matthiessen's rule for phonon and spin-disorder mechanisms are important, they should be more pronounced in Gd and Tb where the Curie temperature is large and comparable with the Debye temperature. This issue deserves a separate study, and is the topic of Chapter 6.

## 5.6 Conclusions

In this chapter we investigated the SDR of the heavy rare-earth metals using two complementary approaches, one based on the explicit spin-disorder averaging of the Landauer-Büttiker conductance of a supercell, and another one using linear response calculations in the paramagnetic state described by the coherent potential approximation (DLM method). The two methods agree well with each other and properly capture the crystallographic anisotropy of the spin-disorder resistivity. A fairly universal linear $\rho(\Delta^2)$ dependence is obtained for the series, where $\Delta$ is the exchange splitting of the conduction band in the ferromagnetic state.

The calculated spin-disorder resistivities are systematically smaller than experiment, suggesting that the scattering rates are underestimated by the classical frozen-spin-disorder model. A quantum correction factor of $(S+1)/S$ significantly improves agreement with experiment, especially for heavier elements. Moderate improvement is also obtained in individual cases by including the $4f$ states in the basis set and by including spin-orbit coupling. Still, all these corrections are insufficient at least for Gd and Tb. Since in these two elements the Curie and Debye temperatures are comparable, it is possible that deviations from Matthiessen's rule for spin-disorder and phonon scattering may be important.

## 5.A Convergence with respect to supercell cross-section

The cross-section of our supercells used in the LB calculations was chosen to be large enough to minimize finite-size effects. The sufficiency of these sizes was established by convergence tests for Gd, Ho and Tm. For $c$-axis transport we increased the cross-section to $5\times5$ (area of $12.5a^2\sqrt{3}$ with 25 atoms per monolayer) and integrated using a $20\times20$ $k$-point mesh. For in-plane transport we increased the cross-section to $4\times3$ (area of $12ac\sqrt{3}$ with 24 atoms per monolayer) and integrated using a $12\times12$ $k$-point mesh.

Table 5.3 summarizes the dependence of the SDR on the supercell cross-section. The local moment used for each element is included in the table. We used the reduced

Table 5.3: The dependence of the SDR on the supercell cross-section (units of $\mu\Omega$ cm).

| | in-plane | | $c$-axis | |
|---|---|---|---|---|
| Element | 3x2 | 4x3 | 4x4 | 5x5 |
| Gd ($7.72\mu_B$) | | | 44.9 | 43.8 |
| Ho ($4.20\mu_B$) | 16.7 | 16.5 | 8.4 | 8.6 |
| Tm ($2.21\mu_B$) | 5.96 | 6.05 | 3.43 | 3.55 |
| Tm ($2.088\mu_B$) | 3.00 | 3.09 | 1.67 | 1.71 |

moment taken from DLM for Ho, and both the ferromagnetic and DLM local moments for Tm. The results for different cross-sections agree very well in all cases.

## 5.B Comparison with full-potential band structure

To verify the adequacy of our TB-LMTO representation of the band structure, we chose Gd as a representative example and performed a full potential linearized augmented planewave (FLAPW) calculation using the FLEUR software package [193] for comparison. The $4f$ states were kept in the partially polarized core, as in most of the TB-LMTO calculations reported here. The FLAPW and LMTO band structures for Gd are shown in Fig. 5.6(a). Our FLAPW calculation is consistent with the one reported in Ref. [181] and well with angle-resolved photoelectron spectroscopy measurements [194]. Near the Fermi level the TB-LMTO band structure is quite close to FLAPW, but there is a notable deviation along the H-K and K-Γ symqmetry lines.

The agreement with FLAPW band structure is improved by adding empty spheres in the TB-LMTO basis set. We included the unoccupied $5f$ orbitals in the basis set for Gd and reduced the local Gd moment to $7.603\mu_B$ using FSM. The resulting band

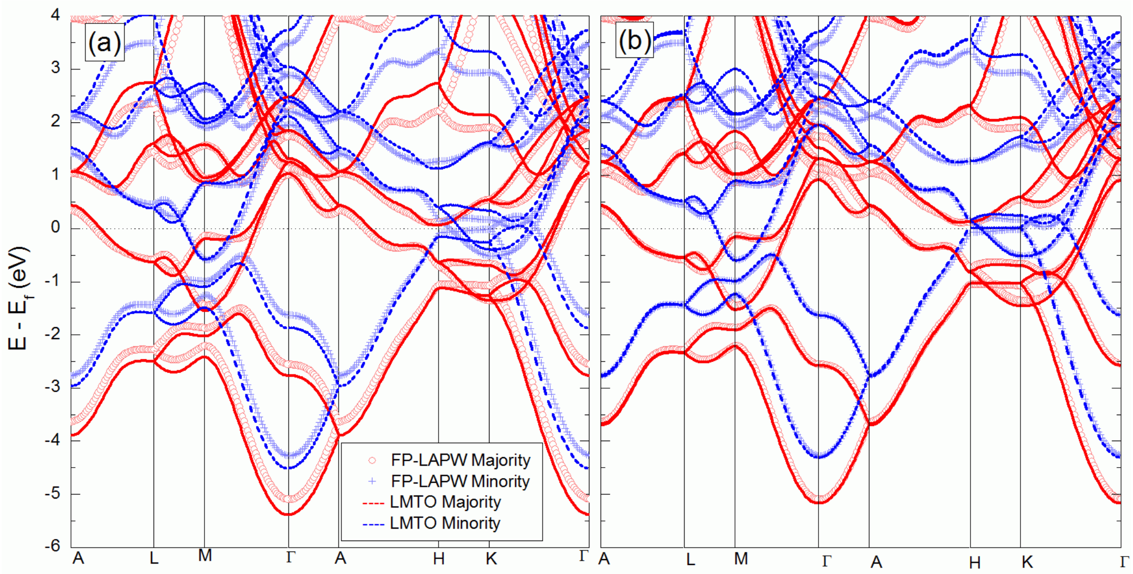

Figure 5.6: Band structures calculated using TB-LMTO and full-potential linear augmented plane wave (FLAPW) methods. Solid red line: majority-spin LMTO, dashed blue: minority-spin LMTO. Open red circles: majority-spin FLAPW, blue plus signs: minority-spin FLAPW. (a) No empty spheres in the LMTO basis set. (b) With empty spheres in the LMTO basis. Note the improved agreement along the H-K and K-Γ symmetry lines.

structure is shown in Fig. 5.6(b); the agreement with FLAPW near the Fermi level is now almost perfect.

The SDR was calculated in the same way as described in Sec. 5.2.1 with the following modifications: the *c*-axis was calculated using a 2 × 2 supercell with 4 Gd atoms per monolayer (there are 12 empty spheres surrounding each monolayer of 4 Gd atoms); random spin disorder is introduced only on the Gd sites; 48 × 48 *k*-point mesh for Brillouin zone integration; configurationally averaging over 30 random spin configurations for each thickness.

The calculated SDR using the adjusted band structure is 47.4 $\mu\Omega$ cm, which is 6% larger than the result of 44.9 $\mu\Omega$ cm reported in Table 5.1. This increase is not statistically significant. Therefore, we conclude that the original TB-LMTO representation of the band structure is sufficiently accurate for SDR calculations.

## 5.C Fluctuations of the orbital structure of the $4f$ shell

The effect on the conduction bands of the multipole potential generated by variations in the orbital structure of the $4f$ states (violating Hund's rules) was evaluated using a FLAPW [193] calculation for Ho. For this purpose the $4f$ states were included in the valence basis and subjected to the LDA+$U$ potential (fully localized limit [187] with $U = 7.5$ eV and $J = 0.7$ eV). The band structures for different orbital occupations of the $4f$ shell corresponding to orbital momenta $L = 0$, 4, 5, 6 were calculated self-consistently. We found no detectable effect of the $4f$ shell orbital structure on the conduction bands near the Fermi energy; the bands were modified only close to the unoccupied $4f$ states, which in all cases were more than 1 eV above the Fermi energy. Therefore, we conclude that fluctuations of the orbital structure of the $4f$ shell do not materially contribute to the scattering potential seen by the conduction electrons.

# Chapter 6

# First-principles investigation of the electronic origin of phonon and Anderson disorder-induced resistivity enhancements in spin-disordered Fe and Gd

## 6.1 Introduction

The electrical resistivity of magnetic metals has several scattering contributions, which include scattering due to impurities, thermal vibrations of ions (phonons), and thermal fluctuations of the local magnetic moments [13, 59, 60]. When evaluating the electrical resistivity Matthiessen's rule is typically assumed, in which scattering sources are treated as independent and are summed together [195]. Impurities are observed as a residual resistivity at low temperatures and the phonon contribution to the resistivity is well described by the Bloch-Grüneisen formula [196]. However the understanding of spin-disorder scattering at finite temperatures is incomplete [107]. In magnetic metals the spin-disorder scattering rate increases with temperature and saturates in the paramagnetic state where spin directions are random and uncorrelated. The saturated magnetic resistivity is called the spin-disorder resistivitiy (SDR).

The transition metal Fe and the heavy rare-earth metal Gd both have received much attention in the scientific literature. The electrons responsible for magnetism are itinerant in Fe and highly localized in Gd, and comparing the magnetic resistivity of each may reveal the influence of electron localization on scattering rates. The experimental resistivity studies of Fe [2–4, 197] agree on the transition temperature of 1040 K and on the general shape of the resistivity curve, although the absolute value of the residual subtracted resistivity differs, see Fig. 6.1 and Sec. 6.4 for additional discussion. The SDR of Fe was reported to be 80 $\mu\Omega$ cm [195]. The electrical resistivity tensor of Gd is anisotopic and has independent components parallel to the c-axis and in-plane directions, and the experimental studies are in quantitative agreement [11, 66, 198], with the resistivity anisotropy decreasing as the melting point is approached. The SDR of Gd was reported for c-axis ($\|$) and in-plane ($\perp$) directions to be $\rho_{\|} = 95$ $\mu\Omega$ cm and $\rho_{\perp} = 105$ $\mu\Omega$ cm [66].

The implementation of density functional theory with transport calculation schemes allows for a quantitative prediction of the SDR from first principles. One such approach is to solve the electronic structure problem in the disordered-local moment (DLM) approximation [116] and calculate transport using linear response [190, 191]. Recently this approach was used to evaluate the SDR in transition metal ferromagnets and alloys [188], as well as the heavy rare-earth metals [199]. Another approach is to construct supercells and average over the Landauer-Büttiker conductance of random spin-disordered configurations, as was used to study the transition metals Fe and

Ni [179], and the heavy rare-earth metals [199]. These two complementary methods are in good agreement with each other and the predicted SDR of Fe is in agreement with experiment [195], while the predicted SDRs of the heavy rare-earth metals are strongly underestimated compared with experiment [66]. In particular the Gd SDR is underestimated by a factor of 2, which suggested that a scattering mechanism was missing from the theoretical description.

Phonons may be modeled in supercell calculations using frozen thermal lattice disorder, where the atomic positions of ions are displaced from equilibrium. Recently this approach was used to study Gilbert damping, with the lattice disorder modeled with a Gaussian distribution [5]. First-principles calculations of the resistivity of collinear Fe as a function of temperature using lattice displacements determined from ab-initio molecular dynamics simulations have also been demonstrated [200].

Deviations from Matthiessen's rule have been observed in dilute nonmagnetic and magnetic alloys (see Ref. [201] for a review of the topic). For alloys, the total resistivity can be expressed as,

$$\rho_a(c,T) = \rho_p(T) + \rho_0(c) + \Delta(c,T), \tag{6.1}$$

where $c$ is the impurity concentration, $T$ is the temperature, $\rho_p(T)$ is the temperature-dependent resistivity of the (pure) host metal, $\rho_0(c)$ is the residual resistivity at concentration $c$, and $\Delta(c,T)$ is the deviation from Matthiessen's rule at concentration $c$ and temperature $T$. A source of deviations is anisotropic electron-phonon scattering due to violations of the $\tau$-approximation [202], which for example may occur on an anisotropic Fermi surface [203–205]. The two-band model for non-magnetic alloys captures the qualitative features of such deviations [206], which are small compared to the residual resistivity. For example, at room temperature, dilute $\mathrm{Cu}_{1-x}\mathrm{Au}_x$ ($x <$

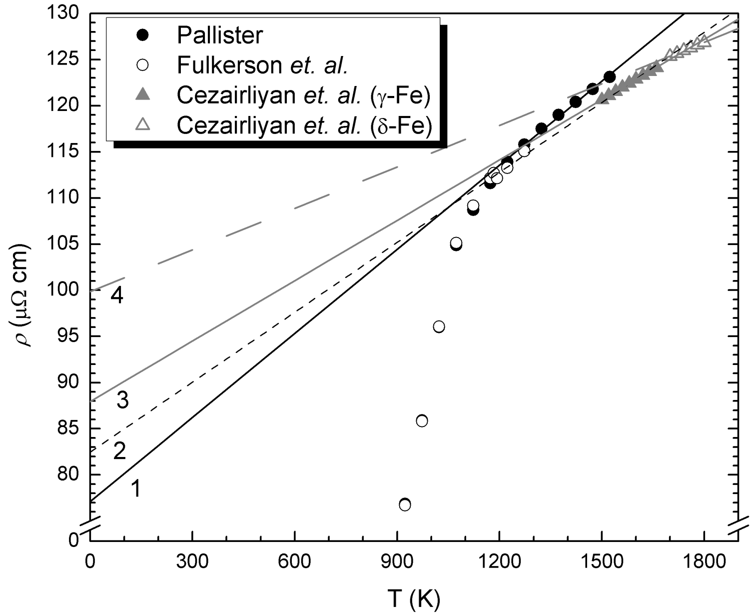

Figure 6.1: Electrical resistivity data for Fe from Refs. [2–4]. The four lines correspond to fits to data from (1) Pallister [2], range of 1223 K $\leq T \leq$ 1523 K, slope of 0.0304 $\mu\Omega$ cm/K, intercept of 77.1 $\mu\Omega$ cm; (2) Fulkerson *et. al.* [3] and Cezairliyan *et. al.* [4], range of 1193 K $\leq T \leq$ 1660 K, slope of 0.0253 $\mu\Omega$ cm/K, intercept of 82.5 $\mu\Omega$ cm; (3) Cezairliyan *et. al.* [4], range of 1500 K $\leq T \leq$ 1660 K, slope of 0.0218 $\mu\Omega$ cm/K, intercept of 88.0 $\mu\Omega$ cm; (4) Cezairliyan *et. al.*, range of 1700 K $\leq T \leq$ 1800 K, slope of 0.0150 $\mu\Omega$ cm/K, intercept of 100 $\mu\Omega$ cm.

0.0025) has a deviation of $\Delta(c,T)/\rho_0(c) \sim 0.10$ [207]. Magnetic alloys, on the other hand, may exhibit very large deviations, for example dilute $\mathrm{Fe}_{1-x}\mathrm{Mn}_x$ ($x = 0.01$) at room temperature has a deviation of $\Delta(c,T)/\rho_0(c) = 2.2$ [208]. These large deviations are understood to be a consequence of the two-channel model [209–211] where spin-up and spin-down currents are independent and flow in parallel.

In electrical resistivity experiments, the SDR is identified as the intercept of an appropriate fitting to the high temperature data, while in first-principles calculations it is directly calculated without a $T \to 0$ K limiting. In this chapter it is suggested that a more appropriate comparison using the supercell approach is to simulate lattice vibrations as in Ref. [5] combined with spin disorder as in Refs. [179, 199], investi-

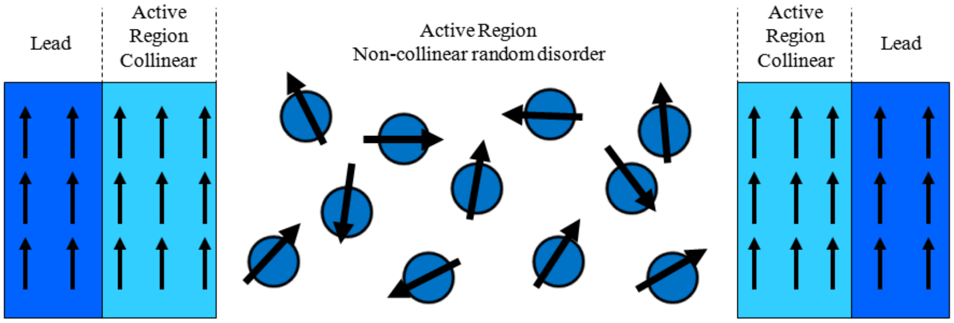

Figure 6.2: A schematic of the supercells used to calculate transport.

gating the resistivity as a function of the atomic mean-square displacement $\Delta^2_{\mathrm{ph}}$. In this scheme, ab-initio calculations show that the inclusion of phonon disorder leads to a non-linear increase in the resistivity $\rho(\Delta^2_{\mathrm{ph}})$ for small displacements and a linear dependence of the resistivity for larger displacements. Fits to the linear region have intercepts that are larger than the "bare" SDR, an enhancement that is modest in Fe and substantial in Gd, suggesting that the neglect of phonons explains why previous Gd SDR calculations were strongly underestimated. It is then shown that these enhancements are electronic in origin, and the spectral function of Gd indicates that the rapid increase in the resistivity can be traced to an interaction between the hole and electron Fermi surfaces. We then close by offering some remarks on how the spectral function calculations compare with recent angle-resolved photo-emission spectroscopy (ARPES) measurements of Gd [194].

## 6.2 Computational methods

For our calculations we used density-functional theory (DFT) in the local density approximation (LDA) as implemented for tight-binding linear muffin-tin orbitals (LMTO) in the atomic sphere approximation. The general method used for SDR calculations is described in Ref. [179] and Chapter 5 and the method for calculating the resistivity of collinear ferromagnets due to lattice vibrations in the frozen thermal lattice approximation (phonon disorder) is described in Ref. [5]. The approach here combines both as shown in the schematic in Fig. 6.2, placing phonon and random, uncorrelated spin disorder on equal footing to simulate the high temperature region, $T > T_c$ and $T \gg \Theta_D$. The atomic displacements are modeled using a Gaussian distribution with the mean-square displacement $\Delta^2_{\mathrm{ph}}$ input parameter used to characterize the thermal fluctuations of atomic positions. The effects of simultaneous spin and phonon disorder were investigated in the transition metal Fe and the heavy rare-earth metal Gd.

The lattice constant for each element was set to the experimental value. Both the $\alpha$ (BCC) and $\gamma$ (FCC) phases of Fe were investigated, with lattice constants 2.8655Å for $\alpha$-Fe and 3.6394 Å for $\gamma$-Fe, where the lattice constant for $\gamma$-Fe was measured at $T = 1190$ K, close to the $\alpha - \gamma$ phase transition [212]. The crystal structure of Gd is hcp, with lattice constant 3.629 Å and a $c/a$ ratio of 1.597.

The *spd* basis set of LMTO was used to solve for the electronic structure of Fe and Gd. We note that the primary effects of using the expanded *spdf* basis in Fe compared with *spd* is the reduction of local moments and the modification of final scattering states, which modifies the calculated value of the SDR, see Ref. [179] for more discussion. In Gd, using the *spdf* basis in LDA positions the 4f bands too close to the Fermi level [181]. For our calculations the 4f electrons are placed in the ionic core (open-core approximation) and the *spd* basis is used for the conduction electrons, for additional discussion, see Ref. [199] or Chapter 5.

The conductance is calculated using the same method as used in Chapter 5. The area-resistance vs active region length plots in Fig. 6.3 are examples of the calculations, with the slope identified as the resistivity due to phonon and spin disorder.

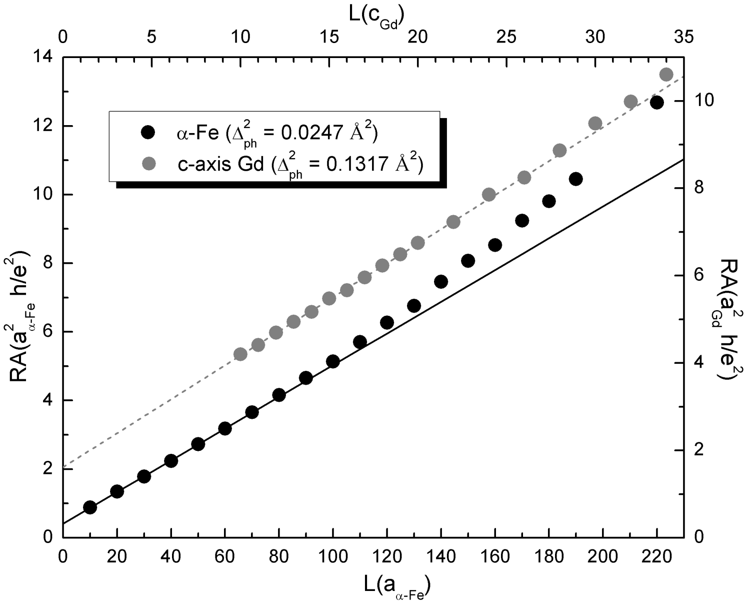

Figure 6.3: The area-resistance product as a function of active disordered region length with random spin and/or phonon disorder. The black circles (read using bottom and left axes) are calculations with collinear ferromagnetic $\alpha$-Fe and a phonon mean-square displacement $\Delta^2_{\mathrm{ph}} = 0.0247$ Å$^2$, and the gray circles (read using top and right axes) are calculations with randomly spin-disordered Gd with current flowing parallel to the c-axis and a phonon mean-square displacement $\Delta^2_{\mathrm{ph}} = 0.1317$ Å$^2$

The resistivity tensor for $\alpha$-Fe and $\gamma$-Fe has one independent component for current flowing along one of the cubic axis directions, while for Gd the tensor has two independent components for current flowing parallel and perpendicular to the hexagonal $c$ axis. The $\alpha$-Fe supercells were constructed with a 4 × 4 (16 atoms per monolayer, interlayer spacing $a_{\alpha\text{-Fe}}/2$) square cross section of area $16a^2_{\alpha\text{-Fe}}$, and the $\gamma$-Fe supercells were constructed with a 3 × 3 (18 atoms per monolayer, interlayer spacing $a_{\gamma\text{-Fe}}/2$) square cross section of area $9a^2_{\gamma\text{-Fe}}$. For Gd, the supercells for current flowing along the c-axis were constructed with a 4 × 4 (16 atoms per monolayer, interlayer spacing $c/2$) cross section of area $8a^2_{\mathrm{Gd}}\sqrt{3}$, and the supercells for current flowing along one of the in-plane lattice vectors were constructed with a 3 × 2 (12 atoms per monolayer, interlayer spacing $a_{\mathrm{Gd}}$) rectangular cross section of width $3a_{\mathrm{Gd}}\sqrt{3}$ and height $2c$. The integration over the Brillouin zone was performed using a $25 \times 25$ k-point mesh for the collinear $\alpha$-Fe with phonon disorder calculations, and for calculations with both random spin and phonon disorder, a $15 \times 15$ k-point mesh was used for $\alpha$-Fe, a $20 \times 20$ k-point mesh for $\gamma$-Fe, and a $24 \times 24$ k-point mesh for both transport directions of Gd. In all instances the conductance was averaged over 15 configurations when the mean-square displacement $\Delta_{ph}^2 < 0.0064a^2$ ($a$ is the lattice constant), and averaged over 30 configurations when the mean-square displacement $\Delta_{ph}^2 \geq 0.0064a^2$.

Input moments from different self-consistent calculations were used in our transport calculations. The resistivity of $\alpha$-Fe and Gd were both calculated using the input potentials from the self-consistent ferromagnetic ground state. In addition, the disordered-local moment (DLM) approach [116], which is an implementation of the coherent potential approximation, was used to calculate the self-consistent potentials of the paramagnetic state. The local moment of $\alpha$-Fe in the DLM state is nearly identical to the ferromagnetic state, so transport calculations were not repeated. $\gamma$-Fe is a high-temperature phase so only the DLM potential was used as input. The DLM potential for Gd was used in addition to the ferromagnetic potential along the in-plane direction. The spectral function, which is the imaginary part of the Green's function and may be thought of as the generalized density of states, was also calculated in the coherent potential approximation.

For comparison with phonon disorder, Anderson disorder was also used with the square of the disorder amplitude $\Delta_{\mathrm{And}}^2$ replacing the mean-square atomic displacement as the parameter to describe thermal fluctuations. Anderson disorder is applied as a rigid shift of the band centers (LMTO potential parameters $C$ and $E_\nu$) of individual atomic sites according to a random distribution.

## 6.3 Results

The area-resistance vs disordered region length plots in Fig. 6.3 for $\alpha$-Fe and Gd are typical of the results from the transport calculations. The large resistivities ($> 100\ \mu\Omega$ cm) seen in Figs. 6.4(b) and 6.4(c) imply small electronic mean-free paths and the possibility of localization effects (as seen in Chapter 4) where diffusive behavior breaks down [173]. This was checked for by varying the active region to long lengths as shown in Fig. 6.3, where exponential deviations of positive curvature from ohmic behavior were observed, establishing the length scale over which such effects become important. The points used for fitting to extract the resistivity were limited to the linear region where localization effects were unimportant.

Fig. 6.4(a) is the plot of the calculated resistivity $\rho$ as a function of $\Delta^2_{\mathrm{ph}}$ for collinear $\alpha$-Fe, displaying our results and results by Liu *et. al.* in Ref. [5]. The fit has a slope of $1381 \pm 15\ \mu\Omega$ cm/$\text{Å}^2$. The method used by Liu *et. al.* is formally the same as ours and we were able to reproduce their results.

Figs. 6.4(b) and 6.4(c) depict the resistivity as a function of $\Delta^2_{\mathrm{ph}}$ when spin and phonon disorder are combined. The error bars of the resistivities in both panels are approximately half the height of the data symbols, where the average Fe error bar height is $\sim 0.5\ \mu\Omega$ cm and the average Gd error bar height is $\sim 0.9\ \mu\Omega$ cm. In Fig. 6.4(b) the results for $\alpha$-Fe with input moment 2.27 $\mu_B$ and $\gamma$-Fe with input moment 2.11 $\mu_B$ are shown. The solid line fit to the $\alpha$-Fe data has a slope of $134 \pm 5$ $\mu\Omega$ cm/$\text{Å}^2$ and an intercept of $129 \pm 1\ \mu\Omega$ cm; the dashed line fit to the $\gamma$-Fe data has a slope of $120 \pm 6\ \mu\Omega$ cm/$\text{Å}^2$ and an intercept of $126 \pm 1\ \mu\Omega$ cm. In Fig. 6.4(c) the results for Gd with current flowing parallel and perpendicular (in-plane) to the c-axis with input moment $7.72\mu_B$ are shown, as well as another set of in-plane calculations using the input moment of $7.45\mu_B$, which is the moment from the self-consistent DLM

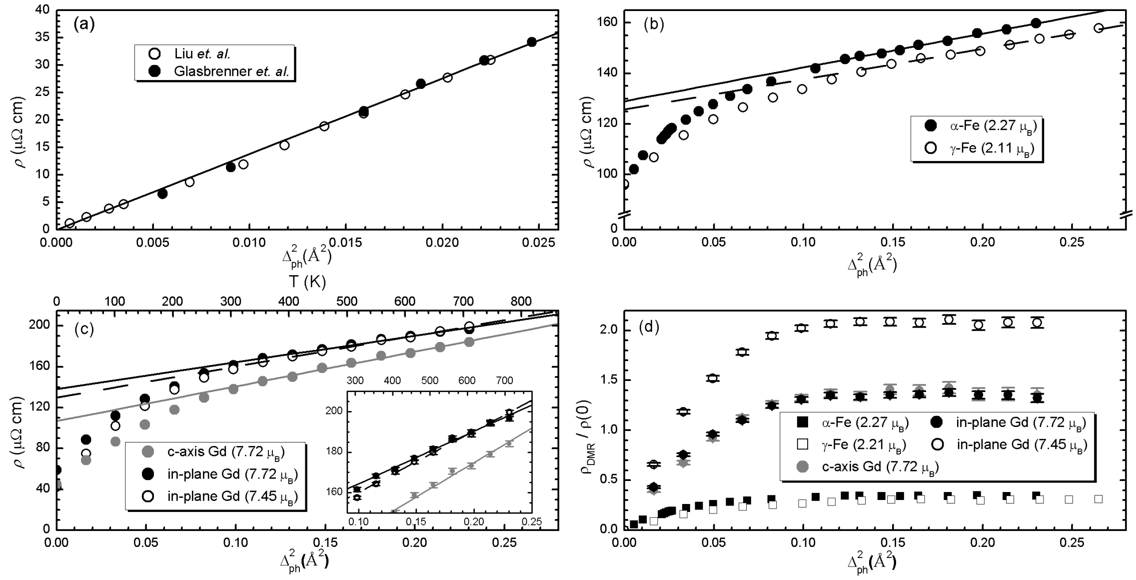

Figure 6.4: Panels (a), (b), and (c) show the resistivity as a function of the mean-square displacement $\Delta^2_{\text{ph}}$ for Fe and Gd. The top axis in (c) shows the temperature mapping of the Gd results. Panel (d) shows the ratio of deviations from Matthiessen's rule $\rho_{\text{DMR}}$ over the SDR $\rho(0)$ as a function of $\Delta^2_{\text{ph}}$ for Fe and Gd. The results in (a) are for a collinear spins, while in (b), (c), and (d) the spins are randomly disordered. (a) $\alpha$-Fe, the closed circles are our calculations and the open circles are from Ref. [5]. (b) $\alpha$-Fe, open circles; $\gamma$-Fe, closed circles. (c) c-axis Gd ($m = 7.72\mu_B$), closed gray circles; in-plane Gd ($m = 7.72\mu_B$), closed black circles; in-plane Gd ($m = 7.45\mu_B$), open circles; Inset: Scaled plot of linear region of in-plane Gd results. (d) $\alpha$-Fe, closed squares; $\gamma$-Fe, open squares; c-axis Gd ($m = 7.72\mu_B$), closed gray circles; in-plane Gd ($m = 7.72\mu_B$), closed black circles; in-plane Gd ($m = 7.45\mu_B$), open circles.

calculation. The solid gray fit to the c-axis Gd data ($m = 7.72\mu_B$) has a slope of $340 \pm 11$ $\mu\Omega$ cm/Å$^2$ and an intercept of $107 \pm 2$ $\mu\Omega$ cm; the solid black fit to the in-plane Gd data ($m = 7.72\mu_B$) has a slope of $269 \pm 9$ $\mu\Omega$ cm/Å$^2$ and an intercept of $138 \pm 2$ $\mu\Omega$ cm; the dashed fit to the in-plane Gd data ($m = 7.45\mu_B$) has a slope of $303 \pm 9$ $\mu\Omega$ cm/Å$^2$ and an intercept of $130 \pm 1$ $\mu\Omega$ cm.

The top horizontal axis of Fig. 6.4(c) is a mapping of $\Delta^2_{\text{ph}} \mapsto T$ for Gd using the calculated in-plane slope with the $7.45\mu_B$ input moment and the experimental in-plane slope from Ref. [66]. Using the ferromagnetic input potential calculations instead reduces the scaling of the temperature axis by a factor of 0.86. To obtain this mapping, it is known from the equipartition theorem that $\Delta_{\mathrm{ph}}^2 \equiv \langle x^2 + y^2 + z^2 \rangle = CT$ for a Gaussian distribution, where $x$, $y$, and $z$ are the Cartesian coordinates of a harmonic oscillator situated at the origin and $C$ is a constant. From the theoretical calculations and experimental measurements of $\rho$, $d\rho/d\Delta_{\mathrm{ph}}^2 = a$ and $d\rho/dT = b$, and from the equipartition theorem $d\Delta_{\mathrm{ph}}^2/dT = C$ it follows that $C = b/a$ maps $\Delta_{\mathrm{ph}}^2 \mapsto T$.

Fig. 6.4(d) plots the ratio of the deviations from Matthiessen's rule over the SDR for Fe and Gd, defined as

$$\frac{\rho_{\mathrm{DMR}}(\Delta_{\mathrm{ph}}^2)}{\rho(0)} = \frac{\rho(\Delta_{\mathrm{ph}}^2) - \rho(0) - a\Delta_{\mathrm{ph}}^2}{\rho(0)}, \tag{6.2}$$

where $\rho(\Delta_{\mathrm{ph}}^2)$ is the total resistivity, $\rho(0)$ is the calculated SDR, and $a$ is the slope of the fitted lines in Figs. 6.4(b) and 6.4(c). Eq. 6.2 saturates at 0.344 for $\alpha$-Fe, 0.306 for $\gamma$-Fe, 1.38 for c-axis Gd with input moment $7.72\mu_B$, 1.35 for in-plane Gd with input moment $7.72\mu_B$, and 2.08 for in-plane Gd with input moment $7.45\mu_B$.

Fig. 6.5 shows the DOS for paramagnetic Gd for several different choices of $\Delta_{\mathrm{ph}}^2$. To calculate the DOS we constructed Gd supercells of 64 atoms (4 hexagonal monolayers with 16 atoms per monolayer, periodically repeated in three dimensions) with input moment $7.72\mu_B$ and generated seven random spin disorder configurations and Gaussian distributions with the selected $\Delta_{\mathrm{ph}}^2$. The partial density of states (DOS) was then projected on the local reference frame (z-axis parallel with local moment direction) for each configuration of spin and phonon disorder and averaged over all sites and configurations.

In Fig. 6.6 the resistivity of Gd along the in-plane direction is investigated as a function of Anderson disorder. The random spin-disordered paramagnetic state with ferromagnetic potentials is investigated and compared with calculations using non-magnetic potentials.

The spectral function of Gd at the Fermi energy for different planes in reciprocal space is shown in Fig. 6.7. The first row is the spectral function for the DLM calculation and the second row is DLM plus an Anderson disorder amplitude of 0.95 eV, where in the CPA calculation the Anderson disorder is a non-self-consistent 50/50 mix of DLM potentials whose band centers are either shifted up or down by the specified amplitude. The color scale for the first row of plots is located above the figures and for the second row below the figures.

## 6.4 Discussion

An evaluation of the available experimental resistivity data suggests that there is ambiguity in taking a fit to extract the SDR. The data from several resistivity experiments for Fe is shown in Fig 6.1, along with potential fits to the $T > T_c$ region (Bloch Grüneisen is approximated as a linear fit). The slope of fit 4 is a factor of 2 smaller and the intercept a factor of 1.3 larger than those of fit 1. In addition, because the $\alpha$ ($T \leq 1180$ K) and $\delta$ ($T \geq 1680$ K) phases are BCC, it is anticipated that a smooth continuation of the resistivity curve should connect the two regions, which does not appear consistent with the data and introduces uncertainty into taking a proper fit to extract the SDR. The high temperature single-crystal Gd data [198] over a 1000 K range is not linear, and depending where the fit is taken the intercept will vary. The ratio of the c-axis and in-plane resistivities, an indication of the scattering anisotropy, approaches unity as temperature increases. This may be an indication that the commonly reported SDRs of Fe and Gd could be an underestimation.

The combined effect of random spin and phonon disorder on the resistivity in Figs. 6.4(b) & 6.4(c) for Fe and Gd is that the curves have a region of rapid increase

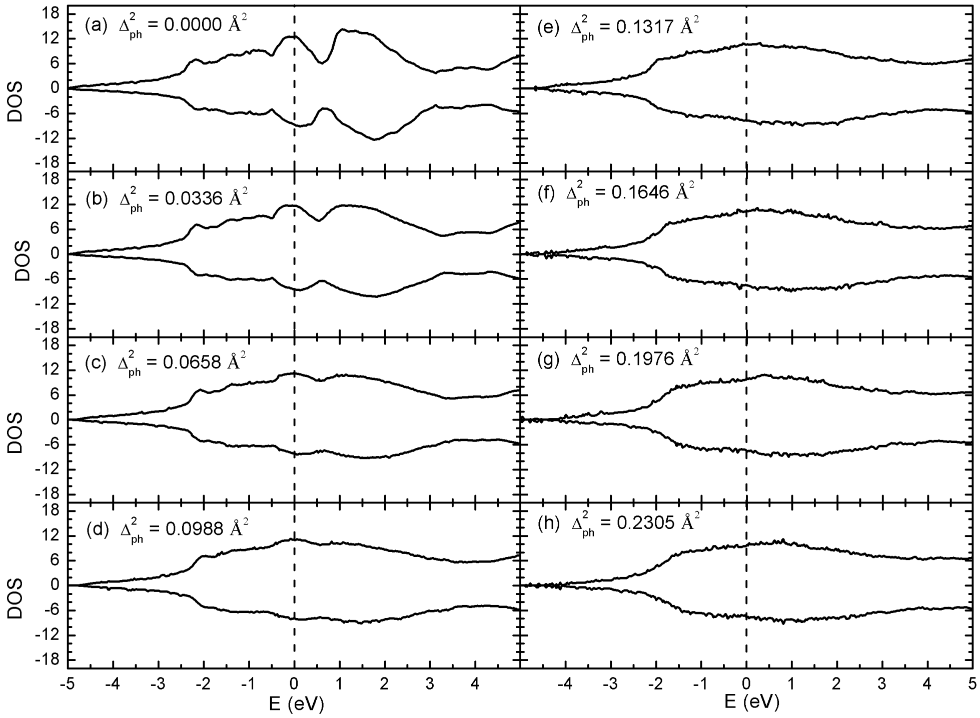

Figure 6.5: Spin-projected local DOS of paramagnetic Gd averaged over 64-atom supercells with random noncollinear local-moment orientations and input moment $7.72\mu_B$ for different values of the phonon disorder mean-square displacement $\Delta^2_{ph}$. The values used are (a) no phonon disorder, (b) $\Delta^2_{ph} = 0.0336$ Å$^2$, (c) $\Delta^2_{ph} = 0.0658$ Å$^2$, (d) $\Delta^2_{ph} = 0.0998$ Å$^2$, (e) $\Delta^2_{ph} = 0.1317$ Å$^2$, (f) $\Delta^2_{ph} = 0.1646$ Å$^2$, (g) $\Delta^2_{ph} = 0.1976$ Å$^2$, (h) $\Delta^2_{ph} = 0.2305$ Å$^2$.

followed by a transition into a linear region with a smaller slope. This is in contrast with the naïve expectation that phonon disorder would simply add to the resistivity a term proportional to $\Delta^2_{\mathrm{ph}}$. A simple visual inspection shows that the intercept of a fit to the linear region (”apparent” SDR) is not equal to the resistivity calculated with no phonon disorder (”bare” SDR). For $\alpha$-Fe ($\gamma$-Fe), the apparent SDR is 1.34 (1.32) times larger than the bare SDR, and for the c-axis (in-plane) direction of Gd, the apparent SDR is 2.4 (2.3) times larger than the bare SDR. The substantial enhancement observed in Gd implies that previous theoretical underestimations of the SDR are due to a neglect of the additional scattering due to phonon disorder.

The apparent SDR is insensitive to the phase of Fe and the input moment in Gd. The bare SDRs of $\alpha$-Fe and $\gamma$-Fe are the same within statistical uncertainty, and the enhancements are also nearly the same. This is not unexpected, as the small and difficult to observe change in resistivity at the $\alpha - \gamma$ transition point at 1180 K in Fig. 6.1 indicates that scattering trends are unaffected. In Gd, the use of the DLM input potential instead of the FM input potential has little effect on the apparent SDR. The absolute resistivity is nearly the same in the linear region of the in-plane direction whether FM or DLM input potentials are used, as can be seen in the inset of Fig. 6.4(c). Unlike the bare SDR case where the input moment plays a central role in scattering, the inclusion of phonon disorder strongly diminishes the scattering effects of variations in the on-site exchange splitting.

The apparent SDR for Fe and Gd is in general agreement with experiment although the absolute value is overestimated. Some of this can be attributed to the atomic sphere approximation which overestimates scattering rates. For Fe, the inclusion of $f$ orbitals in the basis set, which will alter the available final scattering states, led to a strong change in the bare SDR [179] and may similarly lower the apparent SDR. Making the disordered active region potentials self-consistent may also improve agreement with experiment for both Fe and Gd. Including $f$ orbitals or making the active region potentials self-consistent is rather expensive compared to using non-self-consistent potentials and the *spd* basis.

The Debye-Waller factor, a temperature dependent quantity that measures the reduction of the intensity of x-ray diffraction maxima as $T$ is increased, can be used to estimate the temperature dependence of the mean-square phonon displacement $\Delta^2_{\text{ph}}$. Several authors extracted from measurements of the Debye-Waller factor the temperature dependence of $\Delta^2_{\text{ph}}$ of $\alpha$-Fe [213, 214] and compared the results with models [215–217]. The experimental $\Delta^2_{\text{ph}}$ data is noisy at elevated temperatures, but

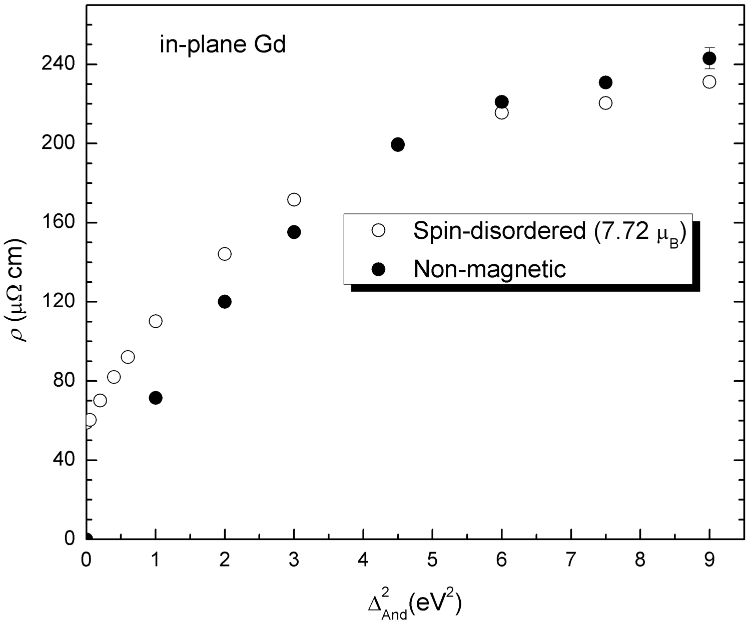

Figure 6.6: Calculated resistivity of in-plane Gd as a function of the square of the Anderson disorder amplitude. The open circles are calculations that included random spin disorder with ferromagnetic potentials for input; closed circles are calculations that used non-magnetic potentials. Unless pictured, the statistical uncertainty is smaller than the width of a data point.

the theoretical model plotted in Ref. [217] may be considered the minimum value of $\Delta^2_{\text{ph}}$ for all temperatures. At the Curie temperature $T = 1040$ K the minimal $\Delta^2_{\text{ph}}$ is estimated to be $\sim 0.053$ Å$^2$. The data for the transition metal copper [218] is more stable at elevated temperatures, and at $T = 1040$ K, $\Delta^2_{\text{ph}} \sim 0.094$ Å$^2$. These values are of the same order used in our calculations, clarifying that the resistivity behavior isn't the result of using physically unrealistic values of $\Delta^2_{\text{ph}}$.

The range of the temperature axis in Fig. 6.4(c) is reasonable with the linear region starting close to the Curie temperature $\sim 290$ K. When comparing the absolute resistivities between theory and experiment, the calculated resistivities are $\sim 1.2$ times larger than the experimental values, which is expected since the apparent SDR is also larger than the experimental value by a similar factor.

The deviations calculated using Eq. 6.2 in Fig. 6.4(d) are reasonable for Fe when the ambiguity of extracting an experimental SDR and the sources of overestimation discussed above are taken into account. The saturated value of $\rho_{\mathrm{DMR}}/\rho(0)$ is of the same order as that observed in dilute alloys, suggesting that there is some variation in the scattering rates at the Fermi energy. While this may be a plausible explanation for Fe, the strong enhancement in Gd cannot be explained in the same way. The dilute magnetic alloys have similar $\rho_{\mathrm{DMR}}/\rho(0)$ ratios, but in that case it is clear that this is due to two-channel conduction.

The DOS of paramagnetic Gd is shown in Fig. 6.5 for different mean-square phonon displacements. Fig. 6.5(a) shows that the DOS for paramagnetic Gd behaves like a Stoner magnet with unequal weights in the two spin channels and the inclusion of phonon disorder does not change this. Phonon disorder broadens the bands, and by Fig. 6.5(e) the peak features near the Fermi energy are smoothed out, which correlates with the onset of linear behavior in Fig. 6.4(c).

The evolution of the DOS is reminiscent of the effects of Anderson disorder, suggesting that the deviations may not be unique to the combination of spin and phonon disorder. In Fig. 6.6 the resistivity is calculated as a function of the square of Anderson disorder amplitudes and the same qualitative resistivity behavior is observed. The same resistivity trend is also observed for *non-magnetic* input potentials, which is not completely unexpected since the non-magnetic DOS of Gd is very similar to the DOS of the paramagnetic phase. This indicates that the resistivity enhancement is entirely an electronic structure effect and that the linear behavior at large amplitudes (or large phonon displacements) is a saturation effect due to the large degree of disorder present in the system.

The spectral function plots in Fig. 6.7 demonstrate the before and after effect of including Anderson disorder. The first row indicates that spin disorder has little

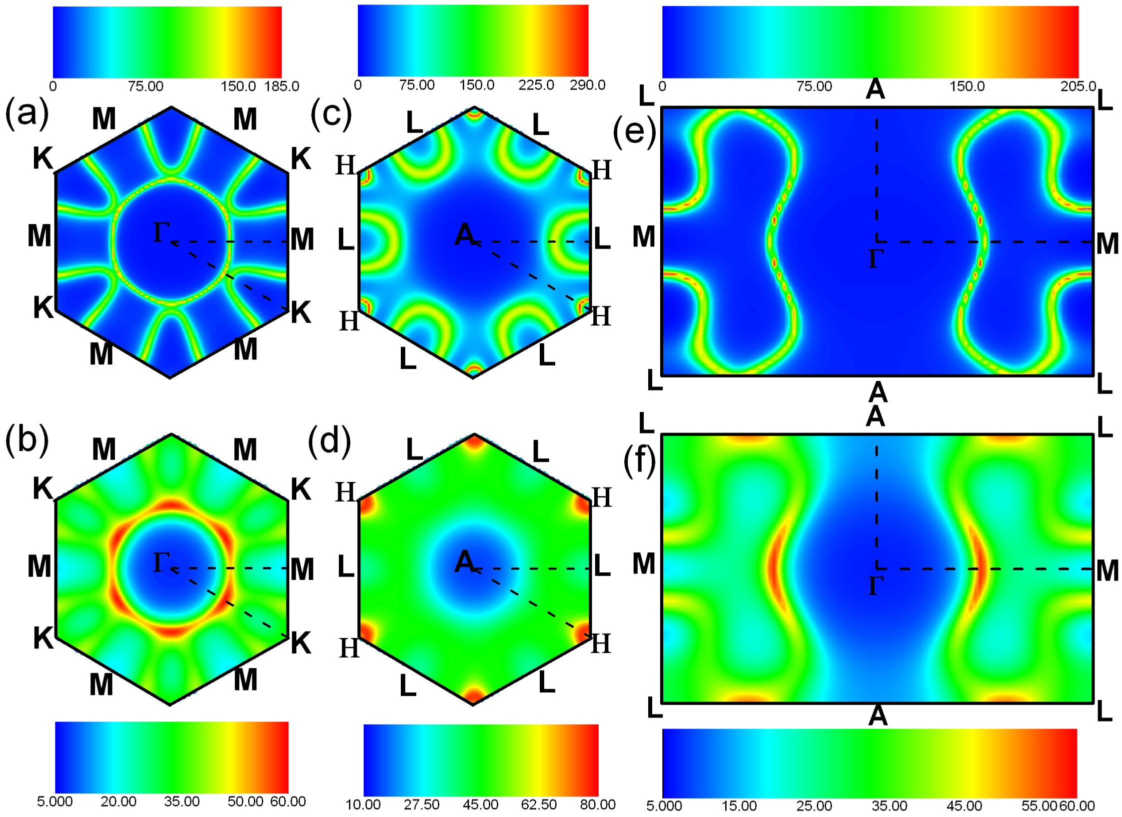

Figure 6.7: The spectral function of Gd calculated at the Fermi energy in CPA along the indicated planes in reciprocal space. The first row of calculations (a), (c), and (e) are DLM only and the second row of calculations (b), (d), and (f) are DLM with an Anderson disorder amplitude of 0.95 eV.

effect on the Fermi surface which is nearly identical to the non-magnetic Fermi surface [219]. As discussed in Ref. [219], the cylindrical sheet centered around the $\Gamma - \mathrm{A}$ line is a hole Fermi surface and the pockets outside it are electron Fermi surfaces. There are several points where the electron and hole surfaces approach each other, such as along the $\Gamma - \mathrm{K}$ line. The surfaces cross near the $\Gamma - \mathrm{H}$ line and are degenerate on the AHL plane. When Anderson disorder is introduced, the locations where the surfaces are either degenerate or close to touching strongly interact as indicated by the large spectral weight appearing in these regions. This effect is most dramatic around the Γ-centered cylinder in Fig. 6.7(b) and over the entire AHL plane in Fig. 6.7(d). Overall, the rapid increase in the Gd resistivity can be viewed as resulting from the strong interaction between the hole and electron Fermi surfaces activated by Anderson (or phonon) disorder. When $\Delta_{\text{And}}$ is increased to values consistent with the linear region in Fig. 6.6, the broadening overwhelms the interaction effects and an incoherent spectral weight spans the Brillouin zone, consistent with the observation that the linear behavior is a saturation effect due to strong disorder. These observations also provide an explanation for why the enhancement in Fe is modest compared to Gd; the Fermi surface of Fe does not have separate sheets that can interact and the paramagnetic state alone corresponds to strong disorder, such that with DLM only the spectral function already has incoherent weight throughout the Brillouin zone.

The band broadening (normalized by the initial broadening in the DLM state) in the Gd spectral function, which is proportional to the inverse scattering rate, is modest when the broadening rates of different bands are compared. The most significant differences when comparing broadening rates between two band crossings with similar Fermi velocities are the electron Fermi surface crossings along the $\mathrm{M}-\mathrm{K}$ line and the $\Gamma - \mathrm{K}$ line, which differ by 22%. The typical variation of broadening rates when comparing most band crossings is between $5 - 10\%$. This will contribute to the deviations observed in the resistivity calculations, but cannot account for the full enhancement of Gd.

Finally, the spectral function of Gd appears to resolve a discrepancy between theory and experiment regarding the shape of the paramagnetic Fermi surface. The calculated non-magnetic Gd hole Fermi surface has a cylindrical trunk and "arms" at the top and bottom of the Brillouin zone [58]. Since the non-magnetic electronic structure is very similar to DLM calculation, the paramagnetic and non-magnetic Fermi surfaces should agree, which is the case for our calculations. However, the angle-resolved photoemission spectroscopy (ARPES) investigation of Gd by Döbrich *et. al.* [194] at 300 K measured a paramagnetic hole Fermi surface without arms in the AHL plane. Comparing the spectral function in Figs. 6.7(e) & 6.7(f) shows that Anderson disorder will lead to incoherent spectral weight close to the AHL plane, save for a cylindrical region near the A point. Therefore phonon disorder, as suggested by the spectral function, may obscure the arm features and as a result the ARPES measurements would only detect the outline of the dark blue cylindrical shape in Fig. 6.7(f). The ARPES data for the ΓMLA plane of paramagnetic Gd also has a dark gray region outside of the cylindrical trunk, the shape of which is consistent with the spectral function in Fig. 6.7(f).

## 6.5 Conclusions

We studied the dependence of the resistivity of randomly spin-disordered $\alpha$-Fe, $\gamma$-Fe, and Gd as a function of the mean-square displacement $\Delta^2_{\mathrm{ph}}$ of the atomic positions. We found that including phonon disorder with spin disorder leads to a non-linear dependence of the resistivity for smaller displacements, transitioning into a linear dependence at larger displacements which, when fitted, leads to an apparent SDR larger than the bare SDR. The enhancement is moderate for both phases of Fe and substantial for Gd, which suggests that previous underestimations of the SDR of Gd compared with experiment are due to the neglect of phonons. The same qualitative behavior in the resistivity of Gd is also observed when Anderson disorder is substituted in for phonon disorder, both for spin-disordered magnetic potentials and non-magnetic potentials, indicating that the deviations are electronic in origin and the linear behavior is a saturation effect brought on by strong disorder. The rapid increase of the resistivity in Gd can be traced to an interaction between the hole and electron Fermi surfaces of Gd activated by disorder wherever the surfaces intersect or nearly touch. This suggests that large discrepancies between the apparent and bare SDRs may be expected in magnetic metals where the Fermi surface is still reasonably well-defined in the spin-disordered (DLM) state and has multiple Fermi sheets that touch, or nearly touch, in the Brillouin zone.

# Bibliography

[1] S. Khmelevskyi, I. Turek, and P. Mohn, Phys. Rev. B **70**, 132401 (2004).

[2] P. R. Pallister, J Iron Steel Inst **161**, 87 (1949).

[3] W. Fulkerson, J. P. Moore, and D. L. McElroy, J. Appl. Phys. **37**, 2639 (1966).

[4] A. Cezairliyan and J. L. McClure, J. Res. NBS **78A**, 1 (1974).

[5] Y. Liu, A. A. Starikov, Z. Yuan, and P. J. Kelly, Phys. Rev. B **84**, 014412 (2011).

[6] R. V. Colvin, S. Legvold, and F. H. Spedding, Phys. Rev. **120**, 741–745 (1960).

[7] P. M. Hall, S. Legvold, and F. H. Spedding, Phys. Rev. **117**, 971–973 (1960).

[8] R. W. Green, S. Legvold, and F. H. Spedding, Phys. Rev. **122**, 827–830 (1961).

[9] D. L. Strandburg, S. Legvold, and F. H. Spedding, Phys. Rev. **127**, 2046–2051 (1962).

[10] D. E. Hegland, S. Legvold, and F. H. Spedding, Phys. Rev. **158**, 158–162 (1963).

[11] H. E. Nigh, S. Legvold, and F. H. Spedding, Phys. Rev. **132**, 1092 (1963).

[12] L. R. Edwards and S. Legvold, Phys. Rev. **176**, 753–760 (1968).

[13] S. V. Vonsovskii, *Magnetism* (Haldsted Press, New York, 1974).

[14] V. V. Zhirnov, Proc. IEEE **91**, 1934 (2003).

[15] M. Kanellos, *Intel scientists find wall for Moore's Law*, CNET News, http://news.cnet.com/Intel-scientists-find-wall-for-Moores-Law/2100-1008_3-5112061.html (2003).

[16] S. Datta and B. Das, Appl. Phys. Lett. **56**, 665 (1990).

[17] H. A. Lorentz, *The theory of electrons and its applications to the phenomena of light and radiant heat*, 2nd ed. (B.G. Teubner, Leipzig, 1916).

[18] J. H. V. Vleck, *The Theory of Electric and Magnetic Susceptibilities* (The Clarendon Press, Oxford, England, 1932).

[19] J. D. Jackson, *Classical Electrodynamics*, 3rd ed. (John Wiley & Sons, Inc., 1999).

[20] P. Langevin, J. de Phys. Th. et App. **4**, 678 (1905).

[21] P. Curie, Ann. de Chim. et Phys. **5**, 289 (1895).

[22] P. Weiss, J. de Phys. Th. et App. **6**, 661 (1907).

[23] J. H. van Leeuwen, J. de Phys. Radium **2**, 361 (1921).

[24] N. Bohr, *Studier over Metallernes Elektrontheori*, Ph.D. thesis, University of Copenhagen (1911).

[25] A. H. Compton, J. Frankl. Inst. **192**, 145 (1921).

[26] D. Hanneke, S. Fogwell, and G. Gabrielse, Phys. Rev. Lett. **100**, 120801 (2008).

[27] R. Skomski, *Simple Models of Magnetism* (Oxford University Press, New York, 2008).

[28] L. D. Landau and E. M. Lifshitz, *Quantum Mechanics (Non-relativistic Theory)*, 3rd ed. (Pergamon Press, Oxford, 1977).

[29] R. Kubo and T. Nagamiya, eds., *Solid state physics* (McGraw-Hill, New York, 1969).

[30] N. W. Ashcroft and N. D. Mermin, *Solid State Physics* (Holt, Rinehart, & Winston, New York, 1976).

[31] H. Kramers, Physica **1**, 182 (1934).

[32] P. W. Anderson, Phys. Rev. **79**, 350 (1950).

[33] J. H. V. Vleck, J. Phys. Radium **12**, 262 (1951).

[34] M. A. Ruderman and C. Kittel, Phys. Rev. **96**, 99 (1954).

[35] K. Yosida, Phys. Rev. **106**, 893 (1957).

[36] T. Kasuya, Prog. Theor. Phys. **16**, 45 (1956).

[37] J. K. Kübler, *Theory of itinerant electron magnetism* (Oxford University Press, New York, 2000).

[38] M. Johnson and R. H. Silsbee, Phys. Rev. B **35**, 4959 (1987).

[39] M. Johnson and R. H. Silsbee, Phys. Rev. B **37**, 5312 (1988).

[40] P. C. van Son, H. van Kempen, and P. Wyder, Phys. Rev. Lett. **58**, 2271 (1987).

[41] T. Valet and A. Fert, Phys. Rev. B **48**, 7099 (1993).

[42] S. Hershfield and H. L. Zhao, Phys. Rev. B **56**, 3296 (1997).

[43] E. I. Rashba, Phys. Rev. B **62**, R16267 (2000).

[44] E. I. Rashba, Eur. Phys. J. B **29**, 513 (2002).

[45] M. Ziese and M. J. Thornton, eds., *Spin Electronics* (Springer, 2001).

[46] A. G. Aronov, JETP Lett. **24**, 32 (1976).

[47] A. G. Aronov and G. E. Pikus, Sov. Phys. Semicond. **10**, 698 (1976).

[48] M. N. Baibich, J. M. Broto, A. Fert, F. N. V. Dau, F. Petroff, P. Etienne, G. Creuzet, A. Friederich, and J. Chazelas, Phys. Rev. Lett. **61**, 2472 (1988).

[49] G. Binasch, P. Grünberg, F. Saurenbach, and W. Zinn, Phys. Rev. B **39**, 4828 (1989).

[50] N. F. Mott, Proc. R. Soc. A **153**, 699 (1936).

[51] G. Schmidt, D. Ferrand, L. W. Molenkamp, A. T. Filip, and B. J. van Wees, Phys. Rev. B **62**, R4790 (2000).

[52] P. R. Hammer, B. R. Bennet, M. J. Yang, and M. Johnson, Phys. Rev. Lett. **83**, 203 (1999).

[53] B. T. Jonker, S. Erwin, A. Petrou, and A. G. Petukhov, MRS Bulletin **28**, 740 (2003).

[54] P. R. Hammer and M. Johnson, Appl. Phys. Lett. **79**, 2591 (2001).

[55] H. J. Zhu, M. Ramsteiner, H. Kostial, M. Wassermeier, H.-P. Schönherr, and K. H. Ploog, Phys. Rev. Lett. **87**, 016601 (2001).

[56] R. Fiederling, M. Keim, G. Reuscher, W. Ossau, G. Schmidt, A. Waag, and L. W. Molenkamp, Nature **402**, 790 (1999).

[57] K. N. R. Taylor and M. I. Darby, *Physics of Rare Earth Solids* (Chapman and Hall LTD, London, 1972).

[58] B. Coqblin, *The electronic structure of rare-earth metals and alloys: the magnetic heavy rare-earths* (Academic Press, New York, 1977).

[59] B. R. Coles, Adv. Phys. **7**, 40 (1958).

[60] N. F. Mott, Adv. Phys. **13**, 325 (1964).

[61] T. Kasuya, Prog. Theor. Phys. **16**, 58–63 (1956).

[62] P. G. de Gennes and J. Friedel, J. Phys. Chem. Solids **4**, 71 (1958).

[63] P. Drude, Annalen der Physik **306**, 566 (1900).

[64] M. D. Wilding and E. W. Lee, Proc. Phys. Soc. **85**, 955–961 (1965).

[65] P. Jacobsson and B. Sundqvist, Phys. Rev. B **40**, 9541–9551 (1989).

[66] K. Maezawa, K. Mori, K. Sato, Y. Saito, and S. Wakabayashi, J. Phys. Soc. Jpn. **43**, 1815 (1977).

[67] M. Ellerby, K. A. McEwen, and J. Jensen, Phys. Rev. B **57**, 8416–8423 (1998).

[68] M. Ellerby, K. A. McEwen, E. Bauer, R. Hauser, and J. Jensen, Phys. Rev. B **61**, 6790–6797 (2000).

[69] R. Brout and H. Suhl, Phys. Rev. Lett. **2**, 387–389 (1959).

[70] S. Legvold, Phys. Rev. B **3**, 1640–1642 (1971).

[71] L. H. Thomas, Proc. Cambridge Phil. Roy. Soc. **23**, 542 (1927).

[72] E. Fermi, Rend. Accad. Naz. Lincei **6**, 602 (1927).

[73] P. A. M. Dirac, Proc. Cambridge Phil. Roy. Soc. **26**, 376 (1930).

[74] P. Hohenberg and W. Kohn, Phys. Rev. **136**, B864 (1964).

[75] W. Kohn and L. J. Sham, Phys. Rev. **140**, A1133 (1965).

[76] R. M. Martin, *Electronic Structure: Basic Theory and Pratical Methods* (Cambridge University Press, Cambridge, 2004).

[77] M. Born and J. R. Oppenheimer, Ann. Physik **84**, 457 (1927).

[78] W. Kohn, *Highlights in Condensed Matter Theory*, edited by F. Bassani, F. Fumi, and M. P. Tosi (North-Holland Physics Publishing, Amsterdam, 1985).

[79] M. Levy, Proc. Nat. Acad. Sci. USA **76**, 6062 (1979).

[80] M. Levy, Phys. Rev. A **26**, 1200 (1982).

[81] M. Levy and J. P. Perdew, *Density Functional Methods in Physics*, edited by R. M. Dreizler and J. da Providencia (Plenum, New York, 1985).

[82] E. Lieb, *Physics as Natural Philosophy*, edited by A. Shimony and H. Feshbach (MIT Press, Cambridge, 1982).

[83] E. Lieb, Int. J. Quant. Chem. **24**, 243 (1983).

[84] E. Lieb, *Density Functional Methods in Physics*, edited by R. M. Dreizler and J. da Providencia (Plenum, New York, 1985).

[85] J. W. Strutt, *Theory of Sound*, Vol. I, Sec. 88 (Reprint: Dover Publications, New York, 1945).

[86] W. Ritz, Reine Angew. Math. **135**, 1 (1908).

[87] C. Fiolhais, F. Nogueira, and M. Marques, *A Primer in Density Functional Theory* (Springer-Verlag, New York, 2003).

[88] J. P. Perdew and A. Zunger, Phys. Rev. B **23**, 5048 (1981).

[89] A. Svane and O. Gunnarsson, Phys. Rev. B **37**, 9919 (1988).

[90] M. E. Casida, *Recent Developments and Application of Density Functional Theory*, edited by J. M. Seminario (Elsevier, 1996) p. 391.

[91] T. Grabo, T. Kreibich, S. Kurth, and E. K. U. Gross, *Strong Coulomb Correlations in Electronic Structure: Beyond the Local Density Approximation*, edited by V. I. Anisimov (Gordon & Breach, Tokyo, 1998).

[92] L. J. Sham and M. Schlüter, Phys. Rev. B **32**, 3883 (1985).

[93] A. Seidl, A. Görling, P. Vogl, J. A. Majewski, and M. Levy, Phys. Rev. B **53**, 3764 (1996).

[94] J. Heyd, G. E. Scuseria, and M. Ernzerhof, J. Chem. Phys. **118**, 8207 (2003).

[95] J. Heyd and G. E. Scuseria, J. Chem. Phys. **121**, 1187 (2004).

[96] V. I. Anisimov, J. Zaanen, and O. K. Andersen, Phys. Rev. B **44**, 943 (1991).

[97] H. J. Kulik, M. Cococcioni, D. A. Scherlis, and N. Marzari, Phys. Rev. Lett. **97**, 103001 (2006).

[98] A. Georges, G. Kotliar, W. Krauth, and M. J. Rozenberg, Rev. Mod. Phys. **68**, 13 (1996).

[99] L. O. Wagner, E. M. Stoudenmire, K. Burke, and S. R. White, Phys. Chem. Chem. Phys. **14**, 8581 (2012).

[100] U. von Barth and L. Hedin, J. Phys. C **5**, 1629 (1972).

[101] L. Hedin and S. Lundquist, *Solid State Physics*, edited by H. Ehenreich, F. Seitz, and D. Turnbull (Academic Press, 1969).

[102] V. L. Moruzzi, J. F. Janek, and A. R. Williams, *Calculated Electronic Properties of Metals* (Pergamon Press, New York, 1978).

[103] D. M. Ceperley and B. J. Alder, Phys. Rev. Lett. **45**, 566 (1980).

[104] S. Vosko, L. Wilkes, and M. Nusair, Can. J. Phys. **58**, 1200 (1983).

[105] I. Turek, V. Drchal, J. Kudrnovský, M. Sob, and P. Weinberger, *Electronic Structure of Disordered Alloys, Surfaces and Interfaces* (Kluwer Academic Publishers, Boston, 1997).

[106] H. L. Skriver, *The LMTO method : muffin-tin orbitals and electronic structure* (Springer-Verlag, New York, 1984).

[107] T. Moriya, *Spin Fluctuations in Itinerant Electron Magnetism* (Springer, Berlin, 1985).

[108] K. K. Murata and S. Doniach, Phys. Rev. Lett. **29**, 285 (1972).

[109] G. G. Lonzarich and L. Taillefer, J. Phys. C **18**, 4339 (1985).

[110] T. Moriya and Y. Takahashi, J. Phys. Soc. Jpn. **45**, 397 (1978).

[111] J. Hubbard, *Electron correlation and magnetism in narrow-band systems*, edited by T. Moriya (Springer, Berlin, 1981) p. 29.

[112] H. Hasegawa, *Electron correlation and magnetism in narrow-band systems*, edited by T. Moriya (Springer, 1981) p. 38.

[113] L. D. Landau and E. M. Lifshitz, *Statistical Physics* (Pergamon Press, 1980) p. 478, sec. 147.

[114] P. Mohn and P. Wohlfarth, J. Phys. F **17**, 2421 (1986).

[115] R. F. Hassing and D. M. Esterling, Phys. Rev. B **7**, 432 (1973).

[116] B. L. Gyorffy, A. J. Pindor, J. Staunton, G. M. Stocks, and H. Winter, J. Phys. F: Met. Phys. **15**, 1337 (1985).

[117] P. H. Dederichs, S. Blügel, R. Zeller, and H. Akai, Phys. Rev. Lett. **53**, 2512 (1984).

[118] T. Oguchi, K. Terakura, and N. Hamada, J. Phys. F **13**, 145 (1983).

[119] J. B. Staunton and B. L. Gyorffy, Phys. Rev. Lett. **69**, 371 (1992).

[120] M. Uhl and J. Kübler, Phys. Rev. Lett. **77**, 334 (1996).

[121] N. M. Rosengaard and B. Johansson, Phys. Rev. B **55**, 14975 (1997).

[122] M. Ležaić, P. Mavropoulos, J. Enkovaara, G. Bihlmayer, and S. Blügel, Phys. Rev. Lett. **97**, 026404 (2006).

[123] A. V. Ruban, S. Khmelevskyi, P. Mohn, and B. Johansson, Phys. Rev. B **75**, 054402 (2007).

[124] V. P. Antropov, Phys. Rev. B **72**, 140406(R) (2005).

[125] J. Kübler, J. Phys.: Condens. Matter **18**, 9795 (2006).

[126] D. P. Landau and K. Binder, *A guide to Monte Carlo simulations in Statistical Physics* (Cambridge University Press, Cambridge, 2000).

[127] L. Onsager, J. Am. Chem. Soc. **58**, 1486 (1936).

[128] R. Brout and H. Thomas, Physics (Long Island City, N.Y.) **3**, 317 (1967).

[129] D. E. Logan, Y. H. Szczech, and M. A. Tusch, Europhys. Lett. **30**, 307 (1995).

[130] M. Cyrot, *Electron correlation and magnetism in narrow-band systems*, edited by T. Moriya (Springer, Berlin, 1981).

[131] M. Cyrot, J. Magn. Magn. Mater. **45**, 9 (1984).

[132] M. Cyrot and H. Kaga, Phys. Rev. Lett. **77**, 5134 (1996).

[133] H. Kaga and M. Cyrot, Phys. Rev. B **58**, 12267 (1998).

[134] M. Wortis, *Phase Transitions and Critical Phenomena*, edited by C. Domb and M. S. Green, Vol. 3 (Academic Press, London, 1974) p. 114.

[135] V. G. Vaks, A. I. Larkin, and S. A. Pikin, Sov. Phys. JETP **24**, 240 (1967).

[136] K. Chen, A. M. Ferrenberg, and D. P. Landau, Phys. Rev. B **48**, 3249 (1993).

[137] G. Horwitz and H. B. Callen, Phys. Rev. **124**, 1757 (1961).

[138] I. Žutić, J. Fabian, and S. D. Sarma, Rev. Mod. Phys. **76**, 323 (2004).

[139] M. Johnson, *Handbook of Spin Transport and Magnetism*, edited by E. Y. Tsymbal and I. Žutić (CRC Press, Boca Raton, FL, 2012) p. p. 115.

[140] R. Jansen, Nature Mater. **11**, 400 (2012).

[141] L. W. Cheuk, A. T. Sommer, Z. Hadzibabic, T. Yefsah, W. S. Bakr, and M. W. Zwierlein, Phys. Rev. Lett. **109**, 095302 (2012).

[142] I. ˇ Zutić, J. Fabian, and S. C. Erwin, J. Phys.: Condens. Matter **19**, 165219 (2007).

[143] I. ˇ Zutić, J. Fabian, and S. D. Sarma, Phys. Rev. Lett. **88**, 066603 (2002).

[144] A. T. Hanbicki, B. T. Jonker, G. Itskos, G. Kioseoglou, and A. Petrou, Appl. Phys. Lett. **80**, 1240 (2002).

[145] S. A. Crooker, M. Furis, X. Lou, C. Adelmann, D. L. Smith, C. J. Palmstrom, and P. A. Crowell, Science **309**, 2191 (2005).

[146] B. T. Jonker, G. Kioseoglou, A. T. Hanbicki, C. H. Li, and P. E. Thompson, Nature Phys. **3**, 542 (2007).

[147] S. P. Dash, S. Sharma, R. S. Patel, M. P. de Jong, and R. Jansen, Nature **462**, 491 (2009).

[148] R. A. de Groot, F. M. Mueller, P. G. van Engen, and K. H. J. Buschow, Phys. Rev. Lett. **50**, 2024 (1983).

[149] M. I. Katsnelson, V. Y. Irkhin, L. Chioncel, A. I. Lichtenstein, and R. A. de Groot, Rev. Mod. Phys. **80**, 315 (2008).

[150] P. A. Dowben and R. Skomski, J. Appl. Phys. **95**, 7453 (2004).

[151] Y. Sakuraba, M. Hattori, M. Oogane, Y. Ando, H. Kato, A. Sakuma, T. Miyazaki, and H. Kubota, Appl. Phys. Lett. **88**, 192508 (2006).

[152] T. Marukame, T. Ishikawa, K.-I. Matsuda, T. Uemura, and M. Yamamoto, Appl. Phys. Lett. **88**, 262503 (2006).

[153] T. Ishikawa, T. Marukame, H. Kijima, K.-I. Matsuda, T. Uemura, M. Arita, and M. Yamamoto, Appl. Phys. Lett. **89**, 192505 (2006).

[154] H. Sukegawa, W. Wang, R. Shan, T. Nakatani, K. Inomata, and K. Hono, Phys. Rev. B **79**, 184418 (2009).

[155] T. M. Nakatani, T. Furubayashi, S. Kasai, H. Sukegawa, Y. K. Takahashi, S. Mitani, and K. Hono, Appl. Phys. Lett. **96**, 212501 (2010).

[156] G. Bridoux, M. V. Costache, J. V. de Vondel, I. Neumann, and S. O. Valenzuela, Appl. Phys. Lett. **99**, 102107 (2011).

[157] T. Kimura, N. Hashimoto, S. Yamada, M. Miyao, and K. Hamaya, NPG Asia Mater. **4**, e9 (2012).

[158] K. Hamaya, N. Hashimoto, S. Oki, S. Yamada, M. Miyao, and T. Kimura, Phys. Rev. B **85**, 100404(R) (2012).

[159] M. Ramsteiner, O. Brandt, T. Flissikowski, H. T. Grahn, M. Hashimoto, J. Herfort, and H. Kostial, Phys. Rev. B **78**, 121303(R) (2008).

[160] S. Takahashi and S. Maekawa, Phys. Rev. B **67**, 052409 (2003).

[161] R. Skomski and P. A. Dowben, Europhys. Lett. **58**, 544 (2002).

[162] X. Waintal, E. B. Myers, P. W. Brouwer, and D. C. Ralph, Phys. Rev. B **62**, 12317 (2000).

[163] P. A. Mello, P. Pereyra, and N. Kumar, Ann. Phys. (N.Y.) **181**, 290 (1988).

[164] C. W. J. Beenakker, Rev. Mod. Phys. **69**, 731 (1997).

[165] P. W. Brouwer and C. W. J. Beenakker, J. Math. Phys. **37**, 4904 (1996).

[166] A. Brataas, Y. V. Nazarov, and G. E. W. Bauer, Phys. Rev. Lett. **84**, 2481 (2000).

[167] J. Bass and W. P. Pratt, J. Phys.: Condens. Matter **19**, 183201 (2007).

[168] H. Y. T. Nguyen, R. Loloee, W. P. Pratt, and J. Bass, Phys. Rev. B **86**, 064413 (2012).

[169] S. Garzon, I. Žutić, and R. A. Webb, Phys. Rev. Lett. **94**, 176601 (2005).

[170] L. Weber and E. Gmelin, Appl. Phys. A **53**, 136 (1991).

[171] P. Mavropoulos, M. Ležaić, and S. Blügel, Phys. Rev. B **72**, 174428 (2005).

[172] S. Chadov, T. Graf, K. Chadova, X. Dai, F. Casper, G. H. Fecher, and C. Felser, Phys. Rev. Lett. **107**, 047202 (2011).

[173] T. N. Todorov, Phys. Rev. B **54**, 5801 (1996).

[174] T. Kasuya, Prog. Theor. Phys. **22**, 227–246 (1959).

[175] A. J. Dekker, J. Appl. Phys. **36**, 906–912 (1965).

[176] H. Miwa, Prog. Theor. Phys. **28**, 208–210 (1962).

[177] A. R. Mackintosh, Phys. Rev. Lett. **9**, 90–93 (1962).

[178] R. J. Elliott and F. A. Wedgwood, Proc. Phys. Soc. **81**, 846–855 (1963).

[179] A. L. Wysocki, R. F. Sabirianov, M. van Schilfgaarde, and K. D. Belashchenko, Phys. Rev. B **80**, 224423 (2009).

[180] S. Legvold, F. H. Spedding, F. Barson, and J. F. Elliott, Rev. Mod. Phys. **25**, 129–130 (1953).

[181] P. Kurz, G. Bihlmayer, and S. Blügel, J. Phys.: Condens. Matter **14**, 6353 (2002).

[182] Y. Baer and W.-D. Schneider, *Handbook on the physics and chemistry of rare earths*, edited by K. A. Gschneidner Jr., L. Eyring, and S. Hüfner, Vol. 10 (North-Holland Physics Publishing, Amsterdam, 1987) pp. 1–73.

[183] O. K. Andersen, Phys. Rev. B **12**, 3060 (1975).

[184] I. Turek, J. Kudrnovský, G. Bihlmayer, and S. Blügel, J. Phys.: Condens. Matter **15**, 2771–2782 (2003).

[185] J. Kudrnovský, V. Drchal, C. Blaas, P. Weinberger, I. Turek, and P. Bruno, Phys. Rev. B **62**, 15084 (2000).

[186] S. Datta, *Electronic Transport in Mesoscopic Systems* (Cambridge University Press, Cambridge, 1995).

[187] A. I. Liechtenstein, V. I. Anisimov, and J. Zaanen, Phys. Rev. B **52**, R5467–R5470 (1995).

[188] J. Kudrnovský, V. Drchal, I. Turek, S. Khmelevskyi, J. K. Glasbrenner, and K. D. Belashchenko, Phys. Rev. B **86**, 144423 (2012).

[189] A. Burusz, L. Szunyogh, and P. Weinberger, Phil. Mag. **88**, 2615 (2008).

[190] I. Turek, J. Kudrnovský, V. Drchal, L. Szunyogh, and P. Weinberger, Phys. Rev. B **65**, 125101 (2002).

[191] K. Carva, I. Turek, J. Kudrnovský, and O. Bengone, Phys. Rev. B **73**, 144421 (2006).

[192] J. K. Alstad, R. V. Colvin, and S. Legvold, Phys. Rev. **123**, 418–419 (1961).

[193] S. Blügel and G. Bihlmayer, *Computational Nanoscience: Do It Yourself!*, edited by J. Grotendorst, S. Blügel, and D. Marx, NIC Series, Vol. 31 (John von Neumann Instiitite for Computing, Jülich, 2006) p. 85; www.flapw.de.

[194] K. M. Döbrich, A. Bostwick, E. Rotenberg, and G. Kaindl, Phys. Rev. B **81**, 012401 (2010).

[195] R. J. Weiss and A. S. Marotta, J. Phys. Chem. Solids **9**, 302 (1959).

[196] J. M. Ziman, *Electrons and Phonons* (Oxford University Press, New York, 1960).

[197] R. W. Powell, Phil. Mag. **44**, 772 (1953).

[198] J. Bass, in *SpringerMaterials - The Landolt-Börnstein Database (http://www.springermaterials.com)*, Vol. 15a, edited by K.-H. Hellwege and J. L. Olsen (Springer, Berlin, 1982) Chap. 1.2.2, pp. 27–41.

[199] J. K. Glasbrenner, K. D. Belashchenko, J. Kudrnovský, V. Drchal, S. Khmelevskyi, and I. Turek, Phys. Rev. B **85**, 214405 (2012).

[200] D. Alfé, M. Pozzo, and M. Desjarlais, Phys. Rev. B **85**, 024102 (2012).

[201] J. Bass, Adv. Phys. **21**, 431 (1972).

[202] D. K. C. MacDonald, *Handbuch der Physik*, edited by S. Flugge, Vol. Vol. XIV (Springer, Berlin, 1956) p. 137.

[203] J. M. Ziman, Phys. Rev. **121**, 1320 (1961).

[204] P. L. Taylor, Proc. R. Soc. Lond. A **275**, 209 (1963).

[205] K. Fischer, Phys. kondens. Materie **6**, 171 (1967).

[206] E. H. Sondheimer and A. H. Wilson, Proc. R. Soc. Lond. A **190**, 435 (1947).

[207] J. S. Dugdale and Z. S. Basinski, Phys. Rev. **157**, 552 (1967).

[208] S. Arajs, F. C. Schwerer, and R. M. Fisher, Phys. Stat. Sol. (B) **33**, 731 (1969).

[209] I. A. Campbell, A. Fert, and A. R. Pomeroy, Phil. Mag. **15**, 977 (1967).

[210] A. Fert and I. A. Campbell, Phys. Rev. Lett. **21**, 1190 (1968).

[211] A. Fert and I. A. Campbell, J. Phys. F: Metal Phys. **6**, 849 (1976).

[212] W. B. Pearson, *A Handbook of Lattice Spacings and Structures of Metals and Alloys* (Pergamon Press, New York, 1958).

[213] J. Prakash, L. P. Pathak, and M. P. Hemkar, Aust. J. Phys. **28**, 63 (1975).

[214] C. W. Haworth, Phil. Mag. **5**, 1229 (1960).

[215] N. Singh and P. K. Sharma, Phys. Rev. B **3**, 1141 (1966).

[216] R. Cavalheiro and M. M. Shukla, Phys. Stat. Sol. (B) **98**, 685 (1980).

[217] H. L. Kharoo, O. P. Gupta, and M. P. He, J. Phys. Soc. Jpn. **43**, 2030 (1977).

[218] C. R. Pinnegar, *Phonon dispersion curves and atomic mean square displacement for several fcc and bcc materials*, Master's thesis, Brock University, St. Catharines, Ontario (1995).

[219] S. C. Keeton and T. L. Loucks, Phys. Rev. **168**, 672 (1968).

# Publications

K. D. Belashchenko, **J. K. Glasbrenner**, and A. L. Wysocki, ”Spin injection from a half-metal at finite temperatures,” Phys. Rev. B **86**, 224402 (2012).

J. Kudrnovský, V. Drchal, I. Turek, S. Khmelevskyi, **J. K. Glasbrenner**, and K. D. Belashchenko, “Spin-disorder resistivity of ferromagnetic metals from first principles: The disordered-local-moment approach,” Phys. Rev. B **86**, 144423 (2012).

**J. K. Glasbrenner**, K. D. Belashchenko, J. Kudrnovský, V. Drchal, S. Khmelevskyi, and I. Turek, “First-principles study of spin-disorder resistivity of heavy rare-earth metals: Gd-Tm series,” Phys. Rev. B **85**, 214405 (2012).

A. L. Wysocki, **J. K. Glasbrenner**, and K. D. Belashchenko, ”Thermodynamics of itinerant magnets in a classical spin-fluctuation model,” Phys. Rev. B **78**, 184419 (2008).

S. N. Walck, **J. K. Glasbrenner**, M. H. Lochman, and S. A. Hilbert, “Topology of the three-qubit space of entanglement types,” Phys. Rev. A **72**, 052324 (2005).